

UNIVERSITÉ DE NANTES
FACULTÉ DES SCIENCES ET DES TECHNIQUES

ÉCOLE DOCTORALE
MOLECULES, MATIERES ET MATERIAUX EN PAYS DE LOIRE

N° attribué par la bibliothèque

--	--	--	--	--	--	--	--	--	--

Année 2011

**INTERACTIONS FAIBLES
DANS LES NANOSYSTEMES CARBONES
WEAK INTERACTIONS IN CARBON NANOSYSTEMS**

THÈSE DE DOCTORAT

Discipline : Physique de Matériaux

Spécialité : Nanomatériaux et Nanotechnologie

Présentée

et soutenue publiquement par

Abu YAYA

Le 4 Nov. 2011, devant le jury ci-dessous

Président M. LEFRANT Serge, Professeur Emerite d'Université de Nantes
Rapporteurs M. HEGGIE Malcolm, Professeur d'Université de Sussex, Royaume Uni.
M. FLAHAUT Emmanuel, Directeur de Recherche CNRS, Toulouse

Examineurs M. EWELS Christopher, Chargé de Recherche, IMN, Nantes
M. VAN LIER Gregory, Post-Doctoral Fellow, d'Université VUB, Belgique
M. DUVAIL Jean-Luc, Professeur d'Université de Nantes

Directeur de thèse : Chris EWELS, Institut des Matériaux Jean Rouxel, Nantes

DECLARATION

I hereby declare that this thesis has not been and will not be, submitted in whole or in part to this or another University for the award of any other degree. I certify that all material in this thesis which is not my own work has been identified.

Signature:

Abu Yaya

4th November, 2011.

Dedication

To my wife, Philo, my son, Malik, and daughter, Hawa, for their patience and their never ending questions ‘what are you doing with this computer’? Playing games! Also to my late Mother, Hawa Jori, who has given me the taste of education.

“If someone feels that they had never made a mistake in their life, then it means they had never tried a new thing in their life”.

-Albert Einstein

Acknowledgements

First and foremost, I would like to thank my thesis supervisor, Dr. Christopher Ewels, for giving me the opportunity to work in his group and for his encouragement, support and patience in all my scientific endeavours. I am extremely grateful for his willingness and encouragement in allowing me to explore and learn new theoretical methods and techniques. Second, I would like to thank my co-supervisor, Prof. Emeritus Serge Lefrant, for his scientific discussions, insight and encouragement. Third, I would like to thank the head of my group, Prof. Jean-Luc Duvail, whose insight and enthusiasm for science I will never forget. Also, I will like to thank all my committee members, Prof. Malcolm Heggie, Dr.Emmanuel Flahaut and Dr.Gregory Van Lier, for taking time off their busy schedules and accepting to be on my external committee, am highly honoured to have such a high calibre of personalities. How can I forget, Dr.Irene Suarez-Martinez, for first putting me on the job of atomistic computer modelling. Thanks to Philipp Wagner and Dr.Victoriya Ivanoskaya, my group members, for the constant knocks on their offices, for doubts I have for clarification. I cannot end without acknowledging the enormous support and help I got from the then secretary of the department, Annie Simons, for helping me with all my paper works right from my first day in Nantes till her departure, your reward is in heaven. Thanks also to Prof.Humbert Bernard for his helpful discussions on Raman spectroscopy. Many thanks should also be given to Prof. Patrick Briddon, for his generosity and help in letting us use the AIMPRO modelling code and his willingness to listen to and answer all my questions; Jean Yves, for his help on the Raman spectroscopy experiments and Prof. Le Bideau Jean, for the French translation.

Also, I will like to thank Mr. Joseph Baah and Pascale El-haj for his support and encouragement; Isaac Musa for his distractions and fun, Dahbia for her moral encouragement, my office colleagues, Nela and Sophie for their patience with me whenever I attended to the telephone in our office and to all the members of the department of Physics of materials and Nanostructure, to which I belong.

Lastly, I will like to thank the Centre National Research Scientific (CNRS) and Pay de la Loire region in the framework of BDI, for funding my PhD.

Résumé de la thèse

Avec le logiciel AIMPRO, qui fournit une modélisation quantique basée sur la théorie de fonctionnelle de densité, on étudie plusieurs exemples importants de la faiblesse des interactions intermoléculaires dans les nanomatériaux de carbone. Au niveau mécanique quantique, nos calculs donnent une compréhension fiable et améliorée du rôle et de la fonction des interactions intermoléculaires faibles, ce qui ne peut pas être prédit par des méthodes conventionnelles comme les potentiels interatomiques classiques.

Premièrement, on étudie l'interaction entre le brome physisorbé sur les nanomatériaux de carbone (graphène, graphite, nanotubes de carbone simple [SWCNT] et double [DWCNT] parois). Pour le graphène, nous trouvons une nouvelle forme de Br_2 , à notre connaissance jamais présentée dans la littérature, où la molécule se trouve perpendiculaire à la feuille de graphène avec un dipôle fort. La bromation ouvre un gap de petite taille (86 meV) dans la structure de bande électronique et dope fortement le graphène. Dans le graphite, Br_2 reste parallèle aux couches de carbone avec un transfert de charge moins fort et sans dipôle moléculaire. À plus haute concentration, la formation de chaînes de polybromure est thermodynamiquement favorisée, mais n'a pas lieu spontanément à cause d'une barrière d'activation appréciable (27,01 kJ / mol). Avec les nanotubes monoparoi, le Br_2 reste perpendiculaire à la surface du tube, comme observé avec le graphène; dans les fagots, le Br_2 s'intercale comme dans le graphite. Les spectres Raman sont enregistrés afin de vérifier ce résultat.

Dans la deuxième partie, on étudie des interactions d'empilement de type π - π entre le benzène d'une part, les chaînes oligomères de PPV d'autre part, avec des nanomatériaux de carbone. Pour le dimère du benzène, nous avons réussi à reproduire les structures stables trouvées par ailleurs via des calculs de plus haut niveau de théorie ; pour le benzène sur le graphène ou sur les SWCNTs, l'empilement est de type AB comme dans le graphite. L'orientation de l'interaction dans le cas PPV / PPV est différente de celle obtenue dans le cas PPV / nanotube ou PPV / graphène. Dans le premier cas des plans moléculaires sont orthogonaux, semblable à un empilement de PPV ou d'autres hydrocarbures aromatiques polycycliques. Dans les autres cas, l'axe de la chaîne de PPV se trouve parallèle au plan du

graphène comme à l'axe des nanotubes, ce qui est attribué à des effets d'empilement π - π . L'analyse des fonctions d'onde près du niveau de Fermi suggère qu'il y a peu de couplage électronique entre PPV et SWCNTs. La différence d'interaction prévue entre PPV et nanotubes semi-conducteurs ou métalliques suggère une nouvelle conception de composites PPV-SWCNT pour les dispositifs électroluminescents organiques.

Les merveilles et la complexité de la vie et son environnement est l'une des plus grandes questions qui ont remis en cause et dérouté l'humanité depuis le début de notre existence. Notre curiosité innée nous a amené à disséquer les mécanismes et les processus qui font de nous ce que nous sommes. Contrôle du comportement à toutes les échelles que nous étudions, du macroscopique au microscopique, le concept d'interaction moléculaire est d'une importance critique. Il est en effet difficile de penser à quelque chose de plus fondamental dans les nanosystèmes que l'interaction moléculaire. Certaines de ces interactions sont très fortes tandis que d'autres sont faibles et même réversibles. Les propriétés des molécules en interactions régissent le type de forces en présence ainsi que la force et la dynamique de cette interaction.

Les caractéristiques des systèmes faiblement liés et de complexes d'hydrogène ont attiré beaucoup d'intérêt pour la recherche en raison de leur importance dans différents domaines, tels que l'emballage de cristal, l'adsorption et la réaction sur les surfaces et interfaces, les effets de solvation hydrophobes ou hydrophiles liés aux processus biologiques et les mécanismes de catalyseur en chimie organique. Afin de comprendre ces réactions, il est crucial d'établir une connaissance fondamentale de la façon dont les atomes et les molécules interagissent avec les surfaces. Par conséquent, la simulation de calcul de ces complexes est perçue comme un outil indispensable en fournissant des informations détaillées concernant les mécanismes de liaison et propriétés interfaciales d'intérêt.

Les nanomatériaux de carbone jouent un rôle unique dans la nature. En fait, la formation de carbone dans les étoiles comme résultat de la fusion de trois α -particules est un processus crucial fournissant l'existence d'éléments chimiques relativement lourds dans l'Univers. La capacité d'atomes de carbone pour former des réseaux complexes est un fait fondamental de

la chimie organique et la base pour l'existence de la vie, du moins, dans ses formes connues. Même le carbone élémentaire montre un comportement inhabituellement complexe en formant un certain nombre de structures très différentes. En dehors du diamant et du graphite qui sont très populaires, les fullerènes récemment découvert, et les nanotubes sont désormais dans le centre d'attention des physiciens et des chimistes. Ainsi, seules trois dimensions (diamant, graphite), unidimensionnelle (nanotubes), et zéro-dimensionnel (fullerènes) allotropes de carbone ont été découvert jusqu'à récemment. La forme à deux dimensions a été manifestement absente, résistant à toute tentative d'observation expérimentale. Cette forme insaisissable de carbone à deux dimensions, a été nommée graphène, et ironiquement, est probablement le meilleur allotrope étudiée. Le graphène est planaire, les arrangements hexagonaux d'atomes de carbone est le point de départ dans tous les calculs sur les nanotubes de carbone graphite et les fullerènes.

L'étude des systèmes faiblement liés avec ces matériaux de carbone à des implications directes pour les problèmes fondamentaux physico-chimiques telles que la spectroscopie moléculaire, les transitions d'état des structures, la sélectivité des liaisons hydrogène, la dynamique des réactions chimiques, la catalyse et les interactions de surface. Mais encore beaucoup de travail reste à faire pour comprendre les similitudes et les différentes interactions entre ces matériaux avec d'autres espèces telles que les gaz absorbés et polymères.

L'adsorption des molécules de Br_2 basse et haute densité a été examiné sur le graphite, le graphène, les nanotubes de carbone à simple et double paroi par la méthode ab initio DFT / LDA, calculs mis en œuvre dans la méthode AIMPRO.

Dans le graphène, nous constatons que les molécules de brome sont préférentiellement orientées perpendiculairement aux plans de carbone. Les molécules forment un dipôle avec un fort transfert de charge associé. La molécule forme un $\text{Br}^+ + \text{Br}^-$, paire qui rend les infra-rouge actif, et aboutit à une l'ouverture d'une petite bande dans le graphène (86 MeV). Ceci est une nouvelle forme de molécule de brome auparavant uniquement considéré comme une

saturation de carbone intermédiaires instables au brome induite obligatoires. Alors que dans la configuration parallèle, aucune distribution de charge dipôle mais symétrique de transfert entre la paire d'atomes. Aussi les énergies de liaison calculée ont montré que les orientations parallèles (0,15 eV) sont moins stables que les orientations perpendiculaires et puisque la différence dans les énergies de liaison entre les structures perpendiculaire et parallèle est négligeable, il est proposé que, à température ambiante, les structures pourraient être intermédiaires en raison de l'agitation.

Dans le graphite, les molécules de brome adoptent une orientation parallèle aux feuillets avec un transfert de charge associés et ceci est en accord avec les données expérimentales lorsqu'elles sont disponibles. Les énergies de liaison pour les deux étapes-1 (Br_2 / AA-graphite) et de stade 2 (Br_2 / AABB) ont été calculés pour être endothermique à la faible couverture en raison de l'énergie de liaison de l' Br_2 /graphite ne pas être en mesure de compenser l'énergie de séparation intercalaire pour la graphite: ce qui a été calculée comme 36,74 meV / atome pour AB et AA-être 12 MeV / atome moins stable. Mais sur bromation, il ya une stabilité préférentiel pour AA-étape-1 que AB stade-1, même si, expérimentalement, aucune étape un composé de brome ont été pensé pour exister.

En outre, pour les nanotubes, quand le brome a été orienté perpendiculairement aux tubes isolés, il adopte un arrangement similaire qu'avec le graphène, et quand ils en ballots intercaler dans les faisceaux comme avec Br_2 graphites intercalés couché parallèle sur les hexagones et par extension similaire, le même phénomène pourrait être vu comme cela se passe pour les nanotubes à double paroi.

A une concentration élevée en Br_2 , la structure de la chaîne polybromure sera thermodynamiquement favorable. Mais la formation de ces chaînes de brome n'est pas spontanée. Il y a une barrière d'activation calculée à -27.01KJ/mol, c'est pourquoi la chaîne n'est pas réalisable. Ainsi, il pourrait impliquer que l'interaction de Coulomb entre les résultats de brome dans la répulsion entre les molécules de brome en raison de transfert de charge à partir des charbons graphène voisins pour les molécules de brome.

Pour ces systèmes, la LDA semble être suffisante et l'ajout d'un terme d'énergie vdW ne devrait pas modifier qualitativement nos résultats, mais peut-être changer nos valeurs pour

les énergies de liaison calculées. En tout cas, un accord entre les valeurs LDA et les données expérimentales a été trouvé.

Interactions impliquant des espèces collage π - π jouer un rôle crucial dans la stabilité et la conformation de l'ADN et les protéines, les cristaux d'empilement des polymères contenant des cycles aromatiques et la reconnaissance des espèces moléculaires (l'auto-assemblage). Celles-ci ont été également connus pour jouer un rôle majeur dans la stabilisation de l'hôte de deviner les complexes et les interactions de certains médicaments à l'ADN.

Cependant, la nature et la variété dans la structure et la composition des composés aromatiques couplée à l'absence d'une compréhension approfondie des interactions π - π , il est difficile d'enquêter sur leurs interactions. Ces difficultés proviennent du traitement de la corrélation électronique, la dispersion, la polarisation et de solvatation, d'une manière qui est appropriée au contexte des applications et dans les limites des ressources informatiques disponibles. Les méthodes expérimentales telles que la RMN ont été utilisées pour étudier la nature de π - π interactions, ce qui donne une information partielle sur les effets énergétiques et substituant. Cependant, l'interprétation de ces résultats expérimentaux est complexe car les effets de solvatation et d'interactions secondaires compliquer la situation.

A la lumière de cela, des études de mécanique quantique deviennent prééminente dans l'étude des interactions impliquant π - π collage. Supérieur méthodes pour fonction d'onde d'une telle théorie quelques-cluster grâce à l'utilisation de triplets perturbative, CCSD (T), avec des ensembles de base grandes, sont connues pour atteindre un bon niveau de précision, mais le coût de calcul est trop exigeant: les échelles de temps pour sur $O(N^7)$, où N est le nombre d'atomes dans le système. Des méthodes moins coûteuses telles que la perturbation Møller-Plesset (MP2) peut aussi devenir cher quand une fonction de base est pris en grande considération. En outre, ils conduisent à une surestimation des effets de corrélation d'électrons qui sont inhérents à π - π purs interactions. Voici donc également laisser des problèmes pour la compréhension théorique des grands systèmes contenant π - π interactions d'empilement, qui ne sont pas encore pleinement compris. Néanmoins, la littérature actuelle suggère que la chimie théorique, le niveau élevé de la théorie de la structure démarche électroniques utilisés par Sinnokrot et al et Tsuzuki et al donne un modèle précis de π -stacking interaction. Cependant le coût de calcul signifie pas qu'il ne peut pas être appliquée à de nombreux grands systèmes que nous envisageons ici, tels que le PPV-nanotubes interactions. Par conséquent, une approche plus simple et moins exigeante de calcul est nécessaire. Le seul moyen théorique pour comprendre plus π - π systèmes grâce à l'utilisation de la technique de la fonctionnelle

de densité dont les échelles beaucoup moins critique avec la taille ensemble de base que les méthodes d'onde avancées fonctionnelles.

Pour cette raison nous benchmark ici l'approche DFT / LDA contre ces techniques plus complexes.

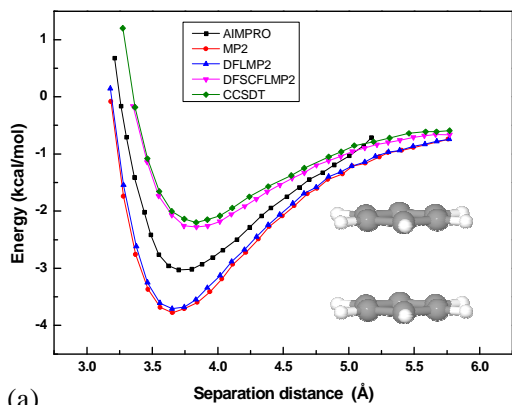
Notre approche est pragmatique, plus proche de l'expérimentation numérique: La question que nous posons est, dans quelle mesure peut plus simple d'échange-corrélation description telle que LDA se reproduire avec succès π - π d'interaction pour les systèmes très grands?

Method	T-shaped	Parallel displaced (PD)	Parallel stacked (PS)
This work	-4.250	-3.371	-2.501
CCSD(T)	-2.492	-2.513	-1.564
DF-LMP2	-3.503	-4.427	-3.147
DF-SCF-LMP2	-2.436	-2.604	-1.833
MP2	-3.516	-4.324	-3.222

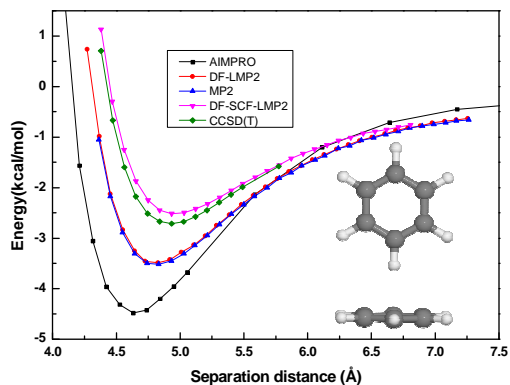
Énergies Interaction (kcal mol⁻¹) pour une configuration différente du benzène dimère comparer avec ce travail et d'autres méthodes prises à partir

Method	T-shaped	Parallel displaced	Parallel stacked
This work	4.89	3.52	3.71
CCSD(T) [14]	5.00	3.60	3.90
DF-LMP2 [16]	4.89	3.70	3.72
DF-SCF-LMP2 [16]	5.04	3.54	3.89
MP2 [14]	4.90	3.40	3.70

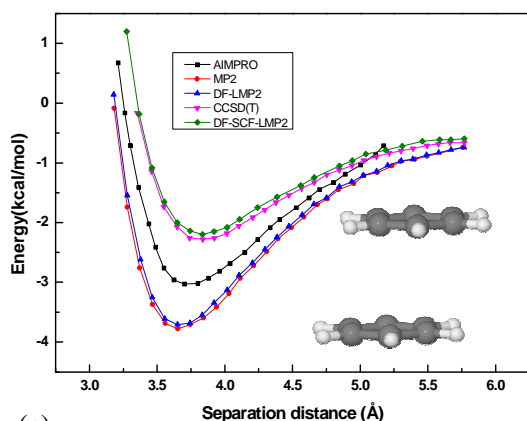
Distance interatomique, R_1 (Å) pour ce travail par rapport à d'autres méthodes



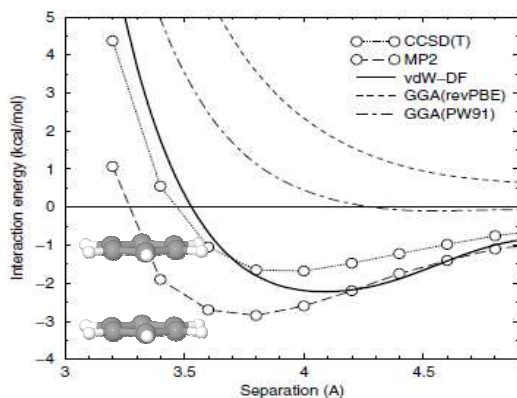
(a)



(b)



(c)



(d)

Comparaison des courbes d'énergie potentielle pour (a) en parallèle empilés, (b) en forme de T, (c) des dimères de benzène parallèle entre ce travail déplacées (AIMPRO) avec celle de CCSD (T), MP2, DF-LMP2, DF -SCF-LMP2 résultats de Grant et Aland (d) compare les résultats de CCSD (T), MP2, vdW-DF avec celle de deux GGAS revPDE et PW91 prises de travaux de Dion et al.

La majorité des études sur l'interaction concentrent benzène benzène sur quelques configurations haute symétrie. La vitesse relative de nos techniques nous permet d'explorer plus en détail la surface d'énergie potentielle pour le benzène-benzène interaction. Nous avons tracé l'énergie pour les deux anneaux de benzène en fonction de leur centre à centre de déplacement dans un point de grille du plan xy avec la séparation interplanaires z autorisé à varier librement, tout en fixant le mouvement du dimère dans les directions xy. La carte montrant le contour du dimère du benzène au moins et les plus stables. L'intrigue confirme que la configuration la plus stable est le dimère en forme de T. Le dimère PS dans

les régions rouges de la carte est défavorisée en raison de π -électron répulsions (compétition entre la répulsion et l'échange Pauli effets électrostatiques dans le dimère). Comme les arrangements deviennent empilage offset, ce qui conduit à d'autres structures de l'Etat de transition avec l'énergie répulsive beaucoup plus faible que les structures initiales jusqu'à ce qu'on atteigne finalement la forme stable qui est le parallèle déplacées (PS) dimère (0,15 eV plus stable que deux molécules de benzène isolées), dans lequel les effets électrostatiques sont minimisés en raison du décalage dans les plans dimère. Orbitales remplies, puis se chevauchent, dans le même temps menant à la minimisation de la répulsion de Pauli échanges avec la conformation la plus favorable dans les régions bleues de la carte. Pour le bord-à-face (en forme de T dimère), il ya une forte attraction dipôle entre l'atome d'hydrogène d'un monomère pointant vers le centre d'un autre monomère qui constitue une interaction σ - π , dans un système de 0,2 eV plus stable que deux molécules de benzène isolées avec dimère plus favorisée dans la région du bleu de la carte. Comme les deux positions sont changées monomère à savoir des régions bleu sur la carte par rapport aux plans XY, d'autres structures à faible énergie de liaison sont vu (les autres couleurs de la carte) jusqu'à un état défavorable est atteint. A ce stade, on voit que, les dimères sont totalement déplacés de la position initiale favorable, et les molécules de benzène ne sont plus en interaction due à leur éloignement.

Nous avons ensuite examiné la liaison entre le graphène et le benzène. Nous avons placé le benzène sur une cellule grande unité composée de 128 atomes de graphène et déplacé latéralement le benzène dans les directions (x et y). A chaque point du graphène a eu lieu fixe et tous les atomes du benzène fixés dans le x et directions y, mais autorisés à circuler librement dans la direction z.

Figure ci-dessous est la carte de contour résultante parcelle pour interagir graphène avec une molécule de benzène. L'interaction montre un arrangement moléculaire similaire à celle du dimère du benzène décrits ci-dessus. Pour l'orientation en forme de T, la géométrie la plus favorable est lorsque la molécule de benzène est positionné au centre d'un hexagone le graphène, qui se traduit par une liaison plus élevée pour cette conformation, qui est plus stable 0.10eV (région bleue) que la conformation d'autres (zone rouge). Contrairement au cas

du benzène-benzène empilage, cette fois la configuration parallèle est plus stable que la géométrie en forme de T.

Lorsque les molécules de benzène sont parallèles empilés sur une feuille de graphène, l'orientation la plus stable, c'est quand le parallèle empiler les commutateurs à une conformation PD (dans lequel le centre de l'anneau aromatique est positionné sur le dessus d'un carbone graphène semblable à AB en graphite empilage), ce qui est de 0,10 eV plus stable que la configuration PS (équivalent à AA empilage). Le benzène est physisorbé sur le graphène, produisant une géométrie parallèle dans lequel on trouve l'adsorbat à être positionné 3,27 Å dessus de la surface en bon accord avec 3,24 la valeur d'une rapportés par Rochefort et al utilisant LDA. Cette distance entre le graphène et le benzène est plus petit par rapport à la distance de 3,71 Å intercalaire nous avons obtenus pour le benzène dimère parallèles empilés, et est proche de l'espacement intercouche pour AB-graphite hexagonal de 3,35 Å.

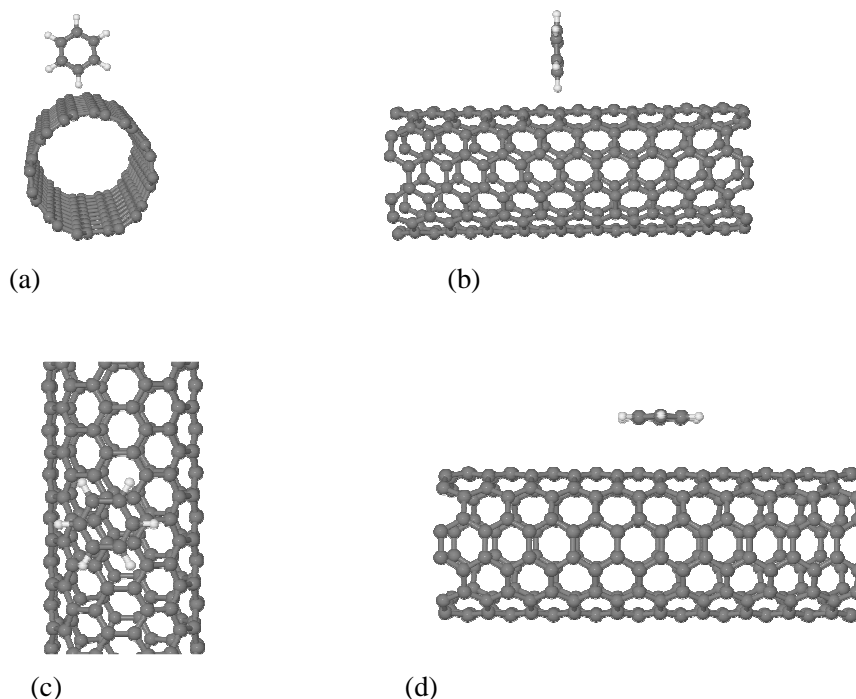
L'adsorption du benzène sur du graphite rapportés dans la littérature donne des valeurs d'énergie de liaison pour les deux sites d'adsorption les plus stables (PS et PD) de 0,229 à 0,350 eV avec LDA et la valeur expérimentale est de 0,45 eV qui sont en accord étroit avec notre énergie de liaison de 0,38 eV.

Parallèlement empilage de benzène avec le graphène est beaucoup plus stable que perpendiculaire, à la différence de benzène-benzène interaction dans laquelle la perpendiculaire est plus stable. Ces différences peuvent survenir dans l'interaction graphène benzène, la géométrie parallèles empilées qui maximise l'effet de π - π interactions empilage tandis que dans le second, ce n'est pas le cas. De plus, tous les atomes de carbone dans le graphène sont neutres, ce qui réduit les interactions dipolaires dans la configuration perpendiculaire par rapport au benzène-benzène interactions.

Ce travail est aussi d'accord avec les études théoriques par Olga et al., Sur l'adsorption de benzène et de ovalene parallèle à l'hydrogène feuille de graphène résilié. Ils ont constaté que, tant le ovalene et le benzène préféré l'AB-empilage, qui est le minimum global, mais pas l'AA-stacking qui est un maximum global.

Les composés aromatiques sont connus pour interagir avec le graphite et aussi avec les flancs graphitiques des nanotubes de carbone. Cette interaction ne perturbe pas la conjugaison aromatique des systèmes du réseau et est donc idéale pour des applications telles que l'électronique et d'autres où la fonctionnalisation non covalente est nécessaire. Cependant la présence de molécules aromatiques sur le flanc d'un CNT pourrait modifier leur transport et leurs propriétés électroniques.

Molécule de benzène d'adsorption sur le fauteuil de [(4,4), (6,6)] et en zigzag [(7,0), (13,0)] NTC ont été calculées avec la molécule de benzène soit perpendiculairement au-dessus du trou hexagonal du SWCNTs, au-dessus un atome de carbone SWCNT ou parallèles empilés (avec le centre des molécules de benzène juste au-dessus d'un atome de la CNT). Dans le tableau ci-dessous pour chaque tube, les énergies de liaison, après la détente la géométrie sont comparés avec le benzène orientée sur le graphène dans la pile en parallèle et l'orientation perpendiculaire.



Optimisation du benzène sur la géométrie (6,6) SWCNTs avec (a) vue de dessus, vue de côté (b) pour le benzène perpendiculaire SWCNTs et (c) vue de dessus, vue de côté (d) pour le benzène / SWCNT en conformation parallèles empilés.

Tube (n,m)	Diameter (Å)	Stacking Binding energy (eV)	Perpendicular (hexagon centers) Binding (eV)	Perpendicular (on carbon) Binding (eV)
(4,4)	5.43	0.19	0.16	0.14
(6,6)	8.14	0.25	0.13	0.13
(7,0)	5.48	0.18	0.11	0.12
(13,0)	10.18	0.26	0.10	0.10
Graphene	-	0.38	0.19	0.15

L'énergie de liaison pour l'orientation des différents molécule de benzène sur des nanotubes de différents diamètres différents en comparaison avec du benzène orienté sur feuille de graphène.

Dans tous les conformations étudiées la plus favorable est le PD (on-top de conformation) à plus haute énergie de liaison par rapport à l'orientation perpendiculaire de plus de 0,15 eV plus élevée dans le cas de tubes de grand diamètre. C'est la même conformation que le benzène sur le graphène avec ce dernier ayant une plus grande énergie de liaison que le benzène sur la NTC. Tableau 13 peuvent être résumées comme suit: (i) de liaison est plus faible à la plus petite des tubes, (ii) les augmentations obligatoires de diamètre (iii) même sur de grands tubes est de moins de graphène. Cela implique que la courbure est important pour la conjugaison (il diminue), sur des tubes de petit diamètre, π empilement est endommagé, et enfin (iv) le benzène perpendiculaires au dessus du trou hexagonal du SWCNTs ou quand un atome d'hydrogène du benzène est placé directement au dessus d'un atome de carbone de l'SWNTs, il n'ya pas de différence significative observée dans la liaison entre les deux conformations, mais il semble y avoir une préférence pour les tubes métalliques dans cette conformation par rapport aux tubes semi-conducteurs. C'est peut être parce charge dans les tubes métalliques peuvent redistribuer plus facilement d'interagir avec le $+\delta$ sur l'hydrogène. Nos résultats théoriques sont en accord avec le calcul théorique du benzène sur des nanotubes de différent par Tournus et al. qui ont trouvé la conformation parallèles empilés à venir comme le plus favorable avec un diamètre de plus en plus les nanotubes.

Ceci est un polymère attrayant pour l'étude théorique des propriétés des polymères conjugués, car elle prend la forme d'assez simple quasi-unidimensionnels molécules

disposées en une structure cristalline en 3D. Ces arrangements permettent donc pas d'étudier les caractéristiques conformationnelles et électroniques à la fois des chaînes de cristaux isolés et des polymères PPV.

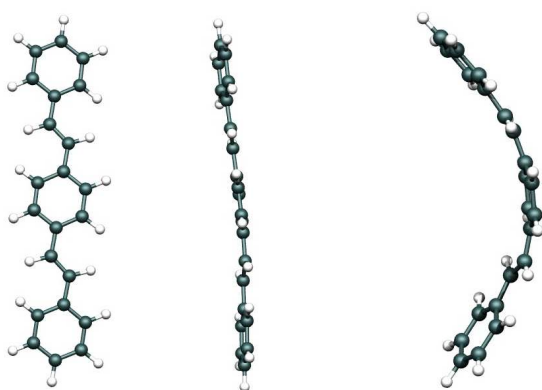
PPV a des groupes aromatiques dans sa longueur de la chaîne qui la rend plus rigide et principalement responsable de la plupart des interactions non covalentes de ces polymères. Les propriétés physiques des matériaux polymères sont également régis par des interactions polymère-polymère. Ceci peut être dominé par les interactions dipôle-dipôle, la répulsion échange de constituants atomiques, répulsion stérique et des mécanismes de liaison hydrogène. Ce comportement de leurs interactions est principalement associée aux électrons locaux ou non locaux des polymères.

Même s'il ya eu quelques études théoriques sur ces types de polymères, les principaux mécanismes permettant de comprendre l'interaction de ces polymères est souvent absente, en raison de l'utilisation de techniques simples de calcul comme base des approches de champ de force et empirique de mécanique moléculaire qui ne prendre en compte la description électronique de ces polymères conjugués.

Ainsi, beaucoup de ces interactions peuvent être compris par la modélisation mécanique quantique pour calculer leurs effets, donnant ainsi à l'origine et la nature de ces interactions.

La chaîne isolée PPV étudiés dans ce travail est constitué d'un monomère répéter 3-phényle. Nous étudions deux configurations différentes composées de configurations à plat et plié. Après la détente atomique, nous trouvons la conformation plane à 0,30 eV plus stable que la conformation pliée méta-stable. Ceci est en accord avec les études théoriques par Zheng et al., Où ils trouvèrent l'unité monomère isolés pour être plane ou plate et la plus stable. Nous trouvons également un très petit angle de torsion de 8 ° stabilise légèrement la molécule supplémentaire. En effet, des études de diffraction expérimentaux suggèrent un angle de torsion d'environ 5 ° par monomère PPV dans les avions qui augmente avec la température. En général, pour PPV deux mécanismes concurrents peuvent être vus à se produire; (1) pour π étendu-conjugaison à produire de la chaîne de télévision à la carte doit être planaire et (2) l'encombrement stérique survenant entre l'anneau benzénique et le lien vinyle à certains

égards en faveur d'une non planaire de conformation, qui pourrait aussi venir avec un coût énergétique (que nous avons calculé à 0,12 eV) voir ci-dessous.

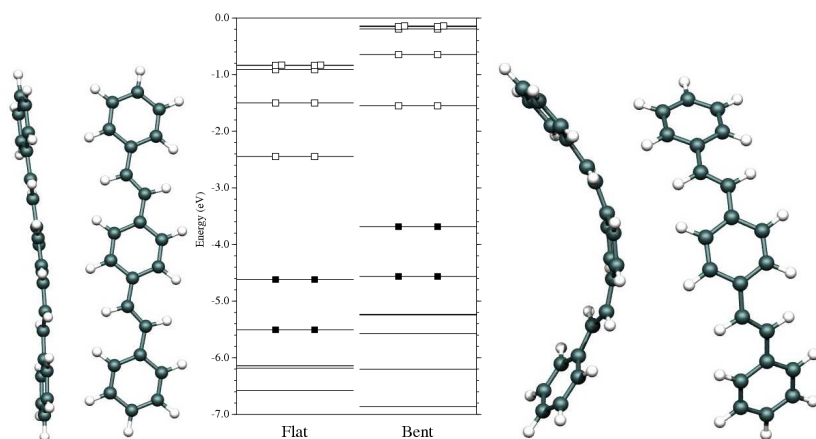


Optimisé pour les géométries 3-phényl unités monomères répétition de PPV avec ((une vue) à l'avant de la géométrie plane, vue de côté (b) de la configuration stable planaire et ((c)-vue de côté, (D)-vue de face) d'un méta-stables de configuration pliée. (0,30 eV moins stable que (b) qui est le plus stable, avec une légère torsion de torsion dans nos calculs de 8 ° par monomère PPV.

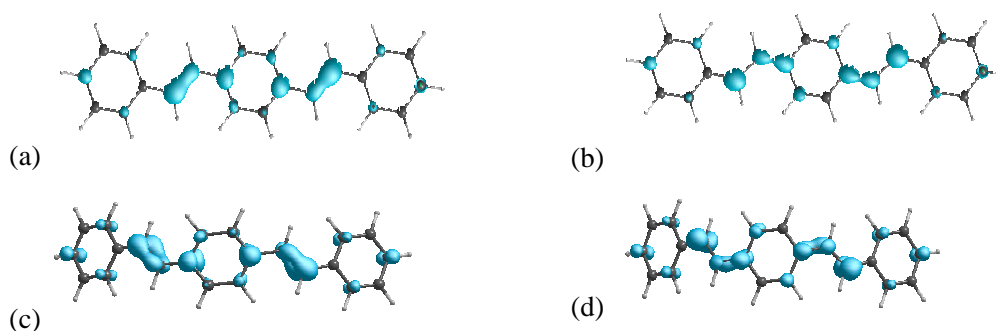
Comme il ya huit atomes de carbone dans une cellule de PPV unité de répétition, mais un seul électron par atome de carbone peut prendre part à collage conjugué π , et parce que chaque niveau d'énergie peut prendre un maximum de deux électrons, ce qui implique que seuls quatre états de valence π , avec plus basse énergie sont remplis et que les quatre états π^* bande de conduction sera vide par maille. Cela signifie que le noyau benzénique contribue trois π -paires électron et le reste π paire électron-vient de la liaison vinyène, (voir ci-dessous pour la structure de bande de molécules PPV).

La bande LDA pour les deux configurations a été calculé: celui de la VPP planaire est 2.17eV, et la VPP est plié 2.13eV avec la bande expérimentale donnée comme 2.5eV. Dans la configuration plié les niveaux d'énergie sont toutes décalées vers le haut par environ 0.9eV en ce qui concerne le niveau d'énergie de la configuration à plat. Un calcul théorique précédente de la bande pour une chaîne oligomère PPV a été trouvé que 1,3 eV. La valeur de la bande à faible écart obtenu par ce groupe

pourrait être due à leur utilisation d'une chaîne infinie dans leur calcul qui donnerait une plus faible écart. Notre chaîne courte introduit des effets de confinement qui peut ouvrir l'écart plus large. Comparé à la valeur d'autres théoriques, notre valeur calculée pour la bande correspond étroitement à la valeur expérimentale de 2,5 eV.



Niveaux d'énergie pour moléculaire (unité de la chaîne 3-phényl) PPV, dans (à gauche) de la configuration plane et stable, et (à droite) une méta-stables de configuration pliée. Dans les deux cas, l'écart reste autour 2.15eV, mais une fois pliés, les niveaux sont décalées vers le haut en énergie. [Les carrés noirs indiquent les états et les carrés blancs remplis états vides]



Place de la fonction d'onde pour les isosurfaces HOMO (a), LUMO (b) pour planaire isolée PPV de la chaîne et Homo (c), LUMO (d) pour plié PPV chaîne isolée.

L'intrigue de la fonction d'onde de densité de charge isosurfaces pour la plus haute orbitale moléculaire occupée de l'(HOMO) et le plus bas des orbitales moléculaires inoccupées (LUMO) sont indiqués pour les deux planaires et courbé méta-stables chaînes de PPV isolés. Pour les PPV planes, l'état HOMO (a) est délocalisée avec la plupart des Etats sur les liens vinylène, mais dans l'état LUMO (b) il n'ya pas d'Etat sur le lien vinylène mais sur la liaison CC simple entre l'anneau benzénique et que des le carbone vinylène parce que c'est un collage anti-orbitaux.

Un effet similaire a été observée dans la méta-stables pliés isolés PPV pour l'Homo état (c) et (b) LUMO. Cependant l'augmentation de répulsion stérique entre les atomes voisins en raison de la courbure de la chaîne PPV couplé avec le raccourcissement des doubles liaisons induites par la flexion pourrait rendre compte de l'évolution des niveaux d'énergie de 0,9 eV que nous avons calculé comparer à la conformation plane.

Ayant établi que la chaîne PPV planaire isolée est la forme la plus stable, nous avons ensuite passé à étudier les effets de l'empilement de deux VPP planaire en géométrie parallèle empilés et en forme de T et également l'interaction de ce polymère avec des feuilles de graphène et les nanotubes de diamètre différent , comme décrit ci-dessous.

PPV est connu pour avoir la structure en forme de T que sa structure cristalline solide (chevrons, illustré ci-dessous).

Les interactions entre deux VPP (unité de répétition 3-phényl) dans AA-empilés et en forme de T configurations ont été étudiées en faisant varier leurs positions sur une grille de points (plan xy) pour déterminer la conformation la plus stable à chaque configuration, d'une façon similaire à notre traitement antérieur de benzène. Une des chaînes PPV a été gelés alors que dans l'autre chaîne PPV deux atomes à l'extrémité de chaque couplage de vinyle ont été contraints dans les directions xy mais a permis d'optimiser librement dans la direction z. Tous les autres atomes dans la chaîne de deuxième PPV ont été autorisés à circuler librement.



Structure cristalline chevrons de PPV dans les directions X et Y. Où $\Phi = 52^\circ$

Ce qui précède montre que le PPV empilés dans une forme en T et PS-configuration sont celles qui conduisent à des structures moins d'énergie semblable à celle du benzène-benzène et du benzène graphène discuté précédemment. Comme pour le benzène benzène, l'énergie des structures en forme de T et PS sont très similaires, à la différence de benzène graphène. Énergies de liaison sont environ trois fois supérieurs à ceux du benzène, ce qui est cohérent parce que la molécule est environ trois fois et demie plus gros. Contrairement benzène benzène, dans ce cas, le parallèle est un peu empilés plus énergiquement favorisées que la perpendiculaire d'empilage. C'est à cause de l'augmentation de π - π aromaticité.

Comme les deux PPV qui interagissent dans le PS sont déplacés dans le plan xy, ils atteignent une conformation où le PPV-dimères assumer un "AB-graphite" configuration de type ie une conformation décalée, ce qui minimise la répulsion stérique entre les hydrogènes à la périphérie de les cycles aromatiques (carte-(b)). Pour la forme de T (carte-(a)), la structure minimale d'énergie est formé lorsque les hydrogènes-dessus de la couronne hexagonale d'un point de molécules PPV directement au milieu de la couronne hexagonale de la molécule d'autres PPV ci-dessous.

Ainsi, ces résultats montrent que le PPV PPV interaction est semblable à du benzène-benzène interaction avec empilage désormais favoriser une conformation parallèles plus graphitique. Nous passons ensuite notre attention sur l'interaction du graphène avec PPV.

Notre tracé de contours pour l'interaction du graphène avec le PPV est donnée ci-dessus. Ceci a été obtenu en utilisant la procédure décrite précédemment dans laquelle la feuille de graphène a été gardé congelé pendant le cycle d'optimisation de contraintes appliquées dans les PPV en construisant une grille de points dans le plan xy et ensuite ce qui lui permet de se déplacer librement dans la direction z pendant la relaxation.

Comme pour le benzène sur le graphène, les structures parallèles empilées sont beaucoup plus stables. Forme de T, la géométrie montre une faible liaison que la configuration parallèle, semblable à du benzène.

Le maximum global (moins stable) correspond à la position PS dans lequel tous les atomes dans les couches voisines se font face, qui est normalement une «AA-stacking" conformation de type avec un espacement de 3,51 Å intercalaire entre les molécules et la surface avec énergie de liaison de 0,5 eV. Le minimum global (plus stable) correspond à celle du PS d'adopter le parallèle décalées (PD) de la conformation (graphite AB-empilé conformation) avec un 0,2 eV plus contraignante et un espacement de 3,22 Å intercalaire.

Le tracé de contours suggère qu'il ya un coût énergétique dans le déplacement de la géométrie AB-empilage à un AA-empilage. Ceci définit alors la plus grande barrière de différence d'énergie entre l'AA et AB-empilement pour le PPV étant parallèles sur une feuille de graphène. Ensuite, nous avons calculé la force de frottement coulissant impliquer dans la VPP sur le graphène à partir de la position minimum global, AB-empilés, au global maximum, AA-empilage. C'est le différentiel de la parcelle d'énergie.

Comme prévu, à l'AB-empilage, ce qui correspond à la structure minimale d'énergie, la force de frottement est égal à zéro (0 N). Une force de 0,13 nN sera nécessaire pour faire glisser le PPV directement à partir de la position stable pour le maximum d'énergie AA-empilage de conformation qui est improbable. Cependant, dans la position d'énergie minimale, il sera beaucoup plus facile de faire glisser le PPV sur le graphène entre les configurations AB qui nécessitent une force plus petite (0,04 NN).

Ceci est important pour une application composite et cela peut être comparé à des expériences où l'effet synergique sur les composites de cette nature aura une résistance mécanique plus élevée dans lequel l'interface entre le PPV et la forme de graphène un modèle

AB-empilage.

Ces résultats sont globalement d'accord avec les études expérimentales sur les mécanismes de friction entre flocons de graphène petites et graphites en utilisant un microscope à force de friction qui permet d'obtenir une résolution au sein des forces latérales à 15 pN. On a constaté qu'il ya une forte dépendance du frottement sur l'orientation des molécules. La force de friction est maximale lorsque l'angle d'orientation, qui définit le désaccord de maille entre les flocons et le substrat, était nul ou 60° signifie la diapositive flocons sur toute la surface de graphite en contact correspondant. Comportement au frottement ultra-faible et glissant amélioré a été observée lorsque le flocon glisse sur la surface de graphite dans un contact incommensurable. Cependant nous constatons que nous n'avons pas regardé tournant le PPV en raison de contraintes de temps.

Une étude théorique sur l'adsorption de l'hydrogène sur le graphite HAP résilié montre qu'il ya une grande force dans le déplacement d'une orientation AB-cumul de ces HAP à AA-empilage, ce qui s'accorde avec nos études.

Même si il ya un vif intérêt dans l'exploitation des nouvelles propriétés des nanotubes de carbone dans les appareils électriques et mécaniques, la réalisation de ces applications est jusqu'ici très limité, car les NTC sont hautement hydrophobes et forment souvent des agrégats insolubles. La présence de tubes multiples chiralité présente également un problème dans la réalisation des applications potentielles des nanotubes de carbone. Deux obstacles importants de l'hydrophobie et l'hétérogénéité conformationnelle dans les deux aqueux et non aqueux posent des défis considérables pour leur séparation et de réunion et donc de limiter leur très envisagé applicabilité.

Par conséquent, la solubilité de ces tubes peut être améliorée par la modification chimique de SWCNTs, par fonctionnalisation covalente en utilisant des polymères, des groupes phényle substitué, et d'autres groupes substituants nombreuses. De cette manière, la méthode chimique peuvent perturber la structure électronique des nanotubes et pour le pire des cas va conduire à la destruction des tubes.

Non modification covalente est l'un de l'approche la plus largement utilisée pour séparer des faisceaux de nanotubes et de faire des tubes individuels. Parce que les propriétés

électroniques des tubes restent intactes, ce qui a attiré beaucoup d'études ont comparé les méthodes de fonctionnalisation covalente. Il est largement admis que la liaison interfaciale entre NTC et la matrice polymère de contrôle de l'efficacité des transferts de charge et, depuis les NTC sont connus pour avoir une distribution de charge uniforme, il n'y a guère d'interactions électrostatiques entre les nanotubes et les polymères, ce qui signifie en l'absence de fonctionnalisation chimique, π - π empilage va dominer les interactions. Dans ces cas, la force de liaison interfaciale dépendra donc de la géométrie de conformation du polymère à l'égard des nanotubes.

Il est donc important d'explorer la possibilité d'optimiser les interactions intermoléculaires non covalentes entre les NTC et de polymères afin de parvenir à une forte transferts interfaciaux.

Dans cette section, nous étudions la relation entre les différentes géométries de PPV polymères interagissant avec des diamètres différents et SWCNTs graphène, en utilisant le code AIMPRO et aussi, en comparant nos calculs avec les résultats expérimentaux disponibles à partir de notre groupe.

Polymères conjugués ont été montré à exposer une bonne liaison avec les SWCNTs et des études de microscopie électronique ont montré l'emballage de SWCNTs par plusieurs polymères.

La modélisation théorique des nanotubes de carbone en interaction avec l'ADN simple brin ont montré que, il se lie à des nanotubes dans un emballage hélicoïdale à la surface, par l'intermédiaire π - π empilage dans lequel l'ADN a été démontrée à fournir un tube dans lequel réside le nanotube, ce qui rend elle soluble dans l'eau. En outre, Lordi et Yao, champ de force utilisé moléculaire à base de calculs de mécanique afin de déterminer la résistance interfaciale et la morphologie de la conformation de polymère sur SWCNTs et ils ont trouvé que, pour un polymère de la morphologie hélicoïdale enveloppant autour de la SWCNTs est le facteur le plus important pour la construction de nanocomposites ultraforte, tandis que l'énergie interfaciale liant joue un rôle mineur. Par ailleurs, en utilisant simulations de dynamique moléculaire, d'autres auteurs ont étudié les interactions entre un ou deux

polymères qui interagissent avec des nanotubes. Même si certaines de ces études ne peuvent pas représenter les propriétés nanocomposites en vrac, ils donnent toutefois des informations utiles sur la nature de l'interface entre le polymère et de nanotubes. Yang et ses collègues ont étudié l'interaction entre le poly (styrène) PS, le poly (phénylacétylène) (APP), le poly (para phénylène vinylène) (PPV) et SWCNTs utilisant la dynamique moléculaire; ils ont constaté que la structure monomère joue un rôle essentiel dans la détermination la force de l'interaction entre les SWCNTs et de polymère. Basé sur leurs simulations, ils ont suggéré que les polymères avec des dorsales contenant des cycles aromatiques sont beaucoup prometteuse pour la liaison non covalente de NTC dans des structures composites. McCarthy et ses collègues [61] a noté que la force motrice pour l'adsorption de polymères peuvent dicter la conformation de l'importance relative de polymère à la CNT, et d'autres études ont indiqué que la structure CNT peut également dicter les caractéristiques conformationnelles des molécules adsorbées.

Simulations de dynamique moléculaire par Liu et ses collègues, seulement observé emballage hélicoïdal pour chaînes simples d'oligomères de dorsales rigides, qui sont également déterminés à être sensible à l'arrangement conformationnel des unités répétitives au sein de la chaîne.

Les matériaux composites basées sur l'emballage en polymère de multi-parois na Ce travail a utilisé le procédé électronique ab initio structure de calcul (AIMPRO / LDA) et expérimentale de spectroscopie Raman pour étudier les structures et les propriétés des complexes interagissant faiblement, en faisant usage de quelques exemples précis à partir du carbone basée Nanoscale Science des matériaux.

En utilisant une approche DFT / LDA nous sommes en mesure de fournir une compréhension fiable et améliorée de la nature des interactions intermoléculaires faibles tels que les interactions dipôle-dipôle, π - π empilage, de transfert de charge complexe et H- π . Ces interactions sont d'une grande importance dans de nombreuses disciplines des sciences et de jouer un rôle majeur dans les processus de reconnaissance biologique et moléculaire.

Nous avons d'abord examiné l'interaction de molécules de brome (orientés parallèlement et perpendiculairement) avec le graphite, le graphène et les nanotubes de carbone à paroi

unique. Pour l'adsorption de brome sur le graphène, nous avons trouvé pour la première fois que lorsque les molécules de brome sont orientées perpendiculairement à la surface du graphène ils forment un dipôle avec un transfert de charge solide. La molécule forme un ($\text{Br}^+ + \text{Br}^-$) paire rendant infra-rouge actif, et résultant en une ouverture petite bande dans le graphène sous-jacent (86meV). C'est donc une nouvelle forme de brome qui était auparavant considéré que comme une saturation de carbone intermédiaires instables au brome induite obligatoires. Nos résultats montrent une différence possible entre le comportement inattendu dans le graphène et le graphite. Il serait très utile pour tester la prédiction de l'activité IR expérimentalement. Cela devrait être facilité par le fait que les deux graphène brome liquide et isolés sont inactifs et donc IR seulement le Br_2 surface doit avoir une forte capacité d'adsorption. Où Br_2 est parallèle à la graphène, aucun dipôle se produit, mais une distribution de charge symétrique de transfert entre la paire d'atomes de brome et le graphène est observée. Notre calcul des énergies de liaison montrent que l'orientation parallèle est de 0,15 eV moins stable que l'orientation perpendiculaire Mais cette différence est assez petit pour que, nous proposons que, à température ambiante, ces structures pourraient être en alternance en raison d'un mouvement de tumbling de l' Br_2 . Dans le graphite, le brome molécules adoptent une orientation parallèle aux fiches avec un transfert de charge associés et ceci est en accord avec les données expérimentales lorsqu'elles sont disponibles. Énergies de liaison pour les deux étapes-1 ($\text{Br}_2 / \text{AA-graphite}$) et de stade 2 ($\text{Br}_2 / \text{AABB}$) ont été calculés pour être endothermique à faible couverture de Br_2 en raison de l'énergie de liaison du $\text{Br}_2/\text{graphite}$ ne pas être capable de compenser la séparation intercalaire d'énergie pour le graphite: ce qui a été calculée comme 36,74 meV / atome pour AB et avec AA-être 12 MeV / atome moins stable. Cependant, après bromation il ya une stabilité préférentiel pour AA-empilage de chaque côté de la couche intercalé brome. Ces calculs actuels ne semblent pas fournir une réponse pour expliquer pourquoi l'étape-1 de graphite bromés n'est pas stable, et cela est clairement un domaine d'études ultérieures. Pour les nanotubes, quand le brome a été orientées perpendiculairement aux tubes isolés, il se comporte même comme avec le graphène. Lorsque la CNT sont en ballots Br_2 s'intercale dans les faisceaux similaire à Br_2 graphites intercalés parallèle à l'hexagone. Par extension similaire, nous supposons que le

même phénomène va se passer pour les nanotubes de carbone à double paroi.

A une concentration élevée Br_2 , structures de la chaîne polybromure sera thermodynamiquement favorable. Mais, la formation de ces structures de la chaîne de brome n'est pas spontanée. Il ya une barrière d'activation calculée comme -27.01kJ/mol donc cinétiquement ces structures de la chaîne ne sera pas réalisable dans les conditions ambiantes. Cette barrière est due à l'interaction entre les molécules de brome Coulomb ainsi que des trous voisins dans le graphène comme un résultat de transfert de charge du brome. Ceci suggère la possibilité intrigante que les systèmes de chauffage brome / carbone dans un système fermé (par exemple sous pression) pour éviter la perte de brome peut encourager la formation de chaînes polybromure. Les résultats calculés montrent que, physisorption ne résulte pas en un changement notable dans la géométrie des substrats tels que le graphène, de graphite et de nanotubes. Et à cause de l'inertie chimique de ces matériaux en carbone, l'énergie de liaison ne dépend que de la zone de contact entre le substrat et adsorbats.

Deuxièmement, nous avons étudié les interactions π - π empilement entre PPV oligomère chaîne avec le graphène, PPV et SWCNTs de diamètre différent et chiralité. Nous avons d'abord considéré comme le plus simple prototype de π aromatiques π -interaction, le dimère du benzène et nous avons trouvé des structures d'énergie minimale que la forme de T (T) et en parallèle décalées (PD) avec des conformations état de transition est le parallèle de pile (SP) conformations . En chimiques complexes différents et les systèmes biologiques, cycles aromatiques peuvent être trouvés à différentes orientations et les distances les uns des autres, qui pourraient ne pas correspondre au potentiel des minima d'énergie pour π - π interactions. Néanmoins, les cycles aromatiques peut toujours interagir assez favorablement pour contribuer de manière significative à la stabilité globale du système. Par conséquent, il est essentiel d'obtenir les courbes d'énergie potentielle pour les systèmes de prototype afin de déterminer comment les interactions π - π dépendent à la fois l'orientation et la distance entre ces cycles aromatiques. Pour atteindre cet objectif, nous avons calculé les courbes d'énergie potentielle en fonction des distances intermonomère pour trois configurations importantes de benzène dimère, à savoir la pile parallèle (PS), la forme de T (T), et en parallèle décalées (PD) de configurations . Cela a également été vu dans le complot carte de contour avec des

structures métastables d'autres énergies. Avec le benzène sur le graphène et SWCNTs, l'arrangement de l'empilement a été jugée comme AB-graphite conformation qui est le plus favorisé avec le moins favorisées étant la conformation AA-empilage qui a une énergie plus élevée et par conséquent, n'aura pas lieu pour l'adsorption des benzène.

Aussi, nous avons remarqué que, l'interaction entre les molécules PPV deux est différent de PPV-SWCNTs ou PPV-graphène. Dans le premier cas, les orientations parallèles et perpendiculaires ont des énergies similaires à un type d'arrangement perpendiculaire survenant dans l'empilement cristallin de ces polymères et d'autres hydrocarbures aromatiques polycycliques. Mais pour le PPV-SWCNTs ou PPV-graphène, la conformation la plus favorisée, c'est quand la VPP est orienté parallèlement sur ces substrats. Molecule / molécule d'interaction semble être fondamentalement différente de la molécule / substrat. Dans le cas des nanotubes, la dépendance énergétique contraignant sur l'orientation de PPV avec diamètre décroissant a été observée. Wavefunction isosurfaces parcelle de quelques interactions choisies entre SWCNTs / PPV, suggèrent très peu d'effet sur le couplage électronique à proximité du niveau de Fermi entre le PPV et SWCNTs. Cela implique que la fonctionnalisation non covalente par π -stacking est catégoriquement différent de fonctionnalisation covalente. Il préserve les propriétés des SWCNTs qui peut fournir une opportunité pour adapter le nanotube dans l'application spécifique d'autres tels que l'électronique, où l'intégrité structurale est très important.

Dans cette thèse, nous avons montré que le code AIMPRO, basé sur la théorie DFT / LDA peut être utilisé pour donner un aperçu sur les interactions faibles qui peuvent survenir entre les nanosystèmes de carbone (graphites, graphènes et SWCNTs) et des molécules telles que le brome, le benzène et PPV. Ces nanosystèmes de carbone peuvent être décrites comme des espèces de carbone sp^2 hybridés dans lequel LDA a prouvé à bien décrire un tel formulaire hybridées de matériaux en carbone et donc notre justification pour l'utilisation de l'approche LDA et sa capacité à traiter de plus grands systèmes de cette nature avec beaucoup moins de calcul efforts par rapport à des niveaux plus élevés de la théorie.

Ces nanosystèmes de carbone peuvent être décrites comme des espèces de carbone sp^2 hybridés dans lequel LDA a prouvé à bien décrire un tel formulaire hybridées de matériaux en carbone et donc notre justification pour l'utilisation de l'approche LDA et sa capacité à traiter de plus grands systèmes de cette nature avec beaucoup moins de calcul efforts par rapport à des niveaux plus élevés de la théorie.

Autres orientations futures de cette recherche sont les suivants;

1. La LDA utilisée dans cette thèse a pas de terme de correction de dispersion. Il sera utile de comparer les énergies de liaison dans ces résultats LDA avec celle d'une approche de force de dispersion corrigée (qui est dans sa phase finale de test avant la sortie dans notre code AIMPRO).
2. Il sera intéressant de varier la longueur de la chaîne de polymère de l'oligomère PPV utilisés à partir de deux chaînes oligomères jusqu'à dix chaînes oligomères de voir s'il y aura des variations dans l'alignement des chaînes de PPV avec SWCNTs que le nombre de cycles phényle augmente.
3. Nos tracés de contours ne montrent que la variation d'énergie de liaison en fonction de la traduction moléculaire, et il serait intéressant d'étudier l'effet de la rotation moléculaire ainsi.
4. Nos collègues d'expérimentation dans le travail de groupe avec un PPV PMN pré-curseur, MEH-PPV, et ils sont désireux de nous le modèle de son interaction avec des nanotubes pour la comparaison avec celle du PPV-SWCNT. Il existe d'autres polymères conjugués intéressantes on pourrait aussi envisager.
5. Notre calcul de la force pour déplacer PPV sur la surface du graphène donne une prédiction directe de la force de frottement de glisser PPV sur le graphène et cela pourrait être important pour les applications des nanocomposites. Il est aussi nécessaire de confirmer

cette constatation expérimentale, ce qui est actuellement examiné par l'un de nos collaborateurs expérimentale à l'Université de Manchester, le Dr Ian Kinloch.

6. Il pourrait être intéressant de voir si à très basse température du brome comportement structurel et donc de transfert de charge de dopage des changements graphène si la motion tumbling peuvent être congelés en.

7. Le développement futur des méthodes approchées (telles que la mécanique moléculaire, des champs de force) qui sont peu coûteux et de calcul capable de modéliser les types π - π et d'autres des interactions faibles dans les grands systèmes, il faudra très précis des résultats de référence pour les systèmes prototypes, tels que les dimères de benzène et les interactions impliquant transferts de charge ou d'interactions dipolaires, et nous espérons que les calculs présentés ici seront utiles pour cela.

Les problèmes liés à la taille du système en faisant un tel calcul avec des chaînes de PPV et de plus SWCNTs de toute chiralité et le diamètre sera plus facile à aborder avec le code AIMPRO quand la "méthode de filtration soi-disant" est introduit. Cette méthode utilise un nombre beaucoup plus restreint de fonctions de base qui donne une description équivalente du système obtenue en utilisant notre numéro de grand courant de fonctions de base, résultant de la vitesse significative en place.

Enfin, nous nous attendons qu'une meilleure compréhension des interactions intermoléculaires faibles et comment ils peuvent être à l'écoute jouera un rôle majeur dans l'avancement de la conception rationnelle supramoléculaire.

Abstract

This thesis uses the ab initio density functional modeling programme AIMPRO to study several important examples of weak intermolecular interactions in carbon nanomaterials. At the quantum mechanical level, our calculations give a reliable and improved understanding of the role and feature of weak intermolecular interactions, which cannot be accurately predicted by conventional methods such as classical interatomic potentials.

First, the geometry and binding of bromine physisorbed on carbon nanomaterials (graphene, graphite and single walled nanotubes) is studied. In graphene, we find a new Br₂ form which is reported for the first time in this thesis, where the molecule sits perpendicular to the graphene sheet with an extremely strong molecular dipole. Bromination opens a small (86-meV) band gap and strongly dopes the graphene. In graphite Br₂ is stable parallel to the carbon layers with less charge transfer and no molecular dipole. At higher Br₂ concentrations polybromide chain structures are thermodynamically favoured, but will not occur spontaneously due to an appreciable formation barrier (27.01 kJ/mol). For single walled nanotubes Br₂ lies perpendicular to the tube surface similar to graphene, while in bundles Br₂ intercalates similar to graphite. Experimental Raman spectra are recorded to verify this result. We next study π - π stacking interactions between benzene and PPV oligomer chains with various carbon nanomaterials. For the benzene dimer we successfully reproduce high level theory stable structures, and for benzene on graphene and SWCNTs, the stacking arrangement matches AB- stacking in graphite. The orientation of the interaction between PPV/PPV is different from PPV/nanotube or PPV/graphene. In the former the molecular planes are orthogonal, similar to the crystal packing in PPV, as well as in other polyaromatic hydrocarbons. In the others the PPV plane lies (axially) parallel to the substrates, attributed to π - π stacking effects. Wavefunction analysis suggests very little electronic coupling between the PPV and SWCNTs near to the Fermi level. Predicted differences in interaction between PPV and semi-conducting or metallic tubes suggest a new route to experimental ultra-efficient composite PPV-SWCNT organic light emitting device design.

Keywords: Graphite, Graphene, Bromine, PPV, SWCNT, DFT, Raman, AIMPRO.

Table of Contents

Chapter 1 Introduction.....	1
1.1 Our method for handling weak Interactions.....	2
1.2 References	4
Chapter 2 Nanostructures, Carbon Materials and Intermolecular interactions	5
2.1 Nanotechnology.....	5
2.2 Carbon Materials	6
2.2.1 Graphite	7
2.2.2 Graphene	8
2.2.3 Carbon Nanotubes.....	9
2.3 Polymers.....	13
2.3.1 Poly-1, 4-Phenylene vinylene (PPV) Polymer.....	13
2.4 Bromine.....	15
2.5 Intermolecular Interactions.....	15
2.5.1 Weak Interactions	16
2.6 Other Types of Interactions.....	22
2.6.1 Ionic Bonds.....	22
2.6.2 Metallic bonds	22
2.6.3 Covalent bonds	23
2.6.4 Coordinative Bonds.....	23
2.6.5 Polyvalent Bonds	24
2.7 Summary	24
2.8 References	25
Chapter 3 Theory, Method and Characterization Techniques.....	27
3.1 The Schrödinger equation	27
3.2 The Many-Body Problem.....	27
3.3 General Assumptions.....	29
3.3.1 Born-Oppenheimer approximation	29
3.4 Hartree Equation.....	29
3.5 Hartree-Fock Theory.....	30
3.5.1 Møller-Plesset perturbation Theory (MP)	31
3.5.2 Configuration Interaction (CI)	31

3.5.3 Coupled Cluster Theory	32
3.6 Density Functional Theory (DFT).....	32
3.6.1 Thomas-Fermi Theory	33
3.6.2 Hohenberg and Kohn Theorem	33
3.6.3 Kohn-Sham Theory.....	36
3.7 Methods for the Treatment of $E_{xc}[n(r)]$	37
3.7.1 Local Density Approximation (LDA).....	38
3.7.2 Generalised Gradient Approximation (GGA)	40
3.7.3 The Hybrid Methods	41
3.8 Pseudopotentials.....	42
3.9 Basis Sets	43
3.9.1 Basis sets used in this work.....	44
3.10 Self-Consistency.....	45
3.11 Structural Optimisation.....	45
3.12 Vibrational Modes	46
3.13 Fermi Statistics (Level Filling).....	47
3.14 Brillouin Zone (k-point sampling).....	48
3.15 Boundary Conditions	49
3.16 Supercell Approach	50
3.17 Mulliken Population Analysis.....	51
3.18 Summary of the AIMPRO code	51
3.19 Characterization Techniques.....	52
3.19.1 Raman Spectroscopy.....	53
3.19.2 Transmission Electron Microscopy (TEM).....	56
3.20 References.....	57
Chapter 4 Bromination of Carbon Nanomaterials.....	59
4.1 Introduction.....	59
4.2 Calculation of Bromine interacting with Graphites, Graphene, SWCNTs and DWCNTs	61
4.2.1 Computational details (AIMPRO).....	61
4.3 Experimental method for the bromination of Single-Walled Carbon Nanotubes	63
4.4 Isolated Bromine Molecule.....	64
4.5 Adsorption of bromine on Graphene	66

4.6 Br ₂ perpendicular to graphene surface	70
4.7 Br ₂ parallel to graphene surface.....	71
4.8 Spectroscopy of bromine on graphene.....	72
4.9 Graphite.....	73
4.9.1 Graphite intercalation compounds.	75
4.9.2 Br ₂ Intercalated graphite.....	78
4.10 Br ₂ doped Single-walled Carbon Nanotubes (SWCNTs).....	84
4.11 Br ₂ doped double-walled nanotubes (DWCNTs)	90
4.12 Polybromide Chain structures	92
4.12.1 Polybromide Chains of Br ₂ ⁻ , Br ₃ ⁻ , Br ₄ ⁻ , Br ₄ ²⁻ and Br ₅ ⁻	94
4.12.2 Kinetic barrier for Br chain formation.....	97
4.13 Summary	100
4.14 References	101
Chapter 5 Pi-stacking vs. electrostatic interactions.....	104
5.1 What is π-π interaction?	104
5.2 Introduction	105
5.3 Computational Methods	106
5.4 Benchmarking- benzene-benzene interaction.....	108
5.5 Surface Contour Maps	116
5.5.1 Benzene-benzene interaction	116
5.5.2 Benzene-graphene interactions	118
5.5.3 Benzene-SWNT Interactions	120
5.6 Poly Para-Phenylene Vinylene (PPV) Polymer.....	123
5.6.1 Isolated PPV (3-Phenyl repeat monomer unit)	123
5.6.2 Electronic Structure of Isolated PPV Chains	124
5.6.3 PPV-PPV Interactions	127
5.6.4 PPV-graphene interaction.....	129
5.7 Non Covalent modification of Single-Walled Carbon Nanotubes (SWCNTs)	132
5.7.1 PPV/SWCNTs complex	133
5.8 Summary	142
5.9 References	144
Chapter 6 Summary, Conclusions and Future Directions.....	147

List of Publications

1- [Bromination of Graphene and Graphite'](#)

A. Yaya, C. P. Ewels, I. Suarez-Martinez, Ph. Wagner, S. Lefrant, A. Okotrub, L. Bulusheva, P. R. Briddon
Physical Review B, 83 (4), 045411 (2011)

2- [Purification of single-walled carbon nanotubes'](#)

A. Yaya, C. Ewels, Ph. Wagner, I. Suarez-Martinez, A. G. Tekley, L. R. Jensen
European Physical Journal : Applied Physics, 54, 10401 (2011)

3- [Stability of Fluorinated Double-Walled Carbon Nanotubes Produced by Different Fluorination Techniques'](#)

L. Bulusheva, Yu. Fedoseeva, A. Okotrub, I. Asanov, V. Koroteev, **A. Yaya**, C. P. Ewels, A. Chuvilin, A. Felten, G. Van Lier, D. Vyalikh
Chem. Mater. 22 (14), 4197 (2010)

4- [Graphene edge structures: Folding, scrolling, tubing, rippling and twisting'](#),

V. Ivanoskaya, Ph. Wagner, A. Zobelli, I. Suarez-Martinez, **A. Yaya**, C. P. Ewels
Book Chapter in Springer NanoCarbon Series, accepted (2011).

5. – [DFT/LDA studies on \$\pi\$ - \$\pi\$ interactions in PPV/SWCNTs and PPV/Graphene](#)

A. Yaya, C.P Ewels, F. Massuyeau, E. Faulques, J. Wery, J. –L. Duvail, et al
In Preparation (2011)

6- [DFT Studies of Polybromide chains in carbon nanomaterials”](#),

A. Yaya, I. Suarez-Martinez, G. Van Lier, A. Okotrub, L. Bulusheva, P. R. Briddon, C. P. Ewels
Prepared, to be submitted (2011)

7. – [Optical spectroscopy of brominated double-walled carbon nanotubes”](#),

L. Bulusheva, Yu. Fedoseeva, A. Okotrub, E. Flahaut, I. Asanov, V. Koroteev, **A. Yaya**, C. P. Ewels,
A. Chuvilin, D. Vyalikh
Prepared, to be submitted (2011)

8. – [Synergic effects of aligned conjugated polymer chains and SWCNTs on \(photo\)conductive properties of composite nanotubes”](#),

F. Massuyeau, **A. Yaya**, E. Faulques, C. P. Ewels, J. Wery, J. –L. Duvail, et al
Nanoletters, to be submitted (2011)

9. – [Atypical charge transfer in composites of conjugated polymer and carbon nanotubes: first-principles calculation and photophysical survey”](#),

E. Faulques, J. Wery, F. Massuyeau, J. –L. Duvail, S. Lefrant, **A. Yaya**, C. Ewels
to be submitted (2011)

List of Conferences and Poster Presentations

Posters

Low density bromination of carbon nanomaterials

1. International workshop for users of the AIMPRO DFT code, IMN, Nantes, France (2008)
2. NanoCarbons; from physicochemical and biological properties to medical and environmental effects, Naples, Italy, September (2009)
3. Ecole doctorale meeting , Anger (2009)
4. NanoteC09, Brussels, Belgium, August, (2009)

DFT study of Polybromide chains

5. 24^{ème} édition des Journées Surfaces et Interfaces, IMN, Nantes, France January (2010)
6. Chemistry of Nanotubes, Archacon, Bordeaux, France (2010)
7. Graphene international summer school, Cargese, France, October (2010)

Oral presentations

Low density bromination of carbon nanomaterials

1. AIMPRO 2010; International workshop, University of Nottingham, UK., April (2010)
2. Ecole doctorale, Nantes, France June, (2010)

DFT/LDA study of π - π stacking interactions

3. Nanofonc, Anger, France, February (2011)
4. Graphene and Nanotube workshop, Paris, France, February (2011)
5. AIMPRO 2011, International workshop, University of Strachlyde, UK., June (2011)

Prizes won

2 poster awards:

1. NanoCarbons; from physicochemical and biological properties to medical and environmental effects, Naples, Italy, September (2009)
2. 24^{ème} édition Des Journées Surfaces et Interfaces, IMN, Nantes, France January (2010)

Abbreviations and Symbols

Abbreviation	Definition
AIMPRO	Ab Initio Modelling PROgramme
BE	Binding Energy
BSSE	Basis Set Superposition Error
BHS	Bachelet, Hamann and Schluter
BZ	Brillouin Zone
CCDS(T)	Couple-Cluster Doublet Singlet (Triplet)
DFT	Density Functional Theory
DF-LMP2	Density Fitted Local Second Order
DF-SCS-LMP2	Density Fitted Spin Component Local Second Order
R ₁	Distance of Separation (center-center)
R ₂	Displacement from center
DWCNTs	Double-Walled Carbon Nanotubes
FT	Fourier Transform
GICs	Graphite Intercalation Compounds
GGA	Generalized Gradient Approximation
HF	Hartree-Fock
HGH	Hartwigsen, Geodecker and Hutter
HOMO	Highest Occupied Molecular Orbital
HOPG	Highly Oriented Pyrolytic Graphite
IDSRS	Ionization-Detected Simulation Raman Spectroscopy
LDA	Local Density Approximation
LJ	Lennard-Jones Potential
LUMO	Lowest Unoccupied Molecular Orbital
MP2	Møller-Plesset Perturbation Second Order
MWCNTs	Multi-Walled Carbon Nanotubes
NMR	Nuclear Magnetic Resonance
PD	Parallel Displaced
PS	Parallel Stack
PAH	Polyaromatic Hydrocarbon
PPV	Poly Para-Phenylene Vinylene
PSE	Pi-Stacking Effect
SEM	Scanning Electron Microscopy
SWCNTs	Single-Walled Carbon Nanotubes
T	T-Shaped
TEM	Transmission Electron Microscopy
TM	Troullier and Martins
vdW	Van der Waals

Objectives of Thesis Work

The main goal of this thesis work is to study the nature of weak intermolecular interactions in carbon nanomaterials through a combination of atomistic computer modelling and experimental optical spectroscopy. Density functional quantum chemical technique (AIMPRO modelling programme) are used to examine primarily two problems: (i) the interaction of bromine with carbon nanomaterials (graphene, graphite and carbon nanotubes), and (ii) the interaction of conjugated polymers, taking PPV as a test example with carbon nanomaterials.

Chapter 1

Introduction

The wonders and complexity of life and its environment is one of the biggest questions that has challenged and baffled mankind since the start of our existence. Our innate curiosity has led us to dissect the mechanisms and processes that make us what we are. Controlling behaviour on every scale that we study, from the macroscopic to the microscopic, the concept of molecular interaction is of critical importance. It is indeed difficult to think of something more fundamental in nanosystems than molecular interaction. Some of these interactions are very strong whilst others are weak and even reversible. The properties of the interacting molecules govern the type of forces involved and the strength and dynamics of the interaction.

The characteristics of weakly bound systems and hydrogen complexes have attracted a lot of research interest due to their importance in different fields [1-3], such as crystal packing, adsorption and reaction on surfaces and interfaces, solvation and hydrophobic or hydrophilic effects related to biological process and the mechanisms of catalyst in organic chemistry. In order to understand many of these reactions, it is crucial to establish a fundamental knowledge of how atoms and molecules interact with surfaces. Therefore, computational simulation of such complexes is perceived as an indispensable tool in providing detailed information regarding binding mechanisms and interfacial properties of interest.

Carbon nanomaterials play a unique role in nature. Actually, the formation of carbon in stars as a result of merging of three α -particles is a crucial process providing existence of relatively heavy chemical elements in the Universe. The ability of carbon atoms to form complicated networks is a fundamental fact of organic chemistry and the base for existence of life, at least, in its known forms. Even elemental carbon demonstrates unusually complicated behavior forming a number of very different structures. Apart from diamond and graphite which are very popular, recently discovered fullerenes, and nanotubes are in the focus of attention of physicists and chemists now. Thus, only three-dimensional (diamond, graphite), one-dimensional (nanotubes), and zero-dimensional (fullerenes) allotropes of

carbon have been known till recently. The two-dimensional form was conspicuously missing, resisting any attempt of its experimental observation. This elusive two-dimensional form of carbon has been named graphene, and ironically, is probably the best theoretically studied carbon allotrope. Graphene - planar, hexagonal arrangements of carbon atoms is the starting point in all calculations on graphite, carbon nanotubes and fullerenes.

The study of weakly bound systems with these carbon materials has direct implications for fundamental physical and chemical problems such as molecular spectroscopy, transition state structures, hydrogen bond selectivity, chemical reaction dynamics, and catalysis and surface interactions. But still much work to do to understand the similarities and differences in the interaction of these materials with other species such as absorbed gases and polymers.

1.1 Our method for handling weak Interactions

Although the post-Hartree Fock methods have been proven to well describe systems involving weak interaction, however, there is a real task as the systems size increases; the computational cost becomes expensive which invariably renders this method impossible for tackling larger systems [3].

Carbon nanosystems are invariably large, with many hundreds of atoms, and complex, with e.g. low symmetry, particularly when combined with polymers. Because graphene and graphite are semimetals their electronic interactions are typically long-ranged (the wavefunctions of defect states spread out a long way in the material) which means that to accurately model molecular interactions where charge transfer is involved, it is necessary to include many carbon atoms to avoid modelling molecule-molecule interaction. The flexibility of the systems (such as polymer chains) means that the potential energy surfaces under study are invariably highly complex with many local minima, which requires multiple calculations from different starting points to ensure a global minimum is identified. All of these reasons mean that to correctly model carbon nanomaterials, in interaction with other complex species such as polymers and charge transfer species, post-HF approaches are impossible, as are indeed many other techniques, and a simpler approach is required. One route to performing large calculations is with density functional techniques, in particular

using localised orbitals based on functions such as Gaussians, as implemented in the AIMPRO code. This is the approach we have used, however it is necessary to benchmark the approach against higher level theory calculations such as post-HF, which we do in Chapter 5. We show that, despite restrictions such as lack of dispersion corrections in the code, we are nonetheless able to reproduce higher level theory calculations to an acceptable degree of accuracy. We then use this approach to explore further the range of complex and fascinating interactions possible between these species, drawing out similarities and differences in interaction depending on the type of carbon nanomaterial involved.

Firstly, an overview of carbon materials and the various forms of interactions are discussed in chapter 2 with a detailed description of the AIMPRO/DFT method given in chapter 3.

The main body of this work comprises theoretical studies of four molecular systems (graphene, graphite and SWCNTs) interacting with either bromine or PPV oligomer unit and or benzene. Each study addresses important issues relating to charge transfer, stretching frequency, Raman modes, stacking interactions and preferential alignment on surfaces.

In chapter 4, the interaction of bromine physisorbed on graphene and graphite is discussed, since this has implication for the study of prototype system for weakly adsorbed nanosystems and also to verify the reliability of our modelling programme in handling such systems. Experimental Raman modes of the bromine before and after interaction with these materials and TEM images were recorded in order to verify and support the theoretical modelling results.

Also, we studied π - π stacking interaction in chapter 5. Initially, we considered the interaction of the benzene dimer, which is used as a prototypical system for studying π stacking interactions, by using this dimer, a potential energy plot for the various stacking arrangements of the dimer was obtained and compared with other potential energy curves of different theoretical methods. The interaction of PPV polymer with SWCNTs and graphene were also studied thereby giving insights into non-covalent interaction or surface functionalization. The most energetically favourable orientation of PPV interaction with benzene or graphene was obtained by a contour plot mapping.

Finally, conclusions and future directions are drawn in chapter 6.

1.2 References

- [1] P. Hobza and J. Sponer, *Chemical Review* **99**, 3247 (1999).
- [2] I. Rozas, I. Alkorta, and J. Elguero, *the Journal of Physical Chemistry A* **102**, 9925-9932 (1998).
- [3] K. Müller-Dethlefs and P. Hobza, *Chem. Inform.* **31**, (2000).

Chapter 2

Nanostructures, Carbon Materials and Intermolecular interactions

The scientific understanding of the molecular world and the application of theoretical methods laid the foundations of modern materials research.

Spontaneous formation of molecules is dependent on the design of molecular structures capable of self-assembling into supramolecular entities representing the desired architecture and functional features [1]. The application of molecular self-organization process is central for the development of novel functional nanoscale materials. Now it is well known that, the self-assembly of molecular structures is very dependent on intermolecular interactions such as electrostatic, Van der Waal forces, π - π stacking interactions, hydrogen bonding and donor-acceptor effects to give a hierarchical organization ranging from molecular level to the macroscale.

It is therefore important in all the scientific disciplines to develop knowledge of the weak non-covalent interactions types which operates between molecular structures and to learn how to use them to solve a particular need or problem.

This chapter therefore, gives brief introduction to nanotechnology and the various carbon materials studied in this thesis (graphite, graphene, PPV polymers, benzene, and SWCNTs), with also, bromine. Furthermore, the various molecular interactions types which are necessary for the understanding of these materials are described.

2.1 Nanotechnology

The continuous speed in the miniaturization of any man-made devices specifically in electronic technology have continued to impact on the technological and economical development including medical, ecological, cultural and social advances.

Nanotechnology uses the units provided by nature, which can be assembled and manipulated based on atomic interactions. Atoms, molecules and solids, are therefore the building blocks of nanotechnology. Being the key driving force in the emerging field of nanotechnology, the limits of further miniaturization as established by the top-down fabrication procedures are

nearing their end, and research and engineering has vigorously drifted into the potential of bottom-up methodologies starting at the atomic or molecular level to design nano-objects of defined shapes and dimensions [2], as already envisioned by Richard Feynman in his talk “there is plenty of room at the bottom” [3].

Over the last half century, the field of computational materials modelling has matured while the understanding of nanoscience has made tremendous progress. The merging of both disciplines represents the most promising approach to design distinct shape-persistent nano-objects via self assembly, creating long-range patterns through intermolecular forces at interfaces.

This therefore, leaves no doubt in the discovery of new materials, processes, and phenomena at the nanoscale, as well as new experimental and theoretical techniques by a way of providing opportunity for the development of innovative nanosystems. Research in nanotechnology promises breakthrough in areas such as materials engineering and manufacturing, nanoelectronics, medicine and healthcare, energy and information technology.

2.2 Carbon Materials

Carbon is a very versatile material which exists in nature in different allotropic forms and the third most abundant element in the universe after hydrogen and helium. On the periodic table, it is classified in group IV together with silicon, germanium, tin and lead. Most of these elements exist in tetrahedral (sp^3) bonding with their neighboring atoms. While Tin is also known to have the largest allotropic forms, carbon is the only member of this group that can also take all different hybridised configurations such as a plane hexagonal (sp^2) or a linear (sp) configuration depending on the atom or compound it is bonded to.

The extraordinary properties of carbon nanomaterials could be traced from the hybridization of carbon; electrons in the innermost shell of carbon atoms make up an electron ‘core’ adequately enclosed to allow the outer electrons to mix with other atoms to form linear or one-dimensional (1D), plane or two-dimensional (2D) and tetrahedral or three-dimensional (3D) materials (see Figure 1).

Various forms of carbon materials are found in nature and the discussion here will be limited to the materials studied in this thesis and readers who require a deep understanding of this wonderful element are referred to consult many of the physical chemistry literature text available elsewhere.

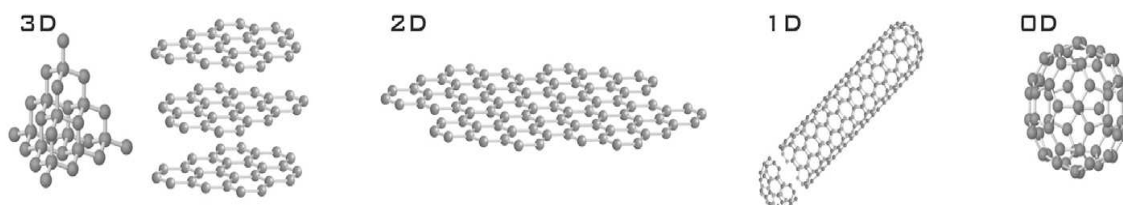


Figure 1. Crystal structures of the different allotropes of carbon. (Left to right) Three-dimensional diamond and graphite (3D); two-dimensional graphene (2D); one dimensional nanotubes (1D); and zero-dimensional buckyballs (0D) (Reproduced from ref. [4]).

2.2.1 Graphite

Graphite has a layered structure in which the atoms are arranged in a hexagonal pattern within each layer and the layers are stacked in an AB sequence. This results in a hexagonal unit cell with dimensions ($a = 2.46 \text{ \AA}$, $c = 6.71 \text{ \AA}$) [5-7]. It was Bernal who first proposed the hexagonal structure of graphite in 1924 [8] (see Figure 2).

The unique properties of graphite result from two different types of bonds in the structures, as a result of sp^2 σ and π bonding as compared to the sp^3 hybridization consisting only of σ bonds that is mostly associated with diamond crystals [7]. It is accepted that the kind of bonding that exists between the intra-layers of graphene sheets are covalent, which obviously applies to graphite, however, the inter-layer interactions have been a subject of debate amongst the science fraternity with some authors suggesting a van der Waals sort of interaction between the layers and some others, instead prefer to call it a weak intermolecular interaction [6]. The graphene planes are separated by a distance of 3.35 \AA .

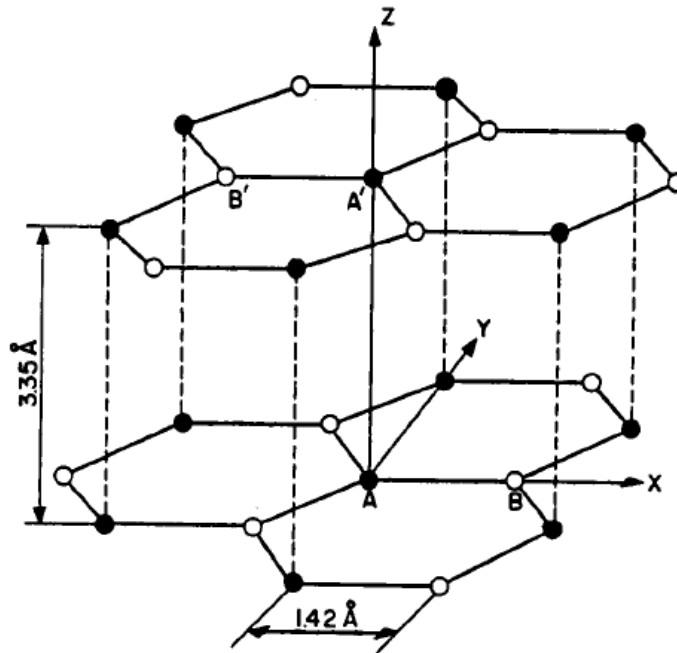


Figure 2. Crystal structure of graphite (taken from reference [5]). The primitive unit cell is hexagonal with dimensions ($a = 2.46 \text{ \AA}$ and $c = 6.71 \text{ \AA}$). The in-plane bond length is 1.42 \AA . There are four atoms per unit cells labeled as A and B

Because of the weak interplanar interactions, the carbon layers can slide over each other making it useful as a lubricant or in pencils and also are used as moderators in nuclear reactors [9].

2.2.2 Graphene

The term graphene was first used in 1987 [10] to describe single layers of graphite. Then in 2004, a layer of graphene was pulled out from graphite and deposited on a silicon substrate [11] see Figure 3.

According to the Mermin–Wagner theorem [12], “long-wavelength fluctuations destroy the long-range order of 2D crystals”. These fluctuations can, however, be suppressed by anharmonic coupling between bending and stretching modes or the presence of a substrate, meaning that a 2D membrane can exist but will exhibit strong height fluctuations [13].

It has been demonstrated that these ultra thin graphite pieces are only one atom thick and that there is a peculiar behaviour of the charge carriers in these ultra thin sheets which has resulted into worldwide research in this material.

In graphene, electrons move with such an ease and possess a vanishing mass and have an intrinsic degree of freedom known as helicity [14].

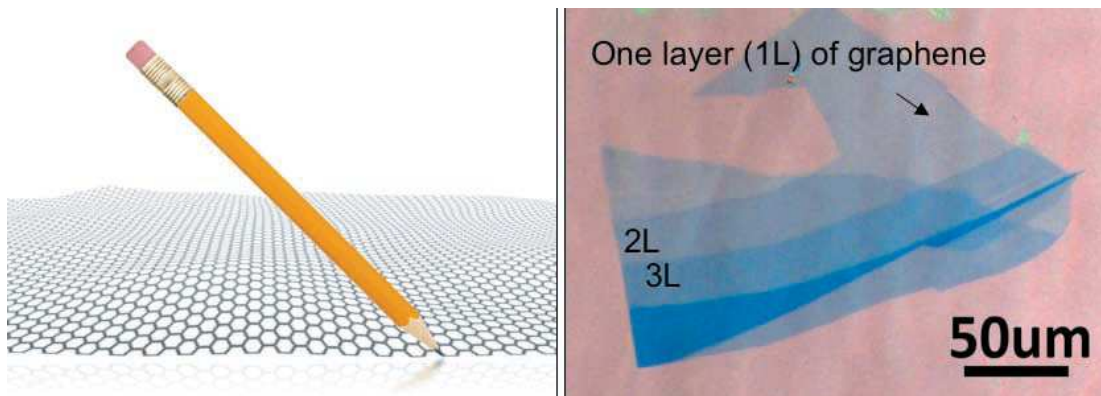


Figure 3. (Left) technique for making graphene by a pencil leaving a trace of graphite on a paper. (Right) optical picture of a few layer graphene flakes. (Taken from ref.[14])

Due to easy manufacturing procedure and affordance of this material, it is envisioned for many potential applications covering a wide range of fields such as, graphene field effect transistor in gigahertz (microchip) and terahertz range which is ideal for the identification of hidden weapons, bio-sensors, touch screens and solar cell application. Also, the mechanical properties of graphene have opened up many exciting studies in composites and force sensing and detection.

2.2.3 Carbon Nanotubes

The landmark paper by Iijima and Ichihashi in 1993 [15] showing single-walled carbon nanotubes (SWCNTs) marked a new beginning for a wide range of research in the field of nanotechnology due to their potential for various applications such as electronic devices, nanocomposites, supercapacitors [16,17] and secondary batteries [18,19].

Carbon nanotubes occur in two different forms, single-walled carbon nanotubes (SWCNT), which are composed of a graphene sheet rolled into a cylinder (see Figure 4) and multi-walled carbon nanotubes (MWCNT), which consist of multiple concentric graphene cylinders. For the SWCNTs, depending on the chiral angle, η , and the chiral vector, L , of the graphene, different chirality could result (armchair, zigzag and chiral, this is shown in Figure 5).

Compared to multi-walled nanotubes, single-walled nanotubes are expensive and difficult to obtain and clean, but they are of great interest owing to their expected novel electronic, mechanical, and gas adsorption properties [20].

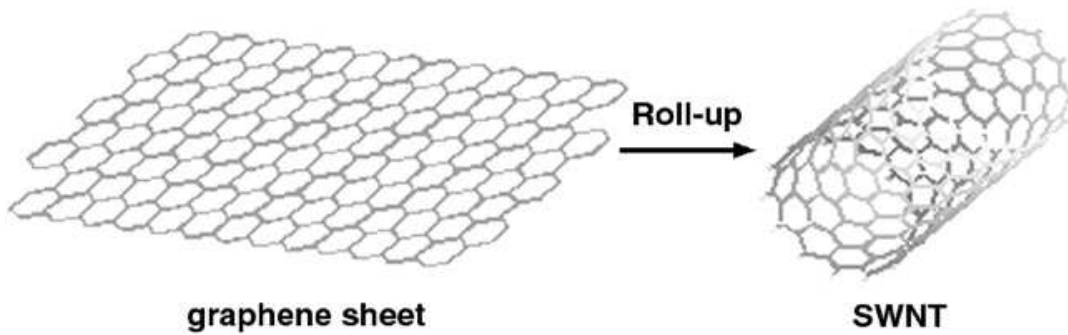


Figure 4. Scheme for creating a single wall carbon nanotube by rolling-up graphene sheet (Adapted from ref. [21])

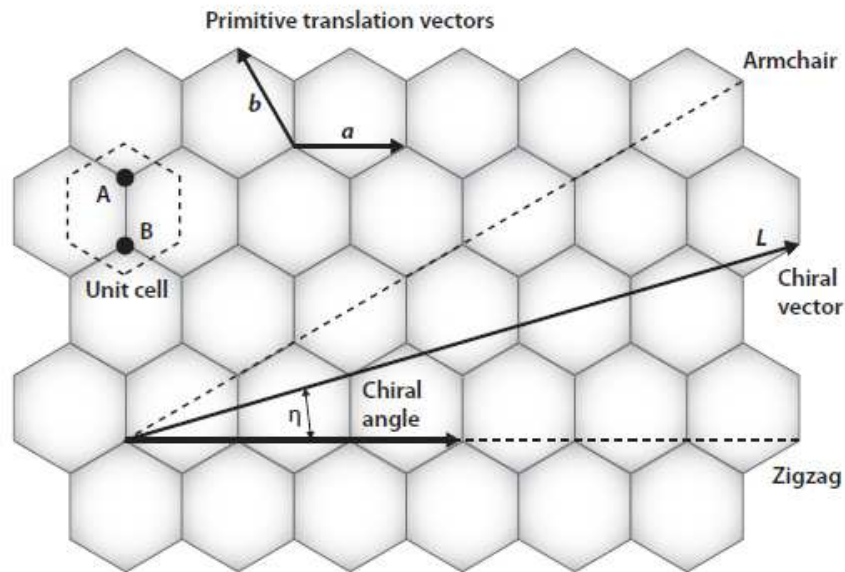


Figure 5. Honeycomb lattice of graphene with hexagonal unit cell (A and B). The chiral vector determining the structure of a carbon nanotube is given by L , and its length gives the circumference. The chiral angle is denoted by η , when $\eta=0$, corresponding to zigzag nanotube and $\eta= \pi/6$, to armchair nanotubes (Taken from ref. [22]).

The common production methods for these versatile materials are by chemical vapour deposition, arc-discharge and laser vaporization, in the presence of a metal catalyst [23].

However, large-scale production of carbon nanotubes with controlled conformation still remains challenging. In the past few years, chemical vapour deposition (CVD) has been used as a promising solution. The process is simpler and has a higher productivity than the arc-discharge process. Nonetheless, the carbon nanotubes produced by the catalytic process are usually thicker than those produced by the arc-discharge process and often consist of large aggregates.

Carbon nanotube based materials have inspired scientists due to a wide range of potential applications. The use of carbon nanotubes in polymer/carbon nanotube composites has attracted wide attention. The carbon nanotubes have unique atomic structure, very high aspect ratio, and extraordinary mechanical properties (strength and flexibility). These properties make them ideal reinforcing fibers in nanocomposites.

However, colloidal materials such as carbon nanotubes do not spontaneously suspend in polymers, thus the chemistry and physics of filler dispersion becomes a major issue. In the case of polymers filled with carbon nanotubes, the research challenge is particularly tremendous due to the unique character of these unusual materials. As a result of strong Van der Waal attraction, nanotubes aggregate to form bundles or “rope” (shown in Figure 6) that are very difficult to disperse [24]. In case of single nanotubes, they are only 1-3 nm in diameter, however, since they like to assemble into ropes which consist of many nanotubes, are most likely 10-200 nm in diameter. Furthermore, ropes are tangled with one another like spaghetti or polymers. With high shear, these ropes can be untangled, but it is extremely difficult to further disperse at the single tube level.

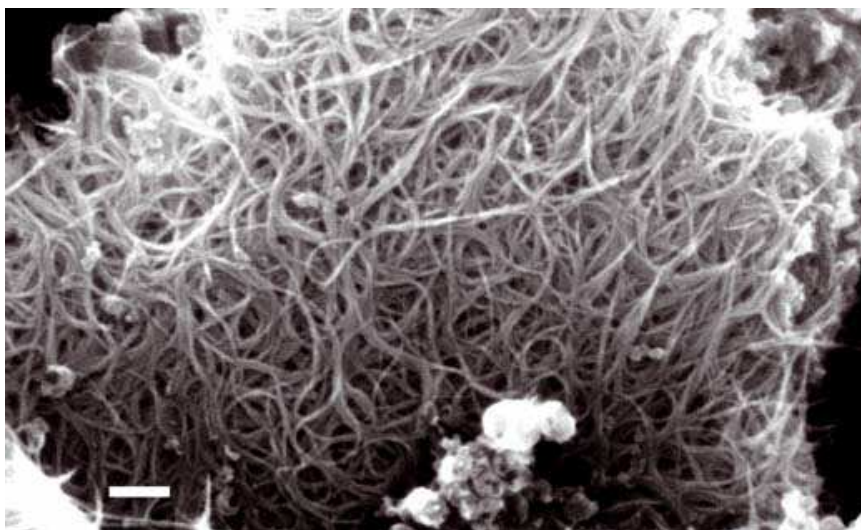


Figure 6. SEM image of single-walled carbon nanotubes showing the rope-like structure [23].

Methods such as covalent and non-covalent functionalization together with sonication have been used to disperse these nanotubes with some success.

As a result of low entropy of mixing, rigid molecules of high molecular weight require strong repulsive interactions to disperse. Since the connectivity and rigidity of macromolecules drastically reduces the number of configurations available in the dispersed state, mixing becomes a problem.

2.3 Polymers

Polymers are long chain molecules that are made up of repeating units (monomers) which form the building block of larger molecules (oligomers). Our modern world is built on polymers (clothes, pipes, wires, coatings, plastics etc). Indeed even the proteins in our body are polymers of amino acid compounds; this then makes life itself a form of polymer with a countless variety of shapes and forms.

Polymers are composed of a backbone of carbon atoms in chains and are result of the catenation property of elemental carbon. They exhibit special mechanical, rheological, electronic and optical properties due to their long chain structure. The properties of polymers are functions of their chemical composition, and also, there is a dependence upon the length of the molecules and physical conditions such as temperature and solvent.

Polymers can be classified into two groups which are based on their backbone stiffness; flexible chain polymers include those polymers that contain aliphatic portions in their backbone and stiff polymers are comprised of molecules having both aromatic and conjugated chemical groups in their backbone which are often called conjugated polymers. For the stiff polymers with high level of unsaturation along the backbone, they tend to be electrically conducting in nature and they also show very interesting crystalline structures and strong intermolecular interaction. They are used in organic photovoltaic devices and flat panel displays. One such polymer that has generated a lot of research interest due to its electroluminescence properties is poly-paraphenylene vinylene (PPV).

This is the polymer used in this thesis work and described below.

2.3.1 Poly-1, 4-Phenylene vinylene (PPV) Polymer

PPV is an organic semi-conducting polymer. Interest in these types of polymers for electroluminescence was triggered by the works of Tang et al [25,26], in which they showed that devices with a sublimed molecular dye film in combination with one or two organic charge transport layers resulted in conversion efficiencies of charge carriers into photons by ~1 %.

The use of PPV in light emitting diode (LED) applications followed the first report by Burroughes et al in 1990 [27]. After this report, a large variety of semi-conducting polymers were used as active electroluminescence layers in LEDs, with a wavelength of light emission centered in different regions of the visible spectrum. Two other examples of conjugated polymers beside PPV are given in Figure 7.

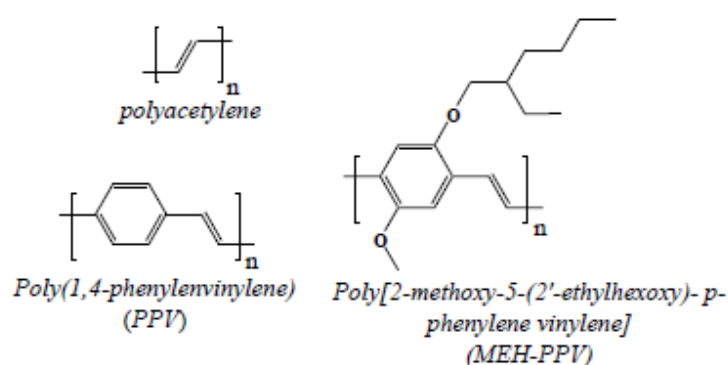


Figure 7. Some structures of organic conjugated polymers [28]

PPV can be solution processed only by the precursor route, the major obstacle in this step is the requirement for thermal conversion which is in excess of 300°C. The breakthrough came with the discovery of soluble PPV derivatives [29], which enable the realization of robust, flexible electronic devices that can be easily processed by solution techniques like spin-coating or ink-jet printing, see Figure 8.



Figure 8. Some flat screen television made from OLEDs by Samsung Limited.

2.4 Bromine

Pure bromine is a diatomic molecule, Br_2 , and is the only non-metallic element that is liquid at room temperature. Bromine is less reactive than chlorine or fluorine but more reactive than iodine. It forms compounds with many elements and like chlorine is used as a bleaching agent. It is also used as a fire retardant in plastics, dyestuffs and as a water purification compounds.

2.5 Intermolecular Interactions

Properties of materials are controlled by the density of bonds, their spatial distribution and bond strength between the particles. Therefore, the understanding of intermolecular interactions in structures is crucial in the understanding of the relationship between (structure-property-function).

As size and system dimension decreases towards the nanoscale, the behaviour and characters of isolated molecules becomes increasingly important. Ultimately, individual molecules (which show thermal and structural fluctuations) will dominate the behaviour of nano-systems. Generally, the interactions between atoms, group of atoms, ions and molecules can

vary enormously with respect to their character and strength. In order to differentiate this, the various types of interactions are divided into classes known as bond types and these classes are suited for the description of a bond.

On the contrary, in classical synthetic chemistry where strong bonds, such as covalent bonds are important, however, in nanomaterials, the weak and medium non-covalent bonds become increasingly important. The significance of these weak bonds increases with an increasing size of the aggregates constructed, which is also comparable to what happens in nature. Hence, this section will build on the key classes of chemical bonds and further discuss their importance to nanomaterials or nanosystems (see Figure 9).

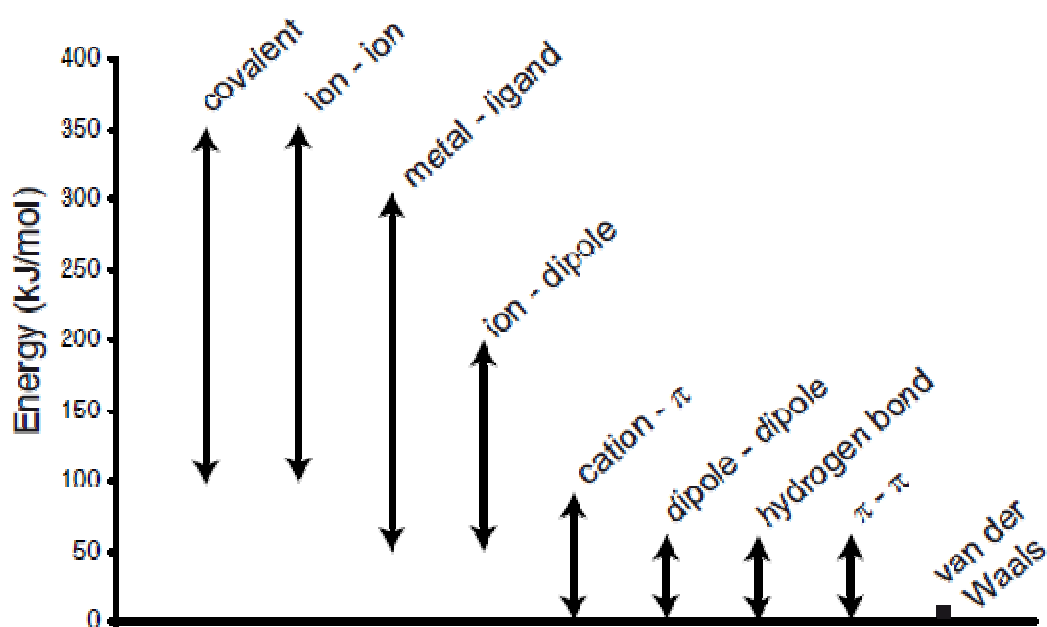


Figure 9. Energies of covalent and non-covalent interactions (taken from ref. [30]).

2.5.1 Weak Interactions

2.5.1.1 Van der Waals Interactions (vdW)

The Van der Waals' [31] interaction occurs universally between closely spaced atoms, but becomes important only when the conditions for stronger bonding mechanisms fail.

Van der Waals bond is a basic type of bond, which becomes important due to the cooperative effect of many atoms bound to each other. The mobility of molecules is determined by the size. Another parameter is the partial dissociation of Van der Waals bonds by intramolecular movements. If atoms or groups of atoms are only connected by freely rotating bonds, the rotation of one part of the molecule can thus induce the separation of the respective bond. With fixed bonds, all bonds are distributed in a cooperative manner. At room temperature the bonds between individual atoms can be thermally activated and broken.

As atoms approach each other, the electrons of one atom dynamically disrupt the distribution of the electrons of the other atom. This deformation perturbs the charge distribution in some way such that the sum of the energy of the two approaching atoms is lowered as compared to the isolated atoms. This difference in energy determines the strength of the bond and if this effect is not influenced by other bonds (example by the exchange of electrons); the bond energy is fairly low.

Dispersion force which act between all atoms and molecules, makes up the major contribution to Van der Waals forces as compared to the others (such as repulsive, electrostatic and induction-polarization forces). Detailed information on Van der Waals interactions between different types of atoms and molecules are given in [32,33].

It was London [34], who theoretically explained what actually happens in the so called Van der Waals atoms or molecules by observing that, a neutral atom has zero permanent electric dipole moment, the same as many molecules; yet such atoms and molecules are attracted to each other by electrical forces. He showed that the zero-point motion, which is a result of the Heisenberg uncertainty principle, gives any neutral atom a fluctuating dipole moment whose amplitude and orientation varies rapidly. Hence the field induced by a dipole falls off as the cube of the distance. Thus if the nuclei of two atoms are separated by a distance r , the instantaneous dipole of each atom creates an instantaneous field proportional to $(1/r)^3$ at the other. Potential energy of the coupling between dipoles which is attractive is given by an equation of the form;

$$E_{\text{attr}} = - (A/r^6) \quad (1)$$

However, as the interatomic separation decreases, the attractive tendency begins to be offset by repulsive mechanisms when the electron clouds of atoms begin to overlap. The attractive energy of the Van der Waals dispersion for neutral, non-polar systems with spherical symmetry is rigorously derivable quantum-mechanically. And one of the most famous empirical parameters commonly used to describe Van der Waals interactions energy is the Lennard-Jones potential;

$$\phi(r) = -\frac{A}{r^6} + \frac{C}{r^{12}} = 4\epsilon \left[\left(\frac{\sigma}{r}\right)^{12} - \left(\frac{\sigma}{r}\right)^6 \right] \quad (2)$$

where ϵ , well depth, r , distance and σ , distance for which the potential energy vanishes, the Hamaker constant, $A = \pi^2 C P_1 P_2$; P_1 & P_2 are number of atoms per unit volume in two interacting systems and C , the attractive interaction strength.

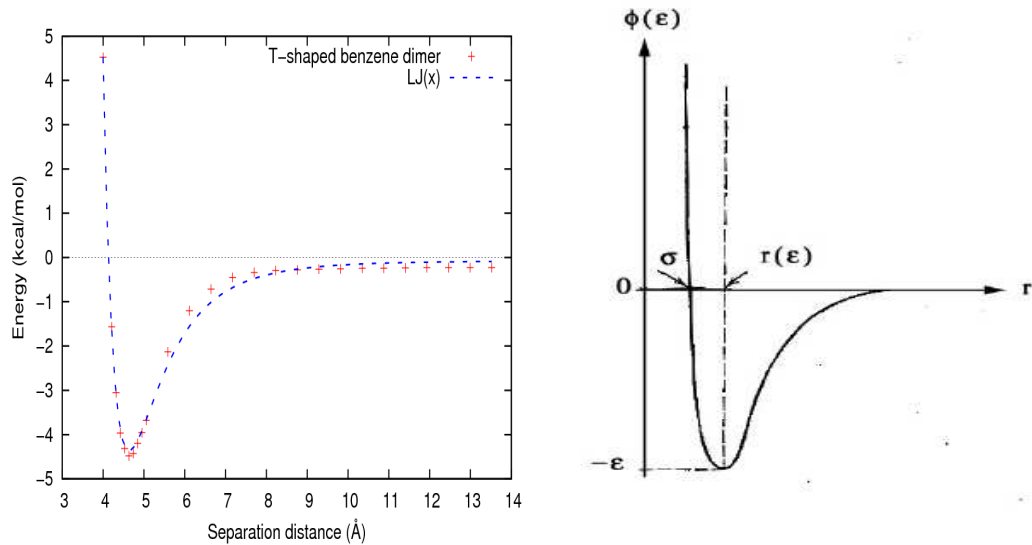


Figure 10. (Left) Our binding energy curve with the trend of its attractive and repulsive components for the benzene dimer in T-shape conformation (red) with the analytical Lennard-Jones fit (blue) and (Right) Lennard-Jones potential between two atoms or non-polar molecules indicating the empirical parameters (adapted from ref. [33]).

These Van der Waals interactions play an important role in all phenomena involving intermolecular forces. While belonging to weak bonds, they are always present [32]. They are also important for life in living cells especially in the creation of 3D structures of proteins. They also form an important component in drug designs for the attachment of other moieties to target specific cells in the body. And in the arrangement of complex molecular aggregates from smaller units which is the basis for supramolecular chemistry.

2.5.1.2 π - π Interactions (Aromatic interactions)

These are direct interactions involving aromatic rings with energies between (0-50 kcal/mol). The attachment of substituent groups is important, as the interactions depend on electron-rich or electron-deficient aromatic rings.

There are three major arrangements for π - π stacking [35-37]; parallel-displaced, face-to-face and edge-on-face conformations, (see Figure 11). The edge-on-face and the parallel-displaced are the most energetically stable structures which have been reported by theory and experiments. The aromatic units attract each other when the interactions of the π system of one arene with the σ system of the other and also when the π - π units of each arene are slightly out of plane, these together gives energies of binding which are higher than when the π - π units of the each arene molecule is face-face, which result in higher repulsion between the two molecules.

The π - π interactions have been shown to be the major contributors to the stability of the double helix structure of DNA, intercalation of drugs in to DNA, protein folding (porphyrin aggregation) and the crystal packing of aromatic units.

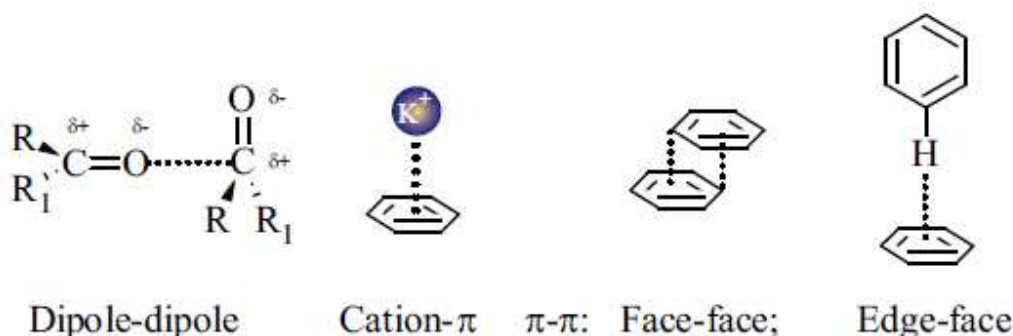


Figure 11. Schematic showing some weak interaction types [38]

2.5.1.3 Hydrogen Bonding

The hydrogen bond is an attraction interaction in which an electropositive H atom, intercedes between two electronegative species (such as oxygen or nitrogen) and brings them closer together [39]. Hydrogen bonding spans between many vital interactions in chemical, physical and biological science, with interesting features such as stability, directionality and dynamic nature [40].

The nature of hydrogen bond depends on the directional strength of the intermolecular interactions and hence, is selective and directional [41]. Generally, an individual hydrogen bond is of relatively low energy, distributing only a weak contribution to the overall energy. Also, it is easily cleaved. However, several hydrogen bonds between two molecules can stabilize the created aggregate significantly by inducing a cooperative binding.

Therefore, the selective nature and directionality of the hydrogen bond has made it an extensive component in the construction and stabilization of large non-covalent bonded molecular and supramolecular structures.

They can also be formed, when a donor (D) with an available acidic hydrogen atom is brought into contact with an acceptor (A), (as illustrated in Figure 12).

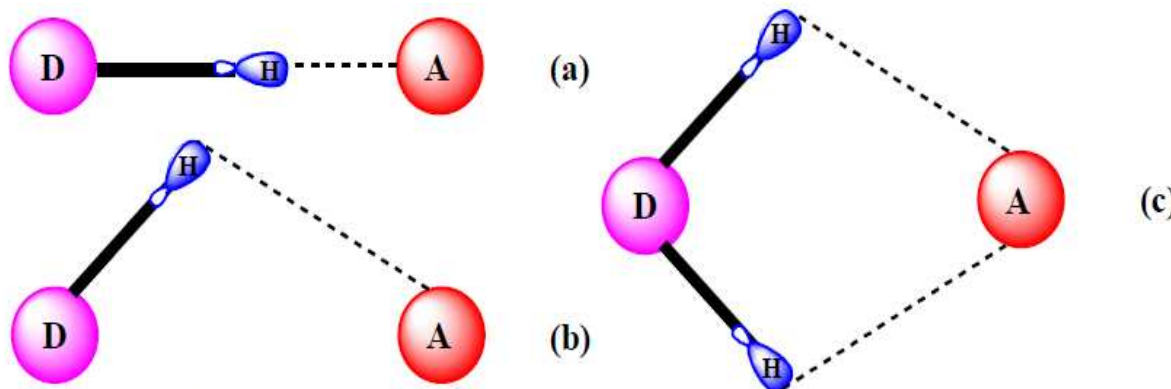


Figure 12. Schematic representation of hydrogen bonds with (a) linear, (b) non-linear, (c) bifurcated hydrogen bonds (adapted from ref. [42])

Three different types of hydrogen bonds are shown based on their structural characteristics (Figure 12). Most of the hydrogen bonds are not linear as they deviate from the 180° bond

angle and are classed as non-linear types (Figure 12b). When an acceptor takes on two hydrogen atoms, the result is a bifurcated hydrogen bond (Figure 12c). Strong hydrogen bond is characterized by D.....H distance of less than 2.5 Å with a linear structure [40], (Figure 12a).

For strong, moderate and weak bonds, the hydrogen bond energy can range from 15-40 kcal/mol, 4-15 kcal/mol and 1-4 kcal/mol respectively. This therefore gives an indication for wider range of interaction energies in hydrogen bonds than for ionic or covalent bonds but however, are still weaker bonds as compared to covalent or ionic bonds.

2.5.1.4 Dipole-Dipole interactions

Due to the differences in electronegativities, molecules made up of different atoms normally exhibit inhomogeneous electron distributions. But when the bonds are symmetrical, this distribution will not be apparent in the environment. Otherwise an electron polarity of the molecule is observed. Such molecules with one or more dipole moment attract each other (see Figure 11). The intensity of the polarity determines the strength of the dipole-dipole interactions.

These can also be observed for instance, when only one half exhibit permanent dipole moments. As the electron shells can be deformed by external fields, a molecule with a permanent dipole moment is able to induce a deformation which therefore results in polarization with a dipole moment which is termed an induced dipole.

Dipole-dipole interactions are ubiquitous in nature and for example can be responsible for deposition and binding on surfaces.

2.5.1.5 Cation- π Interactions

These are electrostatic interactions occurring between a positively charge species and the planes of a system containing π electrons (0-80 kcal/mol), see Figure 11. The interactions of alkali and alkaline earth metals to π systems are weak and considered as supramolecular, but however, the taxonomic classification of transition metals binding to conjugated polymers

has still not come to a final conclusion [43]. The cation- π interactions are not limited to metals; it has been shown that, ammonium and complex organic cations are good π binders. These interactions are seen as equally important as the hydrogen bonds, hydrophobic effects and ion pairing in defining the structures of protein aggregates [44].

2.6 Other Types of Interactions

2.6.1 Ionic Bonds

When there is a large difference in electronegativities of atoms, there is a transfer of one or more electrons from the electropositive to the electronegative interacting partner. The bond formed is not determined by the binding electrons, but by the interaction of ions generated by the transfer of electrons.

The strength of this bond is comparable to covalent bond, implying that, it is a strong chemical bond.

2.6.2 Metallic bonds

This is the electrostatic attractive forces between the delocalized electrons known as conduction electrons and the positively charged metal ions.

Metal have loosely moving electrons. Since the valence electrons move freely, metals can be considered to have positively charged ions instead of neutral atoms. The attraction between the positively charge ions and the loosely moving electrons binds the atoms in metals.

The metallic bonding has attracted interest in micro and nanotechnology due to potential applications of metals and semiconductors in electrical or electronics materials. Also, metallic bond helps in the adhesion and both electrical and thermal conductivity at interfaces occurring between metals and inside alloys [45].

2.6.3 Covalent bonds

This is the strongest of all the bonds. Strong bonding occurs during an interaction between two atoms with unpaired electrons which result in doubly-occupied binding orbitals. While the density distribution of electrons does not differ significantly from the density distribution of the free atoms, the differences in the electronegativity of the binding atoms give rise to polarity of covalent bonds.

An atom is limited by the number of covalent bonds it can make (which is dependent on how much the number of outer electrons differs from a closed-shell configuration), and there is a marked directionality in the bonding [46]. Furthermore, the geometry of the bonds around an atom is influenced by its valence. Bivalent atoms give linear or bent structures and trivalent atoms result in trigonal-planar or trigonal-pyramidal geometries. Regular geometries around atoms with four valence are planar square or tetragonal. Hence covalent bonds can affect just several or high number of atoms. The hydrogen molecule, H_2 , is a simple example of covalent bond.

Consequently, the creation of molecular nanostructures is dependent on the degrees of individual bonds on one hand, and the rigidity of certain parts of molecules on the other hand. Therefore, double bonds, bridged structures and multiple rings system of covalent units are important motifs for molecular architecture and molecular nanotechnology.

2.6.4 Coordinative Bonds

These bonds are generated by the provision of an electron pair by one of the binding partners (ligands) for a binding interaction. One of the requirements for this type of bond is the existence of double unoccupied orbital at the other binding partner, in order to create a doubly occupied binding orbital [47].

The stability of coordinative bonds lies between the strengths of the weaker dipole-dipole interactions and that of covalent bonds. Hence, coordinative bond is well suited for the realization of adjustable binding strengths and lifetimes of molecules. This type of bond can be found in nature which uses the principle of finely tuneable binding strengths of complex bonds; example is the Co- or the Fe-complexes of the heme groups of enzymes [48].

2.6.5 Polyvalent Bonds

Polyvalent or multivalent bonds are the simultaneous association of multiple ligands on one entity (a surface or a molecule) to multiple receptors on another entity [49].

Multivalent interactions are dominant in biology (e.g. in infectious diseases, in processes involving antibodies, metastasis, platelet activation, inflammation, and in many conditions in which cells interact with surfaces) [48,49]. Multiple simultaneous interactions have unique collective properties that are qualitatively different from the properties of their monovalent constituents [49,50]

The mobility of molecular groups determines the size of cooperative effective sections in large molecules which are able to bind externally in a polyvalent manner. This is well known from the melting behaviour of double-stranded DNA. The thermally induced separation of the two strands connected by hydrogen bonds requires rupturing the bridges. Over a length of about 40 bases, the melting temperature does not increase further, pointing to an independent movement of strand sections above a critical length [48].

Confirming, understanding, and quantifying the importance of multivalency in biological interactions, and moving this fundamental knowledge towards applications in the design of drugs and materials will be important in the preparation of dynamic or self-repairing materials for application in medicine, materials science and nanotechnology

2.7 Summary

The importance of nanotechnology has been highlighted with a brief account on nanostructures. Also, carbon which forms the basis of most important material in the field of nano-science has been elaborated. The understanding of physical interactions on the nanoscale and interfacial properties allow structural and functional investigation on a single molecular level.

Together with experimental concept on interfacial properties, theoretical calculations will generate new insight into the nature of molecular interactions and their relation to structures and functions.

2.8 References

- [1] C. J. Kuehl, *Chem. Eur. Journ.* **5**, 102 (1999).
- [2] S. Hecht and I. Huc, *Foldamers: Structure, Properties, and Applications* (Wiley-VCH, 2007).
- [3] R. P. Feynman and C. Sykes, *No Ordinary Genius: The Illustrated Richard Feynman* (Norton, 1996).
- [4] M. I. Katsnelson, *Materials Today* **10**, 20-27 (January).
- [5] D. D. L. Chung, *Journal of Materials Science* **37**, 1475–1489 (2002).
- [6] R. Telling and M. Heggie, *Philosophical Magazine Letters* **83**, 411-421 (2003).
- [7] J.-C. Charlier, X. Gonze, and J.-P. Michenaud, *Europhys. Lett.* **28**, 403-408 (1994).
- [8] J. D. Bernal, *Proceedings of the Royal Society of London. Series A, Containing Papers of a Mathematical and Physical Character* **106**, 749-773 (1924).
- [9] C. P. Ewels, R. H. Telling, A. A. El-Barbary, M. I. Heggie, and P. R. Briddon, *Phys. Rev. Lett.* **91**, 025505 (2003).
- [10] S. Mouras, A. Hamma, D. Djurado, and J.-C. Cousseins, *Revue De Chimie* **24**, 574-582 (1987).
- [11] K. S. Novoselov, A. K. Geim, S. V. Morozov, D. Jiang, Y. Zhang, S. V. Dubonos, I. V. Grigorieva, and A. A. Firsov, *Science* **306**, 666 -669 (2004).
- [12] N. D. Mermin, *Phys. Rev.* **176**, 250 (1968).
- [13] A. Fasolino, J. H. Los, and M. I. Katsnelson, *Nat Mater* **6**, 858-861 (2007).
- [14] B. Özyilmaz, *Innovation* **9**, 31-33 (2010).
- [15] S. Iijima and T. Ichihashi, *Nature* **363**, 603-605 (1993).
- [16] L. Diederich, E. Barborini, P. Piseri, A. Podestà, P. Milani, A. Schneuwly, and R. Gally, *Appl. Phys. Lett.* **75**, 2662 (1999).
- [17] C. Niu, E. K. Sichel, R. Hoch, D. Moy, and H. Tennent, *Appl. Phys. Lett.* **70**, 1480 (1997).
- [18] E. Frackowiak, K. Metenier, V. Bertagna, and F. Beguin, *Appl. Phys. Lett.* **77**, 2421 (2000).
- [19] G. T. Wu, C. S. Wang, X. B. Zhang, H. S. Yang, Z. F. Qi, P. M. He, and W. Z. Li, *Journal-electrochemical Society* **146**, 1696–1701 (1999).
- [20] T. W. Ebbesen, *Carbon Nanotubes: Preparation and Properties* (CRC Press, 1997).
- [21] A. Yaya and T. G. Abraham, *Processing and Characterization of Single-walled Nanotube Polymer Composite*, Master Thesis, Aalborg University, 2008.
- [22] T. Ando, *NPG Asia Mater* **1**, 17-21 (2009).
- [23] A. Yaya, C. P. Ewels, P. Wagner, I. Suarez-Martinez, A. Gebramariam Tekley, and L. Rosgaard Jensen, *Eur. Phys. J. Appl. Phys.* **54**, 10401 (2011).
- [24] C. Bower, A. Kleinhammes, Y. Wu, and O. Zhou, *Chemical Physics Letters* **288**, 481-486 (1998).
- [25] C. W. Tang and S. A. VanSlyke, *Appl. Phys. Lett.* **51**, 913 (1987).
- [26] C. Adachi, T. Tsutsui, and S. Saito, *Appl. Phys. Lett.* **55**, 1489 (1989).
- [27] J. H. Burroughes, D. D. C. Bradley, A. R. Brown, R. N. Marks, K. Mackay, R. H. Friend, P. L. Burns, and A. B. Holmes, *Nature* **347**, 539-541 (1990).
- [28] O. Mirzov and I. G. Scheblykin, *Phys. Chem. Chem. Phys.* **8**, 5569 (2006).

- [29] A. Kraft, A. C. Grimsdale, and A. B. Holmes, *Angewandte Chemie International Edition* **37**, 402-428 (1998).
- [30] D. I. Khomskii, *Basic Aspect of Quantum Theory of Solids* (Cambridge University Press, New York, USA, 2010).
- [31] J. D. van der Waals, in *Over De Continuïteit Van Den Gas- En Vloeistof Toestand* (Leiden, Netherlands, 1873).
- [32] J. Israelachvili and H. Wennerstrom, *Nature* **379**, 219-225 (1996).
- [33] D. Myers, in *Surfaces, Interfaces, and Colloids* (John Wiley & Sons, Inc., 2002), pp. 489-493.
- [34] F. London, *Zeitschrift Für Physik* **63**, 245 (1930).
- [35] S. Grimme, *Angew. Chem. Int. Ed. Engl* **47**, 3430-3434 (2008).
- [36] C. A. Hunter, J. Singh, and J. M. Thornton, *J. Mol. Biol* **218**, 837-846 (1991).
- [37] M. O. Sinnokrot, E. F. Valeev, and C. D. Sherrill, *Journal of the American Chemical Society* **124**, 10887-10893 (2002).
- [38] I. Fleming, *Molecular Orbitals and Organic Chemical Reactions* (John Wiley & Sons, Inc., United Kingdom, 2010).
- [39] G. R. Desiraju, *Angewandte Chemie International Edition* **50**, 52-59 (2011).
- [40] G. A. Jeffrey, *An Introduction to Hydrogen Bonding* (Oxford University Press, New York, 1997).
- [41] M. C. Etter, *Accounts of Chemical Research* **23**, 120-126 (1990).
- [42] S. Scheiner, *Hydrogen Bonding: A Theoretical Perspective by Steve Scheiner* (Oxford University Press, New York, 1997).
- [43] J. C. Ma and D. A. Dougherty, *Chemical Review* **97**, 1303-1324 (1997).
- [44] J. P. Gallivan and D. A. Dougherty, *Proc. Natl. Acad. Sci. U.S.A* **96**, 9459-9464 (1999).
- [45] M. Rosoff, *Nano-surface Chemistry* (Marcel Dekker, 2001).
- [46] B. Bhushan, *Springer Handbook of Nanotechnology* (Springer, 2004).
- [47] J. D. Dunitz, in *Coordinative Interactions* (Springer, Berlin, 1973).
- [48] L. Stryer, *Biochemistry*, 4th ed. (Freeman, New York, 1995).
- [49] M. Mammen, S. K. Choi, and G. M. Whitesides, *Angewandte Chemie-International Edition* **37**, 2755- 2794. (1998).
- [50] R. W. Siegel and G. J. Thomas, *Ultramicroscopy* **40**, 376-384 (1992).

Chapter 3

Theory, Method and Characterization Techniques

The aim of this chapter is to outline the theoretical approaches used in solving the many-body electronic structure problem for a system of interacting particles as well as giving some basics on the experimental instruments used (Raman spectroscopy and Transmission electron microscopy). This begins with the quantum mechanical challenge set by the many-body Schrödinger equation, followed by the main approximations used in solving this equation. Other techniques used in the literature are then discussed such as the Hartree and Hartree-Fock methods. Finally, the discussion shifts to density functional methods (DFT) and the approximations which have been used, followed by a quick overview of their practical implementation within the AIMPRO DFT/LDA approach.

3.1 The Schrödinger equation

Solid state materials are composed of electrons and nuclei which themselves are ‘elementary particles’ whose behavior can be described by the laws of quantum mechanics. The aim of ab initio methods is to extract information about physical systems beginning from fundamental quantum theory alone without the use of any empirical or experimental input as data. This is not easy to achieve, since the exact solution to the Schrödinger equation is too complex to allow a direct solution for all cases except the most simple (e.g. H_2). Despite these difficulties, ab initio methods have been invaluable in rationalizing experimental materials, and in making accurate predictions of the properties of a wide range of materials. This success is due to the existence of reasonable approximations that make the theory tractable by numerical means, the development of robust and efficient algorithms that assist in optimizing the computational requirements and the availability of increasingly powerful workstations and parallel computers.

3.2 The Many-Body Problem

Fundamental to any ground state electronic structure determination method is finding the

solution to the Schrödinger equation for a system of interacting particles.

The Time independent non-relativistic Schrödinger equation is given as:

$$\hat{H}\Psi = E\Psi \quad (1)$$

Where \hat{H} is the Hamiltonian operator, Ψ is wavefunction of the system and E is the total energy of the system. The total Hamiltonian for a many body system containing N electrons and W nuclei can be expressed in terms of its nuclear and electronic kinetic energy, (T_{nuclear} and $T_{\text{electronic}}$) and a Coulomb attractive term between the charge species, ($V_{\text{electron-electron}}$, $V_{\text{nucleus-nucleus}}$ and $V_{\text{electron-nucleus}}$) in atomic units.

$$\hat{H} = T_{\text{nuclear}} + T_{\text{electronic}} + V_{\text{electron-electron}} + V_{\text{nucleus-nucleus}} + V_{\text{electron-nucleus}} \quad (2)$$

$$= -\frac{1}{2} \sum_{k=1}^W \frac{1}{M_k} \nabla_k^2 - \frac{1}{2} \sum_{i=1}^N \nabla_i^2 + \sum_{i=1}^N \sum_{j>1}^N \frac{1}{r_{ij}} + \sum_{k=1}^W \sum_{l>k}^W \frac{Z_k Z_l}{R_{kl}} - \sum_{i=1}^N \sum_{k=1}^W \frac{Z_k}{r_{ik}} \quad (3)$$

where M_k and Z_k are respectively the mass and charge of the nuclei, R_{kl} is the distance between nuclei k and l , r_{ik} the distance between electron, i and the nuclei, k and r_{ij} is the distance between the electrons i and j .

The exact solution to the Schrödinger equation is only soluble for very small systems such as H_2 and He , but not for systems containing large number of atoms, approximations are therefore needed to simplify the Schrödinger equation in these larger systems.

3.3 General Assumptions

3.3.1 Born-Oppenheimer approximation

In general the nuclei of atoms (containing protons and neutrons) are much heavier than electrons. This means that the electrons will respond much faster to their environment than the nuclei. This assumes that the electrons respond instantly on the timescale of the nuclei, i.e. as far as the electrons are concerned, the nuclei can be considered as stationary, which therefore becomes possible to solve the Schrödinger equation for a set of electrons in the presence of static atoms.

This then reduces the Hamiltonian to its electronic parts only:

$$\hat{H}_{\text{electronic}} = T_{\text{electronic}} + V_{\text{electronic-electronic}} + V_{\text{electron-nucleus}} \quad (4)$$

$$= -\frac{1}{2} \sum_i^N \nabla_i^2 + \sum_{i=1}^N \sum_{j>1}^N \frac{1}{r_{ij}} - \sum_{i=1}^N \sum_{k=1}^W \frac{Z_k}{r_{ik}} \quad (5)$$

This first approximation is not sufficient to make the Schrödinger equation soluble for our systems, since there remains the complexity of the correlated behaviour of the electrons.

Next we solve the many body Schrödinger equation for the electrons. Historically there have been several approaches for this.

3.4 Hartree Equation

The Hartree approximation [1] is one of the earliest proposals in solving the electron-electron interactions in many-body Schrodinger equations. It states that, the total electron wavefunction can be represented by the product of single electron wave functions

$$\Psi(\mathbf{r}_1, \mathbf{r}_2, \dots, \mathbf{r}_N) = \psi(\mathbf{r}_1)\psi(\mathbf{r}_2)\dots\psi(\mathbf{r}_N) \quad (6)$$

$$= \prod_i \psi_i(\mathbf{r}_i) \quad (7)$$

This assumes that each electron moves in a field as a result of other electrons.

Hence the potential term in the Schrödinger equation for electron i is,

$$V_i(\mathbf{r}) = \sum_{\alpha} \frac{-Z_{\alpha}e}{|\mathbf{r}_{\alpha} - \mathbf{r}_i|} + \sum_{j \neq i} \int \frac{|\psi_j(\mathbf{r}')|^2}{|\mathbf{r} - \mathbf{r}'|} d\mathbf{r}' \quad (8)$$

This approximation leads to surprisingly accurate results [1], but suffers a draw back due to the lack of electronic exchange, i.e. the many body wavefunction is not antisymmetric with respect to the switching of two of the electrons [2]. This violates the Pauli exclusive principle which forces a change of sign of the total wavefunction when two electrons are switched.

3.5 Hartree-Fock Theory

The Hartree product fails in satisfying all the necessary criteria for a wavefunction as a result of the fact that electrons are fermions and must change sign if two electrons change places with each other which is known as the antisymmetry principle.

A better approximation to the wavefunction therefore, involves the use of a Slater determinant. In this approach, the N-electron wavefunction is formed by combining one-electron wavefunctions in a way that satisfies the antisymmetry principle. This is done by expressing the overall wavefunction as the determinant of a matrix of single-electron wavefunctions,

$$\psi(r_1 s_1, \dots, r_N s_N) = \frac{1}{\sqrt{N!}} \begin{vmatrix} \psi_1(r_1 s_1) & \psi_1(r_2 s_2) & \dots & \psi_1(r_N s_N) \\ \psi_2(r_1 s_1) & \psi_2(r_2 s_2) & \dots & \psi_2(r_N s_N) \\ \dots & \dots & \dots & \dots \\ \psi_N(r_1 s_1) & \psi_N(r_2 s_2) & \dots & \psi_N(r_N s_N) \end{vmatrix} \quad (9)$$

The columns in the Slater determinants are single-electron wave function orbitals, while the row is made up of the electron coordinates.

On the whole, the solution to the HF equation is found by making an initial guess at the wave function and iteratively approaching self-consistency. This is accomplished by continuously feeding the potential due to the electrons back into the equation until a considerable level of similarity is seen between the input and output within some tolerance limit.

The main limitations of the HF methods are; (a) high computational cost involved in generating the integrals for the matrices limits its applications to relatively small systems, (b) lack of electron-correlation, gives a zero density of states at the Fermi level in the simple case of the homogenous electron gas. To overcome this hurdle other methods such as Configuration interaction or Coupled Cluster and Møller-Plesset Perturbation theory, which are collectively called Post Hartree-Fock methods, all aim to incorporate correlation via different methods. While successful, this increases the computational expense astronomically.

3.5.1 Møller-Plesset perturbation Theory (MP)

This theory [3] looks to include electron correlation effects with Rayleigh-Schrödinger perturbation theory (RS-PT). This is the first of several methods that works to remove the deficiency from the Hartree-Fock method. It gets its name from the fact that in the molecular system, electrons are ‘perturbed’ or moved from a ground state to an excited state and then allowed to fall back to the ground state.

There are several levels of MP theory, indicated by the number following the abbreviation “MP” as in MP2, MP3, MP (n).

3.5.2 Configuration Interaction (CI)

Configuration interaction (CI) wave function is a multiple determinant wave function method. This is made by beginning with HF wave function and making new determinants by promoting electrons from occupied to unoccupied orbitals. CI is classified by the number of excitations used in making each determinant. For instance, if one electron is moved for each determinant, this is called a configuration interaction single-excitation (CIS) calculation. Other forms of combinations exist depending on the accuracy of the results required.

3.5.3 Coupled Cluster Theory

These calculations are similar to configuration interaction, in that the wave function is a linear combination of many determinants, although choosing the determinants in coupled cluster calculations is more cumbersome than the choice of determinant in CI. Different forms of combinations such as CCSD, CCSDT, etc. can be formed.

However the computational cost associated with this technique means it is only appropriate for small systems.

3.6 Density Functional Theory (DFT)

This is the approach used in this thesis work. It is based on the hypothesis that [4]“knowledge of the ground state density $n(\mathbf{r})$ for any electronic system (with or without interactions) uniquely determines the system.”

Instead of taking the wave function approach, a charge density, $n(\mathbf{r})$, is considered as the main fundamental variable. The use of charge density considerably reduces our many-body problem from one with $3N(+1)$ variables in the case of the wave function method to only three (x,y,z) spatial coordinates (+1 if spin is included).

DFT, was first developed by Hohenberg and Kohn [5] and then later by Kohn and Sham [6], (Kohn-Sham were given a Nobel Prize in Chemistry in 2000 for their work). The main idea of their work is the use of charge density as the principal variable in solving the many-body Hamiltonian problem encountered earlier on through the use of wave function methods such as the Hartree-Fock approach.

DFT is a ground state theory, meaning the unoccupied states are treated very poorly often leading to errors when calculating the band gap. In addition it is not well adapted for studying excited states.

The first assumption on the use of charge density was coined Thomas-Fermi theory in 1927. Although, the theory is quite useful in describing the total energies of atoms, when it comes to Chemistry and Materials science, which involves valence electrons, it has no use [4].

3.6.1 Thomas-Fermi Theory

In this model, the kinetic energy of a non-uniform system is described by the uniform electron gas expression which is represented as a functional of the electron density n :

$$E_k[n] = \int \frac{3}{10} (3\pi^2)^{\frac{2}{3}} n^{\frac{5}{3}}(r) dr \quad (10)$$

In which the total Thomas-Fermi energy (E_{TF}) as a function of one electron density can be written as:

$$E_{TF}[n(\mathbf{r})] = \int v(\mathbf{r})n(\mathbf{r})dr + \int \frac{3}{4} (3\pi^2)^{\frac{2}{3}} n^{\frac{5}{3}}(\mathbf{r})dr + \frac{1}{2} \int \frac{n(\mathbf{r})n(\mathbf{r}')}{|\mathbf{r}-\mathbf{r}'|} drdr' \quad (11)$$

Where the first term in equation (11) is the nuclear-electron attraction, second is the kinetic energy and lastly, the electron –electron repulsion.

This method, though successful to some extent, does not lead to any chemical binding in molecules and also the mathematical proof is not robust, hence there was an urgent need to solve this problem, which was provided by Hohenberg and Kohn.

3.6.2 Hohenberg and Kohn Theorem

The ground-state density $n(\mathbf{r})$ of a bound system of interacting electrons in some external potential $v(\mathbf{r})$ determines this potential uniquely, this is known as the Hohenberg and Kohn Lemma [4]. In other word this means that, there is a one-to-one correspondence between the electron density of a system and the energy. The intuitive proof of why the density completely defines the system is credited to E.B. Wilson [7], in which he argued that:

- (a) The integral of the density defines the number of electrons.
- (b) The cusps in the density define the position of the nuclei.
- (c) The heights of the cusps define the corresponding nuclear charges.

Hohenberg and Kohn demonstrated that, any two systems with different potentials will have different ground-state energy and also, the ground-state density minimizes the total electronic energy of the system. The following is a summary of their proof.

Here, a universal function for the energy $E(n)$ based on density $n(\mathbf{r})$ can be defined;

Let $n(\mathbf{r})$ represent the non-degenerate ground-state density of N electrons in a potential $v_1(\mathbf{r})$ corresponding to the ground-state wave function Ψ_1 , and the energy E_1 . Then,

$$E_1 = (\Psi_1, H_1 \Psi_1) \quad (12)$$

$$= \int v_1(r)n(r)dr + (\Psi_1, (T + U)\Psi_1) \quad (13)$$

H_1 is the total Hamiltonian corresponding to v_1 , T and U are the kinetic and interaction energy operators. And suppose that a second potential exists, $v_2(\mathbf{r})$, which is not equal to $v_1(\mathbf{r}) + \text{constant}$, with a ground-state wave function, Ψ_2 , which gives rise to the same $n(\mathbf{r})$. Then

$$E_2 = \int v_2(r)n(r)dr + (\Psi_2, (T + U)\Psi_2) \quad (14)$$

Applying the variational principle for the non-degenerate Ψ_1 gives the inequality

$$E_1 < (\Psi_2, H_1 \Psi_2) \quad (15)$$

$$= \int v_1(r)n(r)dr + (\Psi_2, (T + U)\Psi_2) \quad (16)$$

$$= E_2 + \int [v_1(r) - v_2(r)]n(r)dr \quad (17)$$

A similar expression can be constructed for E_2

$$E_2 \leq (\Psi_1 H \Psi_1) = E_1 + \int [v_2(r) - v_1(r)] n(r) dr \quad (18)$$

Addition of equation E_1 and E_2 yields the final expression

$$E_1 + E_2 < E_1 + E_2. \quad (19)$$

The inequality is logically false meaning there is a contradiction of the process, and therefore the assumption for the existence of a second potential $v_2(\mathbf{r})$, which is unequal to $v_1(\mathbf{r}) + \text{constant}$ and result in the same $n(\mathbf{r})$ must be false. Therefore, no two different potentials have the same $n(\mathbf{r})$. Each potential has its own unique density from which the Hamiltonian can be determined.

Kohn & Sham defined a functional $F[n(\mathbf{r})]$, independent of N and $v(\mathbf{r})$ which takes the form,

$$F[n(\mathbf{r})] = T[n(\mathbf{r})] + E_H[n(\mathbf{r})] + E_{xc}[n(\mathbf{r})], \quad (20)$$

Where T is the kinetic energy term for a given charge density E_H is the Hartree energy and E_{xc} is the exchange-correlation energy of the electron gas.

E_H is given by

$$E_H[n(\mathbf{r})] = \frac{1}{2} \int \frac{n(\mathbf{r})n(\mathbf{r}')}{|\mathbf{r} - \mathbf{r}'|} d\mathbf{r}d\mathbf{r}' \quad (21)$$

Since both the kinetic energy and the exchange-correlation energy are complex to express in terms of the density, the Kohn-Sham equation is adopted in determining T and that of E_{xc} ,

which commonly involves the use of one of two approaches, either the Local density approximation (LDA) or the Generalized gradient approximation (GGA).

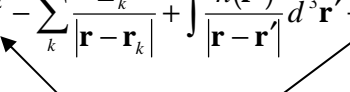
We now discuss Kohn-Sham theory further.

3.6.3 Kohn-Sham Theory

The aim of Kohn-Sham theory is to calculate the kinetic energy under the assumption of non-interacting electrons. In real situation, the electrons are interacting and this does not give the total kinetic energy. However, the difference between exact kinetic energy and that calculated by assuming non-interacting orbitals is small and therefore, the remaining energy is adsorbed into an exchange-correlation term which is implemented in the DFT energy expression.

Kohn and Sham [6] introduced the idea of using orbitals in order to solve the kinetic energy term in the Hamiltonian. Their suggestion is to split the kinetic functional into two parts, one which can be calculated exactly, and a small correction term. However, there is a price to pay by re-introducing the orbitals, whereby increasing the complexity from 3 to 3N variables, in which electron correlation re-emerges as a separate term (One term describes the kinetic energy for the independent electrons, the 2nd term corrects this for real interacting electrons).

This allows the total Schrödinger kinetic equation to be used, which then gives an overall set of one-electron equation

$$\left[-\frac{1}{2}\nabla^2 - \sum_k \frac{Z_k}{|\mathbf{r}-\mathbf{r}_k|} + \int \frac{n(\mathbf{r}')}{|\mathbf{r}-\mathbf{r}'|} d^3\mathbf{r}' + \frac{\delta E_{xc}[n(\mathbf{r})]}{\delta n(\mathbf{r})} \right] \psi_\lambda(\mathbf{r}) = \varepsilon_\lambda \psi_\lambda(\mathbf{r}) \quad (22)$$


These are the 2 parts

The charge density can then be written by summing over all N occupied states;

$$n(\mathbf{r}) = \sum_{\lambda=1}^N |\psi_\lambda(\mathbf{r})|^2. \quad (23)$$

The first three terms in equation (22) represent the Kinetic energy, external potentials (due to ions) and Hartree contributions. The fourth term contains the exchange and correlation information of the system.

According to Parr and Yang [8], the total energy of a system can also be expressed as another functional of the charge density,

$$E[n(\mathbf{r})] = \sum_{\lambda=1}^N \varepsilon_{\lambda} - J[n(\mathbf{r})] + E_{xc}[n(\mathbf{r})] - \int V_{xc}[n(\mathbf{r})]n(\mathbf{r})d\mathbf{r} \quad (24)$$

Where J and V_{xc} are the Hartree and exchange-correlation potential respectively, given by,

$$J[\mathbf{r}] = \frac{1}{2} \int \frac{n(\mathbf{r})n(\mathbf{r}')}{|\mathbf{r} - \mathbf{r}'|} d\mathbf{r}d\mathbf{r}', \quad (25)$$

and

$$V_{xc}[\mathbf{r}] = \frac{\delta E_{xc}[\mathbf{r}]}{\delta n(\mathbf{r})}. \quad (26)$$

Hence, equation (22) and (23) can be solved iteratively until self-consistency is reached to give the ground-state density of the system, which then gives the total energy in equation (24).

The major setback in this theory is that, the exact exchange and correlation energies are not known and therefore, we resort to two approximations which have been used successfully to address this problem.

3.7 Methods for the Treatment of $E_{xc}[n(\mathbf{r})]$

The Kohn-Sham theory assumes the kinetic energy for independent electrons.

Had it not been for exchange and correlation effects, the electrons will move independently of each other. But, this is not the case, their motions are coupled.

The Pauli-exclusion principle states that no two fermions could occupy the same quantum mechanical state [9], which in this case reduces to the fact that two electrons of the same spin cannot occupy the same position in space. Consequently, the many-body wave function must be anti-symmetric under exchange of any two electrons and the energy required to fulfill this anti-symmetric condition is known as the *exchange energy*.

Correlated motion between the electrons and the associated energy contribution is known as *correlation energy*. This term is absent in the Hartree-Fock theory.

Both electron correlation interaction and electronic exchange reduce the probability of two electrons being close to each other. Exchange and Correlation energies must be included in the total system energy.

The two most common approximations used for the exchange-correlation term are, the Local density approximation (LDA) or for systems with non-zero net spin the Local spin density approximation (LSDA) [6,10,11], and Generalized gradient approximation (GGA).

3.7.1 Local Density Approximation (LDA)

Within the LDA, the exchange-correlation energy at a point is taken to be equal to the exchange-correlation energy of a uniform-electron gas with the same electron density n . At a point in space, \mathbf{r} , the contribution to the exchange-correlation energy is approximated in LDA as,

$$E_{xc}[n(\mathbf{r})] = \int n(\mathbf{r})\epsilon(n(\mathbf{r}))d\mathbf{r} \quad (27)$$

where $\epsilon(n(\mathbf{r}))$ is the exchange-correlation energy per electron in a uniform-electron gas of density $n(\mathbf{r})$. The exchange correlation energy for a uniform electron gas can be calculated analytically. This is the simplest solution to find the exchange correlation energy and works surprisingly well.

Improvements in the functional can be constructed by considering the spin-polarization of the system, by introducing $n_{\uparrow}(\mathbf{r})$ and $n_{\downarrow}(\mathbf{r})$ which are respectively the spin-up and spin-down electron densities.

In this case the exchange and correlation functional is separable in spin and the overall contribution of the functional E_{xc} can be written as the sum of two spin dependent functionals,

$$E_{xc}[n_{\uparrow}(\mathbf{r}), n_{\downarrow}(\mathbf{r})] = E_x[n_{\uparrow}(\mathbf{r}), n_{\downarrow}(\mathbf{r})] + E_c[n_{\uparrow}(\mathbf{r}), n_{\downarrow}(\mathbf{r})], \quad (28)$$

where, $n_{\uparrow}(\mathbf{r})$ and $n_{\downarrow}(\mathbf{r})$ are charge densities for spin-up and spin-down electrons respectively, which are consistent with non-zero spin of the system, and the exchange functional has been shown to have analytical form for a homogeneous electron gas [10],

$$E_x[n_{\uparrow}(\mathbf{r}), n_{\downarrow}(\mathbf{r})] = -\frac{3}{2} \left(\frac{3}{4\pi} \right)^{1/3} (n_{\uparrow}^{4/3}(\mathbf{r}) + n_{\downarrow}^{4/3}(\mathbf{r})). \quad (29)$$

For any small region in the system, this assumption is also accurate for the zero net spin case.

Although E_c , has a small energetic contribution, it is considered to be the more complicated term. Ceperley and Alder first parameterized E_c , for a uniform electron gas by quantum Monte Carlo calculations [12]. Later, it was parameterized by Perdew and Zunger [11]. There have also been slight improvements in the parameterization by Perdew and Wang [13]. Other parameterizations such as Vosko-Wilk-Nusair also exist [14].

Even though the LDA is successful in some cases such as inhomogeneous systems when the charge density is slowly varying; it has been very consistent in predicting some structures and large scale properties, but some well known problems are inherent as well.

The energies of excited states and band gaps in semiconductors and insulators are systematically under predicted. This is attributed to the fact that, DFT is a ground-state theorem only, and not for excited states. Band gaps in solids and energy gaps between the

highest occupied molecular orbital (HOMO) and that of the lowest unoccupied states (LUMO) are also under predicted, due to electron self-interaction in the energy functional, which is interaction of an electron with Coulomb and exchange-correlation potential arising from itself.

Prediction of wrong ground-states for some magnetic systems with the most notable example being that of Fe, which is predicted to be hexagonal close packed and non-magnetic instead of body-centered cubic and ferromagnetic, also strongly correlated systems such as Mott insulators NiO and La₂CUO₄ are predicted by LDA to be metallic [15].

It is also known to underestimate atomic ground-state energy and ionization energy, while overestimating binding energies and giving shorter bond lengths as compared to experimentally obtained bond lengths, also compared to results of post Hartree-Fock methods.

However it gets very well graphite interlayer spacing, elastic constants, and heat capacity [16] and also in the description of the interactions between polyaromatic hydrocarbons with other carbon materials [17], this is why we use it in this thesis.

3.7.2 Generalised Gradient Approximation (GGA)

The GGA, was developed in order to improve upon the LDA, based on the observation that the electron gas is not uniform. Therefore, a better way of expressing the exchange-correlation term based on the GGA is by including the derivative of the density in the E_{xc} functional which should give a more accurate description of the true exact exchange-correlation contribution to the energy. The expression takes the form;

$$E_{xc}^{GGA}[n] = \int n(\vec{r}) \mathcal{E}_x^{\text{hom}}[n(\vec{r})] F_{xc}[n(\vec{r}), |\Delta n(\vec{r})|, \dots] d\vec{r} \quad (30)$$

F_{xc} is dimensionless, and $\mathcal{E}_x^{\text{hom}}[n(\vec{r})]$ is the exchange energy term of a uniform electron gas of density n .

In this approach, there is a dependence of the exchange-correlation functional on the gradient of the electron density. As direct expansions in gradients violate the sum-rule for the

exchange hole, a number of authors have proposed corrections to the sum-rules on the generalized gradient expansion. However, there is no consensus, on the most robust GGA method.

The two common parameterizations of this approach are given by Perdew and Wang (PW91) [13] and Perdew, Burke and Ernzerhof (PBE) [18]. Even with this approach the band gap problems encountered in LDA still remain unsolved.

Again, there are some instances where the GGA has been reported to over correct the deficiencies in LDA which eventually leads to under-binding [17]. Some of the most classical cases are with the noble gas dimers and molecular nitrogen crystals which by GGA will not exist as bound entities [7-8]. Further limitations of GGA are incorrect estimation of hydrogen bonding leading to wrong freezing point of water estimations [7].

Both the LDA and GGA do not account for systems with long range Van der Waals even though LDA is able to predict the interlayer interactions in graphites correctly where GGA does badly [16-17].

3.7.3 The Hybrid Methods

Hybrid methods for the treatment of the $E_{xc}[n(\mathbf{r})]$, has also been put forward. The idea is to combine the standard DFT $E_{xc}[n(\mathbf{r})]$ functionals with the Hartree-Fock exact exchange term (E_x^H). The most commonly used of these approaches is that of the B3LYP functional [19,20], combining the Becke exchange functional [21] with the Lee, Yang and Parr correlation functional [22] in a linear combination with E_x^H

These three parameters are fitted to experimental data and the resultant functional has been shown to perform well with systems containing for example, π - π stacking, where the performance of conventional approaches often fail to produce the desired results.

Another approach to be adopted in a future version of our DFT AIMPRO code is “screened exchange” [7].

3.8 Pseudopotentials

An additional approximation that is made in many electronic structure determination methods is the pseudopotential approximation. Indeed, approximations are not only limited to DFT calculations alone. The main idea is to replace the core electrons and the nuclear potential with an effective screened potential, the pseudopotential, which then acts upon a set of pseudo wave functions. The assumption for this is that, the core electrons are highly localised and don't participate in any chemical bonding process. Furthermore, an all-electron calculation gives large total energies and this will result in large error bars when comparing the energies of similar structures and also since there is rapid oscillation of valence electrons wavefunctions in the core region to maintain orthogonality with the core states, which makes it expensive due to the fact that, large fitting functions with appropriate basis set is needed.

In the construction of pseudopotentials, two main assumptions are made; (1) the frozen core, where the core electrons are presumed to be unperturbed by the specific local environment of the atom. This then enables the pseudopotential to become transferable between the systems. (2) Small core approximation, where the assumption is based on a negligible overlap between the core and the valence electrons, which makes them separable. This allows the exchange-correlation functional to be written for the separable core and valence states, hence the exchange-correlation functional becomes the sum of two independent functionals ($E_{xc}(n_{\text{core}} + n_{\text{valence}}) = E_{xc}(n_{\text{core}}) + E_{xc}(n_{\text{valence}})$). Additionally, one of the requirements for many pseudopotentials is that the associated pseudo-wavefunction gives the same total charge density as obtained from the original wavefunction. The term norm-conserving, is used for this sort of pseudopotential which is what we use in this thesis. One major disadvantage of pseudopotentials is that the calculations of quantities associated with the core electrons will not be possible, for example core electron energy loss spectra, though other methods [23,24] are available for the reconstruction of the core electrons.

It was Hans Hellman (1903) [25], who first introduced pseudopotential approximations. There are three kinds of pseudopotential types in AIMPRO:

- (1) Hartwigsen, Geodecker and Hutter (HGH) [26], which is the pseudopotential designed specifically for efficiency with a Gaussian basis set and used in this thesis

work.

- (2) Bachelet, Hamann and Schlüter (BHS) [27]
- (3) Troullier and Martins (TM) [28].

3.9 Basis Sets

One of the major tasks that are encountered when implementing the DFT method is how to represent Kohn-Sham states and the charge density. The functions in which these are expanded are known as basis functions, which are collectively called basis sets.

Basis set functions are normally in the form of Gaussians orbitals, plane waves or Slater orbitals.

The AIMPRO package uses localised real space Cartesian Gaussian type orbitals (GTO) as its basis sets in which each GTO is centred on an atom \mathbf{R}_i given by,

$$\phi(\mathbf{r} - \mathbf{R}_i) = (x - R_{ix})^{n_1} (y - R_{iy})^{n_2} (z - R_{iz})^{n_3} e^{-\alpha(\mathbf{r} - \mathbf{R}_i)^2} \quad (31)$$

where n_1 , n_2 and n_3 are integers that determine the symmetry of the orbitals. The type of the orbital is determined by the choice of the integers: $n_1 = n_2 = n_3 = 0$ gives an s-orbital, fixing $n_1 + n_2 + n_3 = 1$ gives p-orbital in the x-, y- or z- directions whilst setting $n_1 + n_2 + n_3 = 2$ gives a total of five d- and one s-orbital.

One of the major advantages in using Gaussian orbitals is that their matrix elements can be found analytically. In addition, they can be made to decay rapidly away from the atom, thereby resulting in many of the elements of the Hamiltonian matrices being zero.

For use in periodic boundary conditions, a linear combination of the GTO's that satisfy the Bloch's theorem is used, which can be used to solve the Kohn-Sham equations.

The GTO, has a number of advantages in their use as compared to other basis functions and as compared to plane waves (PW). The fast decay leads to an efficient evaluation of matrix elements for the density and Hamiltonian than if the function were longer ranges. This then results in an increase in efficiency for larger systems. Another advantage is the ability to

increase the number of functions within a specific localised region as one requires which is unlike in plane wave method, where the level of the accuracy is constant for the system being modelled. But, it's not easy to show that increasing the number of Gaussian function has resulted in a converged answer. In fact, due to the non-orthogonal nature of these functions, addition of extra functions can result in instability because of over-completeness. Over-completeness is said to occur when too many similarly constructed basis functions (for instance, with similar or equal exponents and equal but opposite coefficient) are included, giving rise to instabilities within the self-consistency cycle. This is contrary to PW, where the results are said to converge with the number of increasing basis functions. However, the PW approach has serious drawbacks, in that it has extreme difficulty in expanding a localised wavefunction and also, due to the periodic nature of PW, for non-periodic systems the vacuum region will be unnecessarily well described. Furthermore, due to the large number of PW required to describe the core region, additional modifications to the pseudopotential is needed to allow for a larger core region, and such pseudopotentials are termed ultrasoft pseudopotentials [29].

3.9.1 Basis sets used in this work

The basis sets used for Carbon(C), Hydrogen (H), Bromine (Br) for the modelling of PPV Polymer, SWCNTs, graphene and graphite, are constructed as follows; (i) pdpp and pddd which corresponds to 22 and 38 functions respectively for each carbon atom. We started with pdpp basis function for computational efficiency but later shifted to pddd which is thought to give a better description for the inter-layer interaction in graphites and other related carbon compounds. This is discussed later in the thesis. (ii) pppp with 16 functions per H atom and (iii) fddd containing 50 functions for each Br atom.

Here, p refers to $n_1 + n_2 + n_3 \leq 1$, i.e. 4 functions, d refers to $n_1 + n_2 + n_3 \leq 2$, with 10 functions, and f refers to $n_1 + n_2 + n_3 \leq 3$ with 20 functions.

3.10 Self-Consistency

The Kohn-Sham equations must be solved self-consistently, i.e. the electrons are allowed to redistribute throughout the system freely until the lowest system energy is achieved. This implies that, the charge density generated by an external potential is the same as that which gave rise to the potential within some tolerance. In order to achieve this, an initial guess at the charge density is usually taken from the neutral atom or from the output of a prior calculation. In this work, self-consistency of charge density is believed to be achieved when the difference in Hartree energies between two consecutive self-consistent cycles is less than 10^{-7} a.u.

3.11 Structural Optimisation

For a given starting geometry, the lowest energy arrangement of those atoms in that coordination can be found once the self consistent solution to the Kohn-Sham equation is obtained. In order for this to be achieved, a structural optimisation must be performed; this then requires a knowledge and minimisation of the forces on each atom. These forces can then be used to produce a search direction to minimize the energy of the system with respect to the atom positions.

The forces on each atom (a) can be given analytically as

$$f_{la} = -\frac{\delta E}{\delta R_{la}}, \quad l = x, y, z \quad (32)$$

where R_{la} is the position of atom and l is the direction of force and this can be evaluated by calculating δE for a displacement δR_{la} . This then gives the formulation of the forces with no derivatives of the wave function coefficient, as required by the Hellmann-Feynman theorem and is corrected for the pulay forces that result from incomplete bases, such as the atom centre Gaussians used in the AIMPRO code [30].

Optimization of the structures starts by moving the atoms in order to minimize their energy. This is achieved in AIMPRO by making use of the conjugate gradient method [31,32], in

minimizing a function by ensuring that an energy minimum is located. The search algorithm simply reduces the energy from the initial value it is given, to the nearest local minimum; the algorithm is incapable of determining whether this is the global system minimum or not. The best way to achieve a global minimum is to try relaxing several different starting structures. By taking the energy as a function to be minimised with respect to the atomic positions, knowledge of the forces on the atoms is required. Moving all the atoms in unison in the direction of the forces will result in new structures. The energy along the displacement direction is approximated to a quadratic or cubic interpolation and the amount of atomic movements is chosen to arrive at a position with the minimum energy.

All the structures presented in this thesis were fully optimised until the energy change in a given structural optimization iteration was less 10^{-7} eV.

3.12 Vibrational Modes

The major importance of a theoretical calculation is to validate concepts and also make realistic predictions where experiments cannot be conducted. In other words, important information can be gained from theoretical calculations and compared with available experimental data and one of them is the vibrational modes of materials. Optical spectroscopy (such as Raman and Infra red spectroscopy) results could be compared directly with calculated modes.

Therefore, a very useful capability is to be able to simulate atomic vibrations of systems. In order to simulate theoretically atomic vibrations, the second derivative of the energy with respect to the displacement of the atoms is required. This is done initially by optimizing fully the system until the forces between atoms are zero, within a chosen tolerance with a final self-consistent charge density. An atom **a** is then subjected to a displacement ε along the direction l . The self-consistent charge density is then recalculated. Then atom **b** feels a force along a direction m given by $f_{mb}^+(l, a)$. The displacement is next repeated such that it is given by $-\varepsilon$, then, this will also correspond to a force $f_{mb}^-(l, a)$.

This then implies that it is possible to calculate the energy second derivative up to second order in ε ,

$$\mathbf{D}_{la,mb} = \frac{(f_{mb}^+(l,a) - f_{mb}^-(l,a))}{2\varepsilon} \quad (33)$$

when the full dynamical matrix \mathbf{D} is determined, it can then be diagonalized and scaled by the square root of the atomic masses, to give the eigenvalues as the vibrational modes within the context of the harmonic approximation (where $\varepsilon \rightarrow 0$). But this method is actually termed *quasi-harmonic* [33] due to the fact that this is a numerical difference in the forces, not an analytical second differential and the $\mathbf{D}_{la,mb}$ contains all even terms in ε thus, there will be some *anharmonic* contributions included.

This method was employed in this work to generate the vibrational modes for bromine doped substrates which has been described elsewhere in the text.

3.13 Fermi Statistics (Level Filling)

In systems with small band gaps, often convergence in the self-consistency cycle for the electronic charge distribution becomes very slow or if not impossible due to the occurrence of *charge sloshing*. In one self-consistency cycle, electrons may be transferred from the (bottom of the valence band) to the (top of the conduction band) which then results in the switching of the electronic levels due to the Coulombic repulsion between electrons in the same level, and when another iteration cycle occurs, the levels switch back. In this way, self-consistency is never reached. In such a situation, it is relevant to smear out the occupation of the electronic levels into a finite temperature distribution using Fermi Statistics. This can often be used in practice during optimization and then turned off when the structure has been relaxed beyond the level where the electronic levels cross. This temperature is not physical and is purely a computational trick to avoid these self-consistency problems.

However, the use of Fermi statistics can sometimes give incorrect structures and such is the case in which the mechanisms contributing to Jahn-Teller distortion is removed when this feature is on. In addition it can dampen out high spin solutions.

In this thesis work, the finite temperature smearing, k_bT , was chosen as 0.04 eV, as this is the standard value used in many graphite calculations.

3.14 Brillouin Zone (k-point sampling)

The first Brillouin zone (BZ), is the region of reciprocal space in which all eigenstates of the electrons from the unit cell can be represented and its shape depends on the symmetry of the crystal being investigated.

When periodic boundary conditions are used in a supercell, the calculation of physical observables requires integration over the entire Brillouin zone (BZ). Generally, the integrand has no simple analytical solution, although it is periodic in reciprocal space; however a numerical integration can be performed.

The method involves taking a dense mesh of points to sample the BZ, but this is practically demanding due to the computational cost involved in calculating the Kohn-Sham states for each point in the zone. Consequently, a number of schemes have been developed to average the value of the physical quantities over a small number of \mathbf{k} -points. The computational cost can further be reduced if one could take a single \mathbf{k} -point in a given volume of the zone as representative of the average effect of all the \mathbf{k} -points within that zone or volume. The scheme introduced by Monkhorst and Pack (MP) [34], which is also implemented in the AIMPRO code, gives correctly the averaging over the entire BZ at the same time keeping the computational expense much lower to converge. For a given BZ with volume $(2\pi)^3 / \Omega$, the average \bar{f} is given by

$$\bar{f} = \frac{\Omega}{(2\pi)^3} \int f(\mathbf{k}) d\mathbf{k} \approx \frac{1}{N} \sum_{n=1}^N f(\mathbf{k}_n), \quad (34)$$

where N is the number of sampled \mathbf{k} -points. The MP model is based on equally spaced points along three directions in reciprocal lattice spaces, termed special \mathbf{k} -points, which are dependent on the shape of the BZ, and are given for a set of primitive lattice vectors $\mathbf{b}_{(1,2,3)}$ by

$$\mathbf{k}(i, j, k) = u_i \mathbf{b}_1 + u_j \mathbf{b}_2 + u_k \mathbf{b}_3 \quad (35)$$

where $u_{(i,j,k)}$ are prefactors give by

$$u_{(i)} = (2i - I - 1)/2I, u_{(j)} = (2j - J - 1)/2J, u_{(k)} = (2k - K - 1)/2K \quad (36)$$

and I, J and K are numbers for the special \mathbf{k} -points. This is evaluated using the formula over a $I \times J \times K$ grid of points, in order to reduce the computational expense. Clearly, the \mathbf{k} -point density determines the accuracy of the calculations in reciprocal space. Therefore, a system with a larger unit cell (smaller BZ) will require a fewer number of \mathbf{k} -points to model the system accurately, however proportionally, the computing time increases with the number of atoms and each \mathbf{k} -point becomes harder to treat as the atom numbers increases hence it is necessary to achieve a balance between the system size and the number of \mathbf{k} -points in order to achieve the highest level of accuracy within a reasonable computing time.

In this thesis work, calculations were done using the MP scheme in which the \mathbf{k} -point grids sizes are given in the text for the different materials studied.

3.15 Boundary Conditions

An important issue when solving the DFT problem is to consider the effects of boundary conditions. These boundary conditions are either periodic or non-periodic which are important to the electronic structures of molecules and crystals. This can be further explained in terms of the extent to which the structure fills the unit cell; (i) When one has full structural

periodicity, meaning the unit cell being modelled has no vacuum regions and the structure is repeated in all directions (x, y, z), this is a bulk material, (ii) if the structure repeats only in two directions (x and y) but the z direction is separated by vacuum, then one is able to model a surface and (iii) if there is no periodicity, i.e. when the unit cell structure is surrounded by vacuum, then one is modelling particle-in-a-box, which is a non-interacting gas of molecules system.

In this thesis work, the periodic supercell method was used to model the interactions between the various carbon materials (single-walled nanotube, graphites, graphene and Poly-para phenylene vnylene oligomer) and bromine molecule (adsorbate), using all three of the above situation as appropriate. It is important to ensure that the vacuum spacing in a given direction is sufficient that the systems are genuinely decoupled, and this is discussed further in the results section.

3.16 Supercell Approach

Both non-periodic cluster and supercell runs are possible in the AIMPRO code. In this thesis we only used the supercell approach.

Carbon materials and the adsorbate were treated in periodic boundary conditions by placing them in a unit cell. This is achieved by generating a lattice vector \mathbf{L}_α , and containing a basis of atoms \mathbf{R}_i where $i=1, 2 \dots N$, with N being the number of atoms in a unit cell. A continuous condition is then applied to repeat unit cells with the positions of all atoms given as $n_\alpha \mathbf{L}_\alpha + \mathbf{R}_i$ where $n_\alpha = 0, \pm 1 \dots$ and this must also satisfy the potential which should be continuous

$$V(\mathbf{r})=V(\mathbf{r} + \mathbf{L}). \quad (37)$$

With this, the resulting Kohn-Sham orbital becomes a Bloch function of the form

$$\psi_{\lambda\kappa}(\mathbf{r})= e^{i\mathbf{k}\cdot\mathbf{r}} u_{\lambda\kappa}(\mathbf{r}), \quad (38)$$

where $u_{\lambda\kappa}(\mathbf{r})= u_{\lambda\kappa}(\mathbf{r} + \mathbf{L})$ is periodic.

3.17 Mulliken Population Analysis

This involves the separation of electrons of a molecular species in some fractional manner into various constituents (atoms, bonds, orbitals) based on the use of density and overlap matrixes. This is possible because atomic charges or populations are not quantum mechanical observables and thus, such molecular descriptions can result from some reasonable, albeit arbitrary method. However, it is useful for the quantitative description of intra-molecular interaction, chemical reactivity and structural regularities. This can also be used to describe the hybridization of a given state by analyzing the contributions from the atomic orbitals (s-, p- and d- orbitals) and the charge state of an atom. We use it in this thesis as a way to analyse quantitatively the charge redistribution between interacting species such as grapheme and Br₂.

Mulliken [35], therefore, proposed a method that apporitions the electrons of an n-electron molecule into net atomic-orbital type populations and overlap populations given by;

$$\int |\phi_j|^2 dV_j = 1 = C_{1j}^2 + C_{2j}^2 + \dots + C_{bj}^2 + \sum_{r<s} 2C_{rj}C_{sj}S_{rs} \quad (39)$$

where S is the overlap integral, $|\phi_j|^2$ is the probability density associated with an electron.

The sum of contributions over all Kohn-Sham energy levels must add up to one. In this thesis, atomic charge states were obtained by summing Mulliken population analysis for a given atom over all the filled electronic states.

3.18 Summary of the AIMPRO code

AIMPRO stands for ‘‘ab initio Modeling Program’’. It is a quantum mechanical approach that solves the many-body Hamiltonian in the Schrödinger equation via DFT method. It was first developed and written in the United Kingdom, by Bob Jones and Patrick Briddon in

1985. Since then, this has been the code of choice for the atomistic modeling of materials in diverse areas of science spanning from Biology, Chemistry, Physics and other engineering related disciplines due to its robustness coupled with low computing time.

It uses Gaussian centred orbitals in the description of the wavefunctions which is computationally less demanding as compared to other approaches such as plane waves. For instance, in the plane wave formalism, the same expansion is used for analysis over all the components in the cells whilst in AIMPRO only the region containing atoms and electrons are considered in expressions of the Hamiltonian over all space. Recent developments in the AIMPRO code make it easier for example, the optimisation of say 300 atoms in a supercell run which before could take not less than a week to optimise, now could be done within a day by turning on 'filtration' during a run, although this is unfortunately still in final development so could not be used during this thesis.

All the calculations presented in this thesis, were obtained within the AIMPRO code unless otherwise stated in the text, under the local density approximation. The pseudopotential of HGH, was used in the simulation of atoms. The many-electron wavefunction was constructed by the use of atom centred Gaussian basis functions, in which the basis sets are labelled by four orbital sets. The Fermi occupation function, $kT = 0.04\text{eV}$, was used to overcome charge sloshing in systems with partly filled degenerate orbitals or small band gaps. Sampling in the Brillouin zone was done with the Monkhorst-Pack scheme and to satisfy periodic boundary conditions of supercells, the Blochs' approach was used over the lattice vectors. Vibrational modes or stretching frequencies were obtained by calculating the energy second derivatives with respect to the atomic displacement.

Though the Van der Waals correction is not included in this thesis, its usefulness in the description of weakly interacting systems cannot be taken for granted.

3.19 Characterization Techniques

The use of atomistic models is invaluable in the advancement of science. For example where experiment is deemed to be laboriously intensive or dangerous; this can be done with ease, using theoretical calculations. Atomistic modelling allows the prediction of many properties

such as electronic properties of the different carbon allotropes and defect vibration modes, just to mention a few.

The comparison of these theoretical calculations with experimental results will then allow the precise assignment of processes such as stretching modes and other properties in order to give insights into their phenomenon. Here a brief description of the experimental techniques used within this thesis work is given for Raman spectroscopy and Transmission electron microscopy (TEM).

3.19.1 Raman Spectroscopy

Raman spectroscopy is based on inelastic scattering of monochromatic light source upon interaction with a sample in which the photons of the laser are absorbed and re-emitted by the sample.

There are three types of photon scattering in the scattering of monochromatic light source; inelastic, quasi-elastic and elastic scattering. Elastic scattering (Rayleigh) is very strong, with the scattered photons having the same frequency as the incident photon frequency (ν_i). Quasi-elastic scattering is related to the relaxational movements, such the atomic or molecular conformational change, translation and rotation. This is the broadened elastic line with almost zero energy transfer. Inelastic (Raman) scattering is very weak with the scattered photons having a frequency ($\nu_i \pm \nu_s$), where ν_s is the vibrational frequency of the system. Stokes Raman scattering, occurs when the frequency of the scattered photons is lower than the incident frequency, as a result of absorption of the frequency difference of the scattered radiation by the system. And anti-Stokes Raman scattering is observed at higher frequency ($\nu_i + \nu_s$) when the scattered photons has higher energy, which means there is a direct transfer of energy from the system to the photons. The three scattering processes are given in Figure 13. The Stokes scattering is usually stronger than the anti-Stokes scattering, since the intensity of the anti-Stokes scattering is proportional to the number of phonons $n(\nu)$ in thermal equilibrium and that of the Stokes scattering is proportional to $n(\nu) + 1$. Because of this, the Stokes line is normally measured in the Raman spectroscopy. Figure 14, shows the

mechanism of various light scattering processes. A much more detailed description of Raman scattering processes can be found in ref [36].

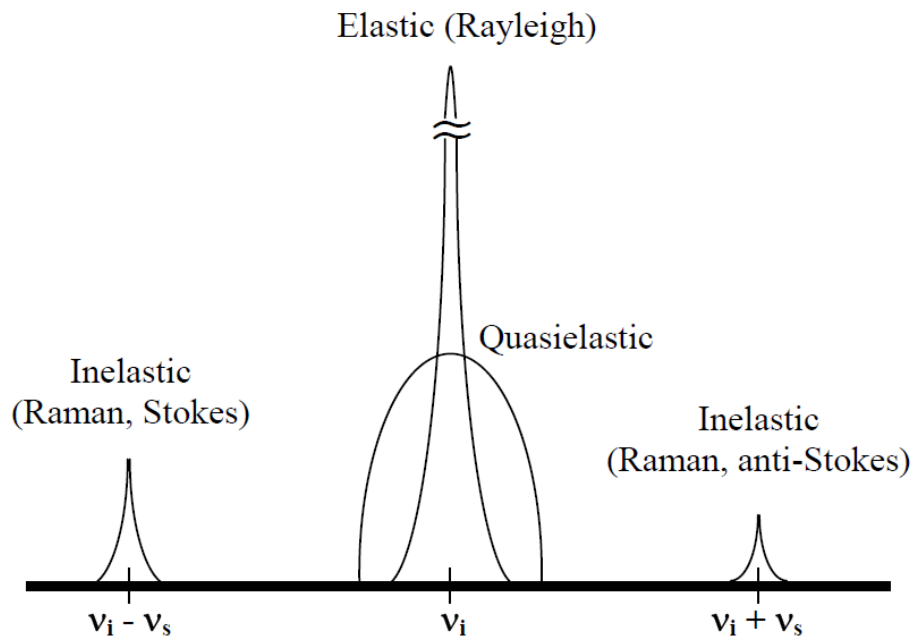


Figure 13. Spectrum of elastic, quasi-elastic and inelastic scatterings [37]

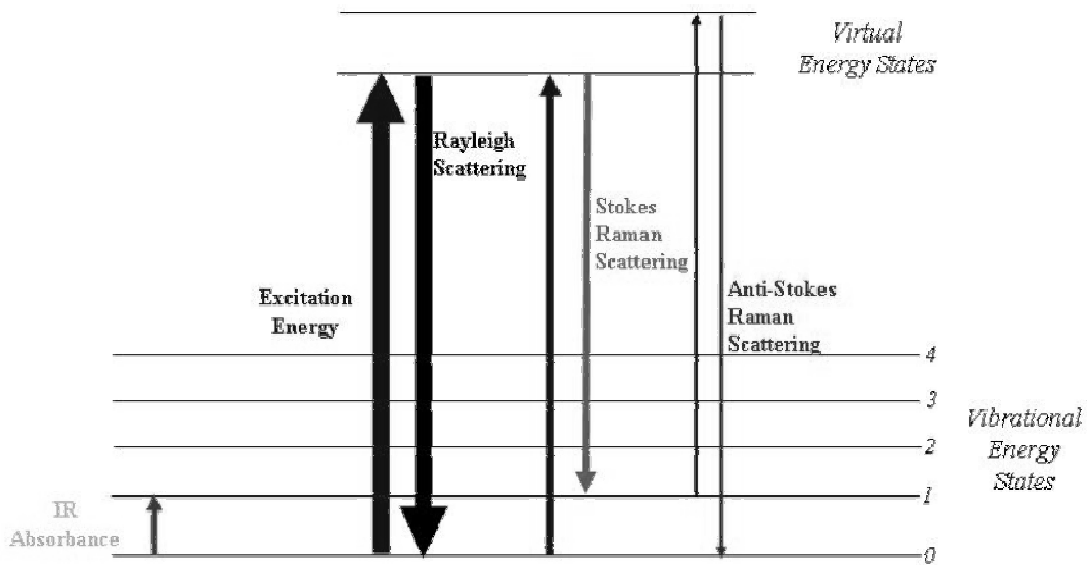


Figure 14. Energy level diagrams for light scattering [37]

The Raman scattering of a species can be observed when the polarizability changes as a result of vibrational motions. The dipole moment induced in a molecule by an electric field is given by

$$\mu = \alpha_0 E_0 \cos(2\pi\nu_0 t) + \frac{1}{2} \left(\frac{d\alpha}{dx} \right)_0 x_0 [\cos(2\pi(\nu_0 + \nu_{\text{vib}})t) + \cos(2\pi(\nu_0 - \nu_{\text{vib}})t)] \quad (40)$$

where α_0 is the Polarizability, E_0 is the vibrational amplitude of the laser, ν_0 is the frequency of the laser, ν_{vib} is the frequency of relevant vibration and $\left(\frac{d\alpha}{dx} \right)_0$ is the variation in polarizability along the displacement led by the vibration. In order for a molecule to be Raman active, $\left(\frac{d\alpha}{dx} \right)_0$ must not be zero, in other words, a change of polarizability is required during vibration. The perturbation of a system under going normal mode vibration could result in the change in polarizability.

The intensities of Stokes (I_S) and anti-Stokes (I_{AS}) lines are,

$$I_S \propto I_i(n(\nu)+1), I_{AS} \propto I_i n(\nu) \quad (41)$$

where n is the temperature Bose factor.

$$n(\nu) = \left(\exp\left(\frac{h\nu}{kT}\right) - 1 \right)^{-1} \quad (42)$$

The sample temperature as a measure of the ratio of the Stokes and anti-Stokes at any vibrational frequency is given as,

$$\frac{I_S}{I_{AS}} \cong \frac{n(\nu)+1}{n(\nu)} = \exp\left(\frac{h\nu}{kT}\right) \quad (43)$$

3.19.2 Transmission Electron Microscopy (TEM)

This is an imaging technique that is widely used for getting information such as structure, crystallography and phase. This can provide a significantly higher resolution than light microscope due small de Broglie wavelengths of electrons. The TEM forms a major tool for the investigation in many scientific fields including physical and biological sciences. This has found application for use in areas such as materials science, cancer research, virology and also semiconductor research. This section is limited to the basics of using TEM, with the view to its use for charactering bromine doped single-walled carbon nanotubes as described in this work. Further detailed information can be obtained in ref. [38]

Image production in TEM is the results of the amplitude difference in the electrons waves reaching the detector or the screen. By the use of a small aperture, between the objective lens

and the detector, only the primary beam contributes to the image. This then culminates into dark and light regions corresponding to areas of the specimen where electrons are scattered strongly and weakly, respectively. In this case, the resolution of the image is controlled by the size of the aperture which then allows more than one beam to the increasing of the resolution.

3.20 References

- [1] D. R. Hartree, *Mathematical Proceedings of the Cambridge Philosophical Society* **24**, 89-110 (1928).
- [2] C. Ewels, *Density Functional Modelling of Point Defects in Semiconductors*, Ph.D Thesis. Exeter, UK. (1997).
- [3] C. Møller and M. S. Plesset, *Phys. Rev.* **46**, 618 (1934).
- [4] W. Kohn, *Reviews of Modern Physics* **71**, 1253–1266 (1999).
- [5] P. Hohenberg and W. Kohn, *Phys. Rev.* **136**, B864 (1964).
- [6] W. Kohn and L. J. Sham, *Phys. Rev.* **140**, A1133 (1965).
- [7] F. Jensen, *Introduction to Computational Chemistry*, 2nd ed. (Wiley cop. New York, 2007).
- [8] R. G. Parr and Y. Weitao, *Density-Functional Theory of Atoms and Molecules* (Oxford University Press, USA, 1994).
- [9] E. Merzbacher, *Quantum Mechanics*, 3rd ed. (Wiley cop. New York, 1998).
- [10] U. von Barth and L. Hedin, *J. Phys. C: Solid State Phys.* **5**, 1629-1642 (1972).
- [11] J. P. Perdew and A. Zunger, *Phys. Rev. B* **23**, 5048 (1981).
- [12] D. M. Ceperley and B. J. Alder, *Phys. Rev. Lett.* **45**, 566 (1980).
- [13] J. P. Perdew and Y. Wang, *Phys. Rev. B* **45**, 13244 (1992).
- [14] S. H. Vosko and L. Wilk, *Phys. Rev. B* **22**, 3812 (1980).
- [15] J. Hafner, *Acta Materialia* **48**, 71-92 (2000).
- [16] R. Telling and M. Heggie, *Philosophical Magazine Letters* **83**, 411-421 (2003).
- [17] F. Tournus and J.-C. Charlier, *Phys. Rev. B* **71**, 165421 (2005).
- [18] J. P. Perdew, K. Burke, and M. Ernzerhof, *Phys. Rev. Lett.* **80**, 891 (1998).
- [19] A. D. Becke, *J. Chem. Phys.* **98**, 1372 (1993).
- [20] P. J. Stephens, F. J. Devlin, C. F. Chabalowski, and M. J. Frisch, *The Journal of Physical Chemistry* **98**, 11623-11627 (1994).
- [21] A. D. Becke, *Phys. Rev. A* **38**, 3098 (1988).
- [22] C. Lee, W. Yang, and R. G. Parr, *Phys. Rev. B* **37**, 785 (1988).
- [23] P. E. Blöchl, *Phys. Rev. B* **50**, 17953 (1994).
- [24] B. Hetényi, F. De Angelis, P. Giannozzi, and R. Car, *J. Chem. Phys.* **115**, 5791 (2001).

- [25] D. A. W. H.E. Schwarz and W.H.E. Schwarz, D. Andraea, S.R. Arnold, J. Heidberg, H. Hellmann jr., J. Hinze, A. Karachalios, M.A. Kovner, P.C. Schmidt, L. Zülicke translated by Mark Smith and W.H.E. Schwarz, *Bunsen - Magazin* 10–21 and 60–70 (1999).
- [26] C. Hartwigsen, S. Goedecker, and J. Hutter, *Phys. Rev. B* **58**, 3641 (1998).
- [27] G. B. Bachelet, D. R. Hamann, and M. Schlüter, *Phys. Rev. B* **26**, 4199 (1982).
- [28] N. Troullier and J. L. Martins, *Phys. Rev. B* **43**, 1993 (1991).
- [29] D. Vanderbilt, *Phys. Rev. B* **41**, 7892 (1990).
- [30] I.-S. Martinez, *Theory of Diffusion and Plasticity in Layered Carbon Materials*, PhD. Thesis, 2007.
- [31] W. Press, *Numerical Recipes in Fortran 77* (Cambridge University Press, Cambridge, UK, 1996).
- [32] E. Polak, *Computational Methods in Optimization: a Unified Approach* (Academic Press, Berkeley, California, 1971).
- [33] R. Jones, J. Goss, C. Ewels, and S. Öberg, *Phys. Rev. B* **50**, 8378 (1994).
- [34] H. J. Monkhorst and J. D. Pack, *Phys. Rev. B* **13**, 5188 (1976).
- [35] R. S. Mulliken, *J. Chem. Phys.* **23**, 1833 (1955).
- [36] N. Colthup, L. Daly, and S. Wilberley, *Introduction to Infrared and Raman Spectroscopy*, 3rd ed. (Academic Press, San Diego, USA, 1990).
- [37] G. Turrell, *Raman Microscopy: Developments and Applications* (Academic Press, 1996).
- [38] D. B. Williams and C. B. Carter, *Transmission Electron Microscopy: a Textbook for Materials Science. Basics* (Springer, 2009).

Chapter 4

Bromination of Carbon Nanomaterials

A variety of exotic properties and potential applications of carbon based materials has triggered an intense research activity since their realization. Analogous to semiconductors, the possibility to dope these carbon materials heavily either by gate voltage or molecular adsorption is of particular interest to applications in electronics and chemical sensors based on these materials.

In this chapter, DFT/LDA calculations and experimental Raman spectroscopy, is used to describe the bromination of graphite, graphene, single walled nanotubes, double-walled nanotubes and the formation of bromide chains. Variations in vibrational modes frequency, bond-length and charge transfer as a result of bromine doping will be discussed. Band structure calculations are included in order to shed light on the changes that occur in these carbon nanostructures as a consequence of bromination.

4.1 Introduction

The doping of carbon nanomaterials with electron donor and acceptors is an active research area which started in 1940 [1] in which much of the efforts were channeled towards the understanding and controlling of electronic properties of graphites and other related carbon structures. Since then graphene and carbon nanotubes have all been doped in this way to tune their electronic properties. Numerous potential applications such as sensors, electronic display panels, hydrogen storage and supercapacitors [2] have been suggested for such materials. Chemical doping is one of the possible ways to tune the electronic properties of these materials for a specific application. Also chemical doping results in Fermi level shift improved dispersion (in the case of bi- or multi-layer substrates) and increase reactivity.

Bromine acts as an acceptor when doped in materials such as graphite, graphene, or nanotubes and has been proposed experimentally as a way to open the band gap in 3- or 4-

layers graphene [3]. Drawing electrons from the host compound drastically modifies the Br₂ molecules characteristic bond-length and stretching frequency [1,2]. Bromine forms many ordered phases and undergoes an order-disorder phase transition as the amount of bromine or temperature changes [4,5].

The layered structure in graphites plays an important role in charge transfer reactions. Acceptor species can intercalate between graphitic layers, expanding the graphite with the resultant hybrids known as graphite intercalation compounds (GIC) [4]. Studies on graphite shows that, the in-plane electrical conductivity of graphite increases from $2.4 \times 10^4 \Omega^{-1} \text{ cm}^{-1}$ at room temperature to $2.5 \times 10^5 \Omega^{-1} \text{ cm}^{-1}$ after intercalation with bromine which can enhance its potential for electrical conductivity-based applications [6]. Furthermore, GICs is a way to make graphene from graphite in combination with other surfactants.

Graphene is a single layer of sp²-coordinated carbon atoms or a monolayer of graphite. It has attracted a lot of interest because of its high carrier mobility and other fascinating physical properties [7], such as abnormal quantum Hall effects and massless Dirac fermions. Furthermore, the high mobility of electrical carriers in graphene makes it useful for a number of carbon-based nanoelectronics devices. In-order to achieve a wider electronic device application such as field effect transistors, there is the need to control the number free electron carriers in graphene with an opened band gap and this could be accomplished by doping with bromine [8].

Single-walled carbon nanotubes (SWCNTs) have attracted a lot of research interest in their high thermal and electronic conductivity, as graphene, there is interest in doping them. One application of SWCNTs is to use them as gas sensors [9]. SWCNTs typically form bundles so once again, their surface and “interior” spaces between these tubes can provide one-dimensional channels for the doping process and the adsorption of dopants in this case is confined as compared to solid surface adsorption.

Double wall nanotubes (DWCNTs) are graphitic carbon structures consisting of two concentric tubes, with diameters and chiral angles similar to SWCNTs [10]. When doped with bromine, it has been proposed as a way to manipulate their electronic properties for applications such as GHz oscillators, cylindrical capacitors and nanocomposites [11]. Recent

experimental studies suggest that, when SWCNTs were doped with bromine, their resistivity and Raman active modes exhibited a stepwise behaviour during the uptake and removal of bromine [12].

Halogen molecules such as Cl_2 , I_2 and Br_2 , are more electronegative than sp^2 - hybridized carbon and they will induce positive doping by charge transfer. However, Br_2 is the only diatomic homopolar halogen that intercalates readily in graphites [7]. Therefore, a much clearer understanding of the behaviour of Br_2 in the doping of carbon nanomaterials is important to explore a new technique of functionalizing carbon nanomaterials.

The bromine molecule has $4s^2 4p^5$ valence electrons and hence the isolated Br_2 molecule has filled p_x and p_y orbitals on both atoms with covalent pp bonding state.

Despite study since 1957, many fundamental questions remain, notably; the amount of charge transfer, bromine vibrational frequency, bromine stable geometry, polybromide chains formation etc. We attempt to address these questions in this chapter.

4.2 Calculation of Bromine interacting with Graphites, Graphene, SWCNTs and DWCNTs

4.2.1 Computational details (AIMPRO)

Optimization of possible structures of bromine molecule interacting with graphite, graphene and SWCNTs were performed using the ab initio density functional code, AIMPRO, within the local density approximation (LDA) by the supercell approach.

Isolated bromine molecule was calculated as a “particle in a box” with a 13.23\AA cubic supercell. Both spin unrestricted and spin average calculations gave net magnetic moments of zero on the bromine isolated molecule.

Hexagonal 4×4 graphene supercells containing C_{32}Br_2 were used with a large vacuum spacing of 31\AA between layers to ensure no inter-layer interaction, and a $4 \times 4 \times 1$ Monkhorst-pack k-point grid [13]. Graphite calculations used $3 \times 3 \times n$ layer supercells $[(\text{C}_{18})_n (\text{Br}_2)_m, n = 1-4, m = 1-2]$ for different layer stackings, corresponding to experimental maximum concentrations, with $4 \times 4 \times 1$ or $4 \times 4 \times 2$ k-point grids depending on the size.

Nanotube calculations were performed using 40 and 80 atom sections of a (5,5) SWCNTs in a hexagonal supercell with Br densities of C₅Br and C₁₀Br respectively and 1 x1x 4 k-point grids. For isolated tube calculations, supercells with 25.39 Å between neighbouring tube surfaces were used and 13.22 Å, along the tube length.

Localised Gaussian basis set were used with a large number of fitting functions per atom (22 for each C atom and 50 for each Br), with angular momenta up to l=2 for C and l=3 for Br. The sampling over the Brillouin zone was performed with weighted summation over wave vectors generated in the Monkhorst Pack scheme. The tolerance in the convergence of self consistency was set as 1x10⁻⁷ eV/atom and a finite temperature electron level filling of kT=0.04eV was used as a computational tool to improve convergence. Core electrons were eliminated using norm-conserving relativistic pseudopotentials of Hartwigsen, Geodecker and Hütter [14], with atomic valence electron configurations of 4s² 4p⁵ for Br and 2s² 2p² for C. Cut-off energy of 150 Hartree was used to obtain convergence of the charge density. Charged systems containing Br₂ cells, were compensated via a uniform background charge in order to maintain overall charge neutrality of the supercell.

All structures were fully geometrically optimised with no constraints of symmetry, allowing both atomic positions and cell dimensions to vary freely. Optimization was considered complete when the total system energy varied by less than 3x10⁻⁶ eV in an iteration. Atomic charge states were obtained by summing Mulliken population analysis over all the filled electronic states. Vibrational frequencies were calculated by determining the energy and forces for ±0.2au displacements of the bromine atoms. The second derivatives on the displaced atoms can then be found from the two-sided difference formula for the second derivative. This approach does not lead to *harmonic* force constants as there are quadratic and higher-order correction terms in these estimates of the second derivatives. We refer to the frequencies arising from these force constants as *quasiharmonic*. If all second derivatives E_{ij} are evaluated then the dynamical matrix can be found directly as E_{ij} / (M_iM_j)^{0.5} where M_i is the mass of the *i*th atom.

We performed test calculations incorporating additionally displacements of neighbouring carbon atoms, but found the difference in calculated Br-Br stretch frequency to be negligible

(*i.e.* the Br-Br stretch is vibrationally decoupled from that of the lattice).

Further discussion of this approach is given in [15], where it was successfully used to identify stretching frequencies of Bromine and Iodine based small molecules.

4.3 Experimental method for the bromination of Single-Walled Carbon Nanotubes

Raw HiPco SWCNTs were purchased from Carbon Nanotechnologies Inc. of Houston, Texas. Liquid Bromine was obtained from Sigma Aldrich Chemicals. In a simple step, 25mg of raw HiPco tubes was mixed with 10ml of Br₂ (l) in a glass ampoule which was capped at the end. We then sonicated the mixture using low-power ultra sonic bath (Fisher Scientific-FB15052) containing ice for 1 hr in order to disperse the nanotubes in the liquid bromine. Another sample was similarly prepared but without sonication (control sample). Both samples were then left for 4 days after which bromine liquid was removed by gradual evaporation in a stream of air for another 4 days.

We then examined the morphology and structure of pristine and brominated SWCNTs using transmission electron microscopy (TEM), using a JEOL-2010 microscope; samples were prepared with Lacey carbon film on a 200 mesh copper grid after dispersing 1mg of tubes in ethanol, this is shown in (Figure 24).

Pristine, liquid bromine and brominated SWCNTs were characterized by Raman spectra in the UV visible range using a Jobin-Yvon T64000 spectrometer equipped with cooled charge detector with scattering excited via Ar⁺ laser ($\lambda = 514\text{nm}$). In the near IR, we used a Fourier transform (FT) Raman spectrometer (Bruker RFS 100) with an excitation given from an Nd: YAG laser ($\lambda = 1064\text{ nm}$). Low laser power of 20mW was used on sample for excitation in the visible range and at 45 mW for the IR excitation: this is to avoid thermal damage due to laser irradiation. A resolution of 4 cm⁻¹ was used in order to discriminate with good accuracy overlapping Raman bands (in order to obtain reasonable signal-to-noise ratios).

4.4 Isolated Bromine Molecule

The Br₂ molecule has been well characterized both experimentally and theoretically. Raman frequency of gaseous bromine has been determined experimentally to be 320cm⁻¹, 309cm⁻¹ for liquid bromine and 295cm⁻¹ for solid molecular bromine [16]. The bond-length of the bromine molecule measured by X-ray diffraction and electron microscopy is reported as 2.283Å [17].

Table 1 below summarizes our calculations of the Br₂ stretching frequency and bond-length using the AIMPRO programme, showing excellent agreement with experiments and other DFT/LDA calculation methods.

	This Work DFT/LDA	Experiment	Literature DFT/LDA
Br-Br bond length (Å)	2.29	2.27 [18]	2.244 [2]
		2.283 [19]	2.263 [17]
Raman Stretch Frequency (cm ⁻¹)	326	323 [18]	324 [2]
		320 [19]	

Table 1 Comparison of bond length (Å) and stretching frequency (cm⁻¹) for isolated Br₂.

The bond length and stretching frequency of Br₂ will vary as a result of charge transfer to the Br₂ molecule when intercalated or absorbed on a donor compound such as graphite or nanotubes. This additional charge occupies the empty ppσ* antibonding state and weakens the Br-Br bond. In order to quantify this effect, a series of geometric optimisations were performed on isolated Br₂ with different charge states, and the resultant bond lengths and vibrational frequencies are given in Figure 15.

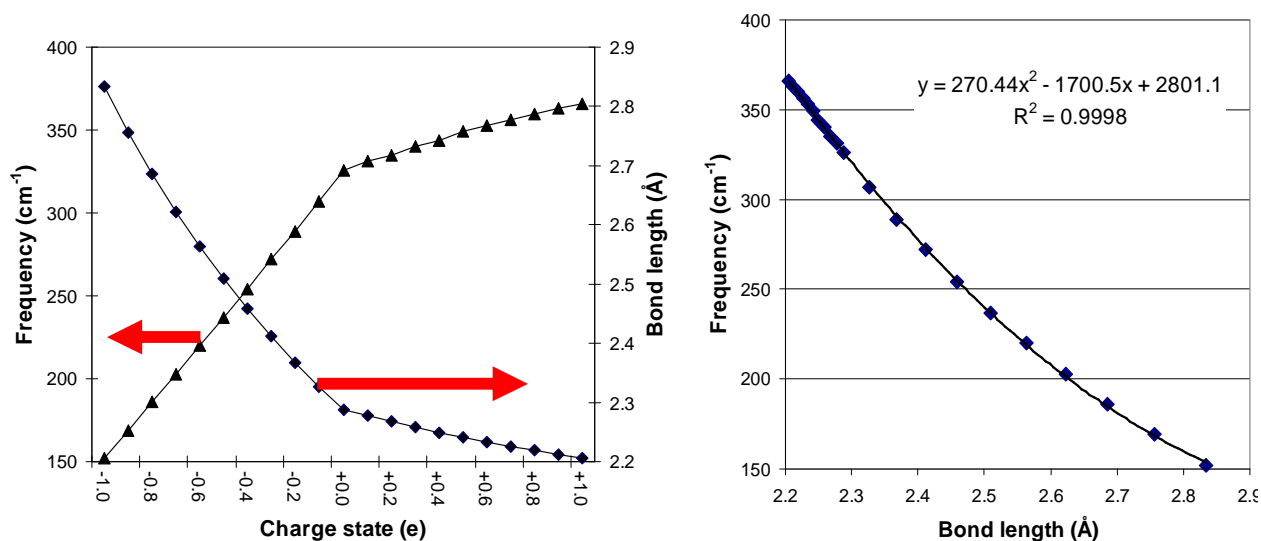


Figure 15 (left) Calculated Br-Br bond length (Å) and vibrational frequency (cm⁻¹) for isolated Br₂ molecule as a function of its charge state, and (right) bond length vs frequency for Br₂ in different charge states.

The bond stretch frequency exhibits two approximately linear regimes as a function of charge state, for the positive and negatively charged molecule respectively. The bond length also shows two regimes, with a slight quadratic dependence. For negatively charged Br₂ (charge state x), Br-Br stretch frequency is given by $\nu = (172.18x + 324.09) \text{ cm}^{-1}$, bond length by $(0.004x^2 - 0.149x + 5.492) \text{ Å}$. For the positively charged molecule these shift to $\nu = (4.0x + 323) \text{ cm}^{-1}$ and length by $(-0.0154x + 4.332) \text{ Å}$. The relationship bond length to frequency is quadratic and is given in Figure 15(right). The Br₂ in graphite typically shows a characteristic peak at 240 cm^{-1} , so these results show that, if this frequency decrease is due purely to charge transfer, it implies a transfer of (0.488 electrons) to each Br₂ molecule. However, to determine if this is the only mechanism involved, it is necessary to model Br₂ in the presence of graphene/graphite, the subject of the following section.

4.5 Adsorption of bromine on Graphene

The ability to modulate band gaps and to n- and p- dope, shifting Fermi level in graphene has spurred intense scientific interest and a lot of methods have been tested to control the electronic behaviour of these novel material, including electrostatic gating [20], use of bilayer graphene [21], graphene-substrate interaction [22], contact with metals [23], and hydrogenation [24]. Being a 2D material, the whole surface of graphene can be used to interact with metal atoms or chemical molecules which may functionalize graphene further with the desirable electronic properties. During chemical absorption, the Fermi level of graphene can be shifted due to charge transfer and the transport of these charge carriers could be controlled accordingly [25]. The introduction of substitutional impurities can disrupt the conjugated network, adsorption-induced chemical doping would be ideal way to manipulate the band structure and control the π -electron conduction of graphene.

Geometrically optimized structures were obtained using the AIMPRO code as described before with the Br_2 molecule placed at parallel and perpendicular configurations at different sites above the carbon atoms, with the concentration modeled, containing C_{32}Br_2 . Figure 16 shows the structures of Br_2 over graphene in both parallel and perpendicular orientation after geometry optimization, with calculated properties for Br_2 perpendicular and Br_2 parallel (structures (a) and (d), respectively, in Figure 16) in Table 2.

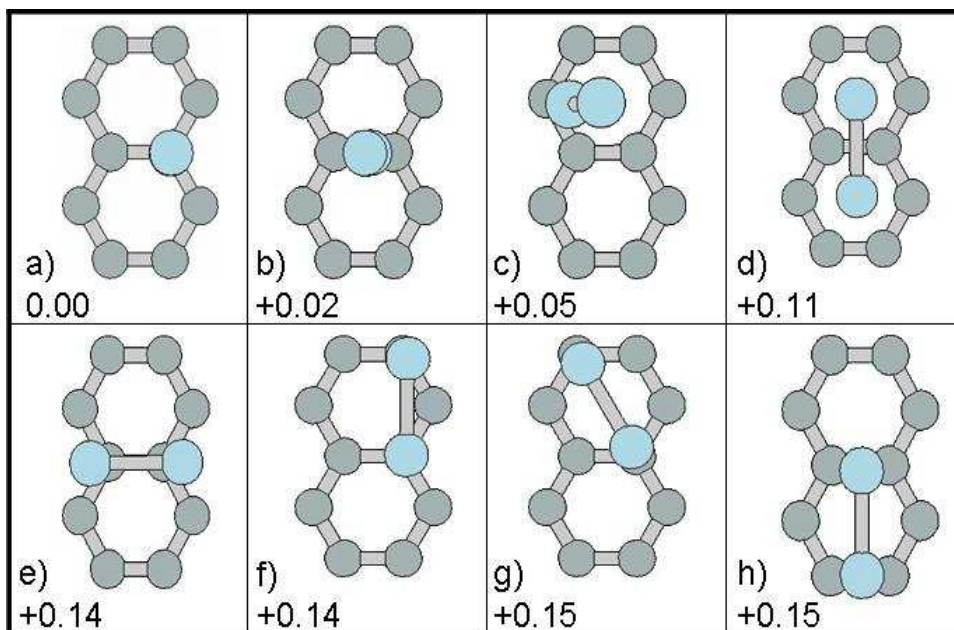


Figure 16. Optimised geometries of Br_2 molecule oriented perpendicular (a-c) and parallel (e-h) to a graphene sheet (C_{32}Br_2), with calculated parameters given in Table 2. Relative stabilities of the different structures are quoted in eV (binding enthalpy of isolated Br_2 to graphene in the most stable structure 'a' is 0.40eV).

The most thermodynamically stable arrangement is Br_2 oriented perpendicular to the graphene sheet above a carbon atom, Figure 16(a). Its binding enthalpy of 0.40 eV shows that it will be strongly physisorbed at room temperature. However, the small variation in binding energy between structures suggests that low density Br_2 binding to graphene will be largely orientation independent; at these densities at room temperature, Br_2 should be in constant tumbling motion. Increasing the Br_2 concentration did not significantly change the relative energies of perpendicular and parallel orientations. However, it is possible to obtain twice the maximum surface density for Br_2 in perpendicular as for Br_2 in parallel orientation [Fig.16(d)]. Thus, for the limit of maximum surface concentration, Br_2 in perpendicular orientation will be expected to dominate.

	Structure								Literature DFT/LDA [2]
	a	b	c	d	e	f	g	h	/VdW- DFT [26]
Orientation with respect to graphene surface	Perpendicular				Parallel				Parallel
Binding energy / Br ₂ (eV)	-0.40	-0.38	-0.35	-0.29	-0.26	-0.26	-0.25	-0.25	-0.20 [2] -0.29 [26]
Br-Br Stretch Freq. (cm ⁻¹)	288	290	289	270	267	269	265	269	311 [2]
Br-Br bond length (Å)	2.33	2.32	2.32	2.31	2.31	2.31	2.31	2.31	2.245 [2]
Br-C distance (Å)	2.74	2.82	2.85	3.45	3.37	3.35	3.35	3.45	3.375 [2] 3.74 [26]
Charge state / each Br (e)	+0.48 -0.61	+0.47 -0.60	+0.48 -0.62	-0.04 -0.04	-0.04 -0.04	-0.04 -0.04	-0.04 -0.04	-0.04 -0.04	-
Total Charge transfer / Br ₂ (e)	-0.13	-0.13	-0.14	-0.08	-0.08	-0.08	-0.08	-0.08	-

Table 2 Calculated parameters for Br₂ oriented in different configuration on graphene compared with other DFT calculations from literature at concentration C₃₂Br₂. [Structures for calculated parameters are shown in Figure 16].

4.6 Br₂ perpendicular to graphene surface

The most stable configuration represents a very unusual configuration for bromine. It shows strong charge transfer (0.129e) from graphene, with a very strong induced molecular dipole (Br^{+0.480} – Br^{-0.609}). The singly occupied p_z orbital of the lower Br atom depopulates into the p_z of the upper Br atom, forming a nascent bromonium and bromide ion pair. In this way, the emptied lower p_z orbital can sit within the graphene π cloud (Br is only 2.74 Å above the graphene), this is shown schematically in Figure 17.

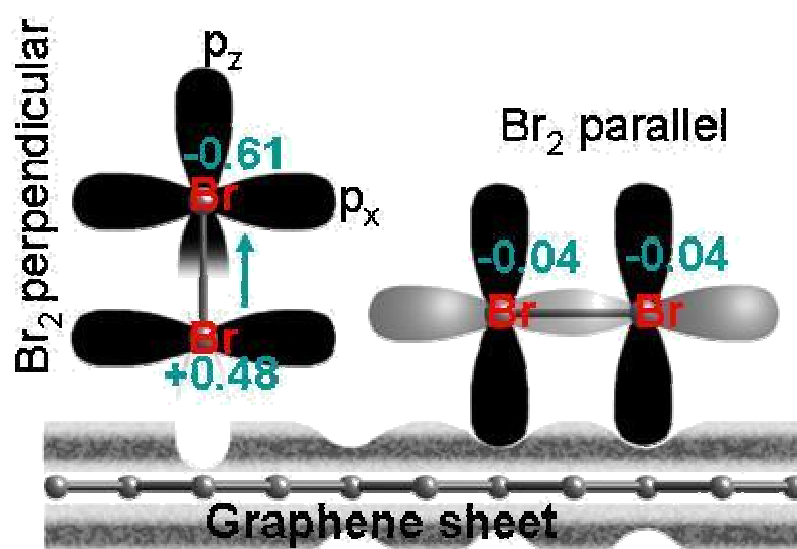


Figure 17 Schematic of orbital filling of (left) Br₂ perpendicular and (right) Br₂ parallel on graphene with charged state marked in green. Filled p-orbitals are black, partially filled gray and empty white. The graphitic π-cloud is represented shaded. Note that Br₂ perpendicular sits above a carbon atom whereas Br₂ parallel sits above hexagon centres. [Thanks to J.-C. Riquier for graphical help with image].

This behaviour is reminiscent of the well-known reaction between Br₂ and unsaturated bonds in organic chemistry. However, in these cases, this dipolar form of Br₂ is an unstable transient state that immediately saturates the C=C bond, forming Br-C bonds. In graphene, this final step would be endothermic due to steric hindrance between the Br atoms as a result of the mechanical confinement of the lattice. Indeed, attempt to stabilize C-Br pairs on graphene in both neighboring (1,2) and cross-hexagon (1,4) configurations both resulted in

Br spontaneously restructuring into a Br₂ molecules (placing Br-C in a (1,4) configuration with Br atoms on opposite sides of the graphene is 1.68 eV less stable than Br₂ in perpendicular conformation).

The unusual Br₂ perpendicular configuration is reflected in the band structure (Figure 18 (a)). The strong coupling between the graphene lowest unoccupied molecular orbital (LUMO) and Br₂ antibonding state at around +0.6 eV reflects the interaction between the empty p_z orbital and the graphene π cloud, with the resultant low-density Br₂ layer opening a small 86 meV band gap. This therefore, represents a new form of Br₂ not previously reported in the literature and discovered in this PhD thesis.

4.7 Br₂ parallel to graphene surface

In contrast, Br₂ in parallel orientation has no induced dipole, with a much weaker charge transfer (0.084e) from the graphene. The molecule sits 3.254 Å (which is higher than Br₂ oriented perpendicular on graphene considered before) above the graphene, i.e., above the π cloud, with the additional charge occupying the Br₂ *pp σ ** antibonding state. The band structure (Fig.18 (b)) shows that the Br₂ states lie lower than those of Br₂ in perpendicular orientation by ~0.7 eV. The Br₂ antibonding state pins the Fermi level ~0.2 eV lower than in the pristine case, leaving graphene states around the K-point depopulated, indicating charge transfer from graphene to Br₂. The bromine states are flat and largely decoupled from the graphene bands since there is only weak interaction between Br₂ orbitals and the graphene π cloud in this orientation.

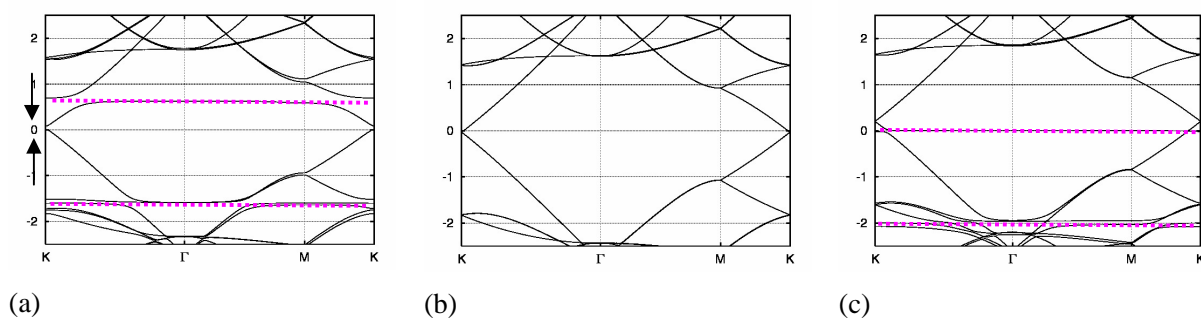


Figure 18. Band structure of (a) Br_2 perpendicular and (c) Br_2 parallel on graphene (eV); (b) same supercell of pristine graphene for comparison. Dotted pink show bromine states and arrow pointing to a band gap opening (86meV) around Fermi level in the Br_2 perpendicular case (a)

4.8 Spectroscopy of bromine on graphene

The results of our theoretical studies above are consistent with Raman observations of brominated graphene [3]. For graphene with three or more layers, a resonant Raman signal was observed for bromine around 240 cm^{-1} ; for monolayer and bilayer graphene, no signal was observed. This could be an orientation effect, since if the Br_2 sits perpendicular to the surface and conventional orthogonal Raman is used, then the molecules will be aligned with the beam and there will be no interaction and, hence, no signal. This would suggest Br_2 is orthogonal to the surface in mono- & bi- layer, and parallel in higher order, consistent with our calculations (see next section). In addition, the bromine highest occupied molecular orbitals (HOMO) and LUMO states are further apart for the Br_2 perpendicular ($\sim 2.2 \text{ eV}$) than for the Br_2 parallel ($\sim 1.96 \text{ eV}$) or for the various graphite structures examined below (1.7-2.0 eV). Given the excitation laser used (633 nm, 1.96 eV), Br_2 perpendicular would have an associated resonant Raman signal, and, since none is observed, this allows to exclude this configuration. However, the perpendicular configuration at 2.2 eV sits above the laser excitation energy and so would not be in resonance, which may also explain the lack of signal since non-resonant Raman is typically 10^6 times weaker signal.

It would be interesting to test, especially as graphene and Br₂ are IR-inactive, so the signal should be clear. Clearly, the strong dipole shows that, the simple first approximation in section 4.7 that the Raman shift is purely due to charge transfer is unlikely to be correct.

4.9 Graphite

Graphite, one of the allotropes of carbon, is a semimetal with nearly compensated low density electrons and holes, and a very small effective mass [27]. Also, it is known to be anisotropic, being a good electrical and thermal conductor within the layers (mainly associated with the in-plane bonding) and a poor electrical and thermal conductor perpendicular to the layers (due to weak interlayer interactions). Electrical conductivity enables graphite to be used as electrochemical electrodes and as electric brushes. Owing to this anisotropic behaviour, the carbon layers in graphite can slide with respect to one another quite easily, thus making graphite a good lubricant and pencil material.

The intraplanar bonding is covalent as a result of sp² hybridization which gives resonant honeycomb structures with C-C bonds of 1.42 Å [28]. The interlayer distance is typically known to be 3.34 Å in AB stacked graphite.

Interlayer interactions became a subject of controversy, initially thought of as purely due to Van der Waals interactions, (or more precisely, dispersion forces). Calculations have suggested that these forces are less important, and that the bonding can be explained mainly through a weak bonding overlap of π-electron system of each carbon layer [29].

Bernal stacked hexagonal graphite is the most stable form of graphite. In this phase, the layer stacking is AB. Other stacking arrangements are also known to exist such as rhombohedral or ABC and AA stackings, shown in Figure 19.

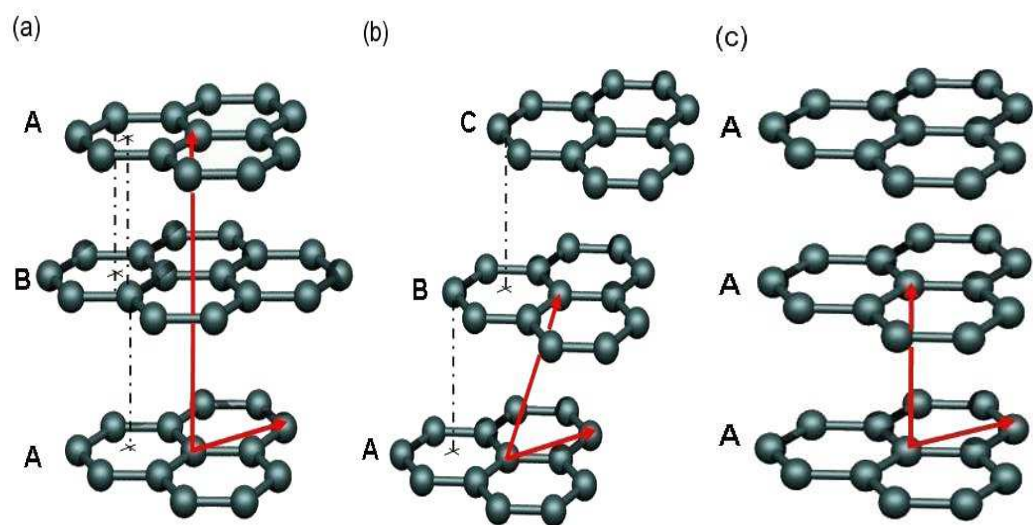


Figure 19. Types of stacking in graphite. (a) AB stacking or Bernal graphite, (b) ABC stacking or rhombohedral graphite and (c) AA stacking. Lattice parameters for the primitive unit cell are shown in red for each case (Image from Ref. [27]).

	Electron affinity, E_a (eV)	Ionization energy, E_i (eV)
Graphite	4.8	4.4
C_{60}	2.8	6.8

Table 3. Comparison of electron affinity E_a and Ionization energy E_i of graphite with C_{60} showing their acceptor rather than donors character (From Ref. [32]).

Next, we modeled graphites and our calculated energy to separate AB graphite layers with no Br present was found to be 36.7 meV/atom, with AA-stacked graphite 12.0 meV/atom less stable than AB-stacked graphite. The figures are in good agreement with experiment (35 meV/atom) [30] and previous calculations (9.68-9.70 meV/atom AA-AB energy difference) [29,31]. The interlayer spacing of 3.39 and 3.50 Å for AB- and AA-stacked graphites respectively are also in reasonable agreement with previous calculations [29].

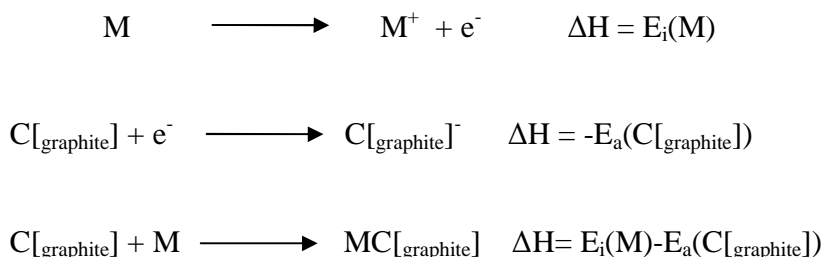
4.9.1 Graphite intercalation compounds.

Graphite intercalation compounds (GICs) are formed by the total or partial equilibrium through the insertion of chemical reactants (called intercalates) between the layers of the graphite host material. These are known as intercalation reactions and were first synthesized (1841 by Schaffautl) with systematic studies on their physical properties by the use of X-ray diffraction for stage index determinations [1] (staging discussed later).

Intercalation compounds occur in highly anisotropic layered structures in which the *intraplanar* binding energies are large in comparison with the *interplanar* binding energies. Amongst the carbon allotropes, diamond is the only crystalline variety of carbon which does not form intercalation compounds due to its 3D rigid structures (sp^3 hybridization). On the contrary, in graphite and other carbon materials such as fullerenes, the crystal structures are held together by weak interactive forces, and intercalation which results in the expansion of the structure, is extremely easy since the energies involved are relatively small.

The amphoteric nature of graphite makes it possible to accept electrons from electropositive donor species (such as K, Rb, Cs) or donate electrons to electronegative acceptor species (such as Br, Cl, F), as a result increasing the number of carriers in the conduction and valence bands accordingly and making it act as a 'synthetic metal'.

The mechanism for alkali metals intercalating in graphite can be described by the hypothetical reaction below:



Where M is the alkali metal, ΔH is the enthalpy of the reaction, E_i is ionization energy and E_a is electron affinity.

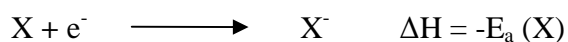
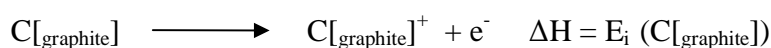
Intercalation into graphite is governed for the alkali metals by their ionization energy. Thus, the higher the ionization energy of a metal, the more difficult to form a GIC and the reverse is true for lower ionization alkali metal, this is given in Table 4

Alkali metals	E_i (eV)	ΔH (eV)
Na	5.14	0.34
Li	5.39	0.59
K	4.34	-0.46

Table 4 Ionization energy of the alkali metals with the values of ΔH calculated by the expression $\Delta H = E_i(M) - E_a(C_{[graphite]})$ (adapted from Ref [32]).

From Table 4, it follows that intercalation compounds of potassium will be easier to form, whereas those of sodium and lithium will be difficult due to the endothermic nature of their reactions.

Similarly, the assessment of donor characteristics of graphite can be performed by combining the first ionization energies with the electron affinity of the acceptor elements (halogens):



Where: X represents a Halogen atom

For the halogen elements, intercalation into graphite follows a different trend which is not well understood, thus, from Table 5 below, one might be tempted to say, since the ΔH value for Cl_2 is lower than the rest it should intercalate more easily but this is not the case. It has

been suggested rather that, Br₂, IBr and ICl halogens intercalate readily due to their intermolecular distances (2.28, 2.49 and 2.40 Å respectively) which are closer to the distances between the graphite hexagons, whose centres are separated by 2.46 Å [6]. For instance, Cl₂ which is much smaller (2.02 Å) and I₂ which is much larger (2.68 Å) do not intercalate in graphites and as a result the graphite-Br₂ system is the most studied the best understood of the molecular intercalation compounds.

Halogen	E _a (eV)	ΔH (eV)
F	3.40	1.00
Cl	3.61	0.79
Br	3.37	1.03
I	3.06	1.34

Table 5. Electron affinity E_a(X) of the halogen and values for the expression E_i(C_[graphite])-E_a(X) (adpted from Ref.[32]).

Perhaps the most important and characteristic ordering property of graphite intercalation compounds is the phenomenon known as staging, which is determined by intercalate layers that form an order sequence along the perpendicular plane of the graphite layers. The GICs are thus classified by a stage index (n) symbolizing the number of graphite layers between adjacent intercalate layers as in Figure 20. The phenomenon of *staging*, is a general process occurring in graphite intercalation compounds, even in samples with very dilute amount of intercalates concentration [1]. The graphite-Br₂ system does not form *stage-1* compounds [33], however, the halogen ICl does form a *stage-1* compounds, (see Figure 20).

Charge transfer, which occurs in GICs, results in the modification of chemical or physical properties of the intercalation compound and as such these compounds are more electrically conductive than graphite on its own.

The high conductivity of GICs has found application as electromagnetic interference (EMI) shielding [34]. Many of the GICs can be exfoliated upon heating, thus providing a means of graphene formation from graphite. Compressing exfoliated graphite flakes without a binder

leads to mechanical interlocking, hence forming a flexible and resilient sheet known as flexible graphite. At present, the interest on these GICs is for secondary batteries applications [32].

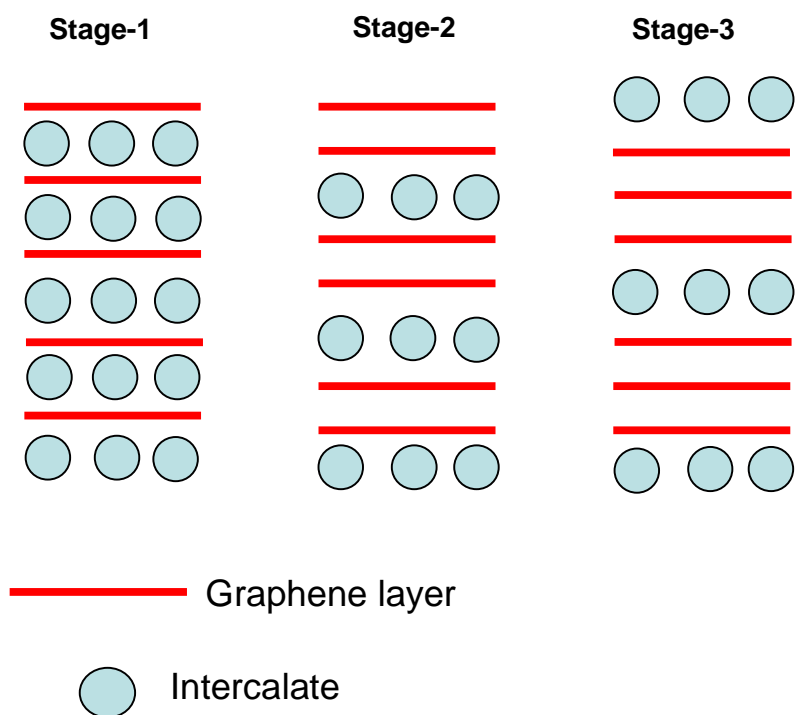


Figure 20 Rudorff model of staging in graphite intercalation compounds [35].

4.9.2 Br₂ Intercalated graphite

Bromine is known to form several transitional phases within graphite which depend on bromine concentration and temperature. Low-energy electron diffraction (LEED) studies [36] show for low coverage of 0.2 bromine atom monolayer at room temperature, five distinct phases: a lattice gas, a liquid, a first and second solid phase, followed by a multilayer or bulk solid phase. The same study suggested bromine molecules become atomic sitting on the

graphite layers. Heald and Stern [37], used Extended X-ray Absorption Fine Structure (EXAFS) spectroscopy at room temperature and 100K to study the Br-Br intramolecular distances and Br-C nearest neighbour distances using bromine gas and CBr_4 as control samples. They found that bromine molecules intercalated at coverages between 0.6 and 0.9 monolayers lie parallel to the basal plane, with an expansion of the Br-Br distance from 2.283Å in the free molecule to 2.31Å with a net charge transfer from the graphite of 0.16e/ Br_2 molecule. The increment of 0.03Å was explained by the need to accommodate the lattice mismatch between the free bromine molecule and the 2.46Å spacing between graphite hexagons. Eeles and Turnbull [17] used X-ray diffraction and electron microscopy to study Br_2 intercalated graphite. They suggested that the intercalated Br_2 at lower concentration is composed of chains of Br_2 molecules in which the intermolecular distances are identical to that of solid bromine.

Graphite Raman spectra associated with Br_2 intercalation shows a strong peak at 242 cm^{-1} [38], assigned to the intercalated Br_2 stretch mode. The frequency is downshifted from 320 cm^{-1} for gaseous Br_2 and 295 cm^{-1} for solid molecular bromine [16]. Raman spectroscopy has proved to be indispensable for characterizing graphite intercalated compounds, giving detailed information regarding the layering type in GICs.

Using AIMPRO (DFT/LDA), a range of different bromine intercalated graphite structures were optimised containing C_{18}Br_2 and C_{36}Br_2 which are (stage-1) and (stage-2) compound respectively, where Br_2 molecules are intercalated between each layer (stage-1) or alternate layers (stage-2) of graphite. The molecules were placed either perpendicular or parallel to the graphite sheets, in a variety of different orientations and locations including above α - and β -carbon atom sites, and above hexagon centers. The energy to separate isolated AA- and AB-stacked graphites was calculated (given in section 4.9 above) together with other different configurations and concentrations of bromine in graphites.

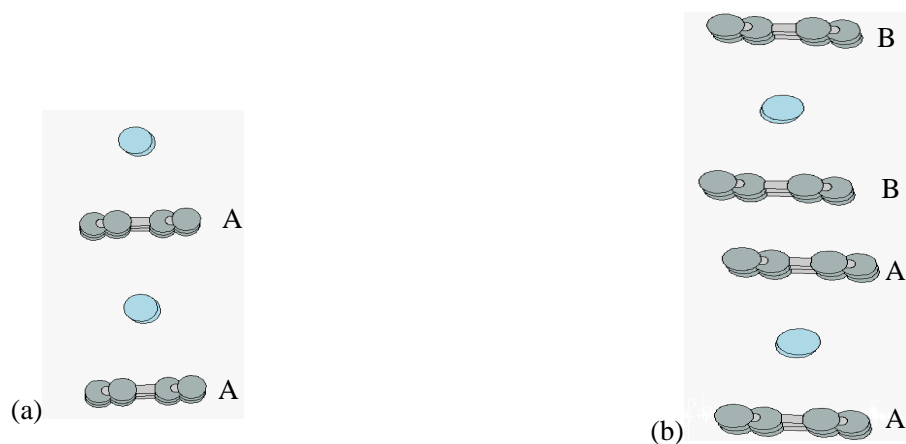


Figure 21. Optimized absorption geometry of Br₂ molecules on (a) stage-1 AA-graphite (C₁₈Br₂) and (b) stage-2 AABBB-graphite (C₇₂Br₄).

Unlike in graphene, Br₂ in graphite is more stable parallel to the graphitic layers after geometry optimization, with Br atoms above hexagon centers (see Figure 21), in good agreement with experiments [17,37]. The perpendicular Br₂ intercalated graphite structures are much less stable (by typically 0.52 eV). The results are summarized and compared with experiments in Table 6. While the majority of agreement is excellent, there is an inconsistency with the charge transfer measurement extracted from Raman. However as the authors themselves observed [19], there is a large potential error in this experimental value.

(a)

	Binding Energy / Br2 (eV)	Br-C distance (Å)	C- C interlayer distance (Å)	c-axis (Å)	Br-Br bond length (Å)	Br-Br frequency (cm-1)	Charge Transfer (e)
Stage 1							
[AX]n (C ₁₈ Br ₂)	+0.040	3.51	6.45	9.80	2.30	287	-0.16
[AXBX]n (C ₃₆ Br ₄)	+0.059	3.47	6.62	9.98	2.33	286	-0.18
Stage 2							
[AXABXB]n (C ₇₂ Br ₄)	+0.040	3.46	6.47	9.82	2.30	274	-0.12
[AXB]n (C ₃₆ Br ₂)	+0.054	3.51	6.61	9.96	2.30	264	-0.17
[AXA]n (C ₃₆ Br ₂)	+0.167	3.51	6.57	9.92	2.31	250	-0.15

(b)

	Stage-1	Stage-2	Experiments
Cell used	C ₁₈ Br ₂	C ₇₂ Br ₄	
Binding energy {Br2 (eV)}	+0.04	+0.04	
C-C layer distance(Å)	6.45	6.47	7.0 [33,38] , 7.05 [35]
c axis (Å)	9.80	9.82	10.7 [17]
Br-Br bondlength (Å)	2.30	2.30	2.34 [37-39]
Br-C distance (Å)	3.51	3.46	2.9 [39]
Br-Br frequency (cm ⁻¹)	287	274	242-258 [18,19]
Charge transfer {Br ₂ (e)}	-0.10	-0.12	-0.16 [37] -0.34 [19]

Table 6 (a) Calculated different stacking arrangements for Br₂ intercalated in graphite at low coverage of Br₂ concentration for (stage-1) and (stage-2) GICs, and (b) Comparison of calculated and experimental results for Br₂ intercalated graphite, where the C-C layer distance refers to the layers separated by bromine. Experimental values are from EXAFS [39], Raman [18,19] and XRD [17,19,33,35]. Note that at these low concentrations, Br₂ intercalation is *endothermic*.

Aside from other lowest energy structures, other metastable structures were obtained. While their energies were all within 0.01-0.05 eV of the lowest energy structures quoted in Table 6b, they show significant variation in the Br₂ stretching frequency (250-286 cm⁻¹) and also slight variation in position and Br-Br bond length (2.31-2.33 Å). This then suggests that, at room temperature, Br₂ in graphite will be mobile and is consistent with the observation of a broad and somewhat complicated Raman peak [18].

Our calculation for isolated Br₂ with the same charge state (-0.16) (see section 4.4) as the intercalated species gave the same Br-Br stretching frequency. Thus, one could conclude that in this case, the drop in Br-Br stretch frequency as compared to gas phase Br₂ is wholly due to charge transfer from the surrounding graphite. In addition, a calculation incorporating the energetic double derivatives of the surrounding carbon atoms was performed, but the frequencies remained the same to within 1cm⁻¹, showing that the Br₂ stretch mode is decoupled from the surrounding carbon lattice consistent with the literature [2].

All possible layer stacking combinations for *stage-1* and *stage-2* Br₂ intercalated graphite were explored. Whilst it is known that, unbrominated graphite prefers to be AB-stacked, in the presence of Br₂ this switches to AA-stacking, with bromine on each side. Thus (indicating layers of bromine molecules by (X), this gives the most stable stage-1 phase to be {[AX]_n} and stage-2 phase to be {[AXABXB]_n}, and presumably by extension {[AXAB]_n} and [AXABABXBAB]_n} for stage-3 and stage-4 respectively.

At these low densities, the binding energy for bromine molecules intercalated in graphite is endothermic (albeit very weakly so). This means that there is an energetic cost associated with separating the graphites planes (a cost per unit area) and at low Br₂ density or concentration, the energetic cost involved with separating the graphitic planes is not sufficiently offset by the binding of the Br₂ to the layers. Subtracting our calculated energy to

separate graphite layers from the Br_2 intercalation energy gives energy for intercalation of Br_2 into pre-separated stage-1 graphite of 0.581 eV/ Br_2 . This implies that the minimum Br_2 concentration for exothermic intercalation in stage-n graphite will be $\text{C}_{16n}\text{Br}_2$. Indeed, a fixed-Br calculation for a C_8Br_2 stage-1 high coverage structure gives Br_2 intercalation as exothermic. Thus, Br_2 will aggregate in the same interlayer space and should be considered as a layer rather than as individual molecules.

This minimum required concentration suggests unusual diffusion behaviour during intercalation, since classic Fick's law diffusion has a continuous concentration gradient at the diffusion front. However in the case of Bromine, the minimum concentration required for thermodynamic stability would indicate a much slower diffusion process with an abrupt diffusion front. This is consistent with the long intercalation times required experimentally [40], despite the high bromine inter-layer mobility that had been calculated. It also explains why, on out-gassing bromine, the material switches from stage-2 to a compound of stage-n ($n = 3, 4, \dots$) rather than remaining at stage-2 with lower bromine density per layer.

Figure 22 a-c, and b-d shows, respectively, the electronic band structures of pristine stage-1, stage-2 graphites and stage-1, stage-2, with intercalated Br_2 . Due to band folding the point, where the π and π^* bonding and antibonding levels of graphite meet occurs at the Γ point. Comparison of the two Br_2 intercalated graphitic band structures (b-d) shows that the Fermi level is shifted to lie below the level crossing point, and a new filled flat band appears in the vicinity of Γ (~ 0.29 eV) then falls off at M (~ -0.1 eV), which is due to the Br_2 states in the stage-1 graphite.

A similar trend is observed for the stage-2 graphite where there is a shift in the Fermi level below the level crossing point, with a filled state at about (0.45 eV) at Γ which does not fall below the Fermi level at M unlike in the stage-1. This could explain the instability in stage-1 compounds bromine compounds observed experimentally. This state also shows some dispersion signifying weak coupling with the underlying graphite. In other respects, the graphite band structures are barely perturbed.

In all cases, there is a down shift in the Fermi level on introduction of Br₂ showing charge transfer from the graphite to the Bromine molecules.

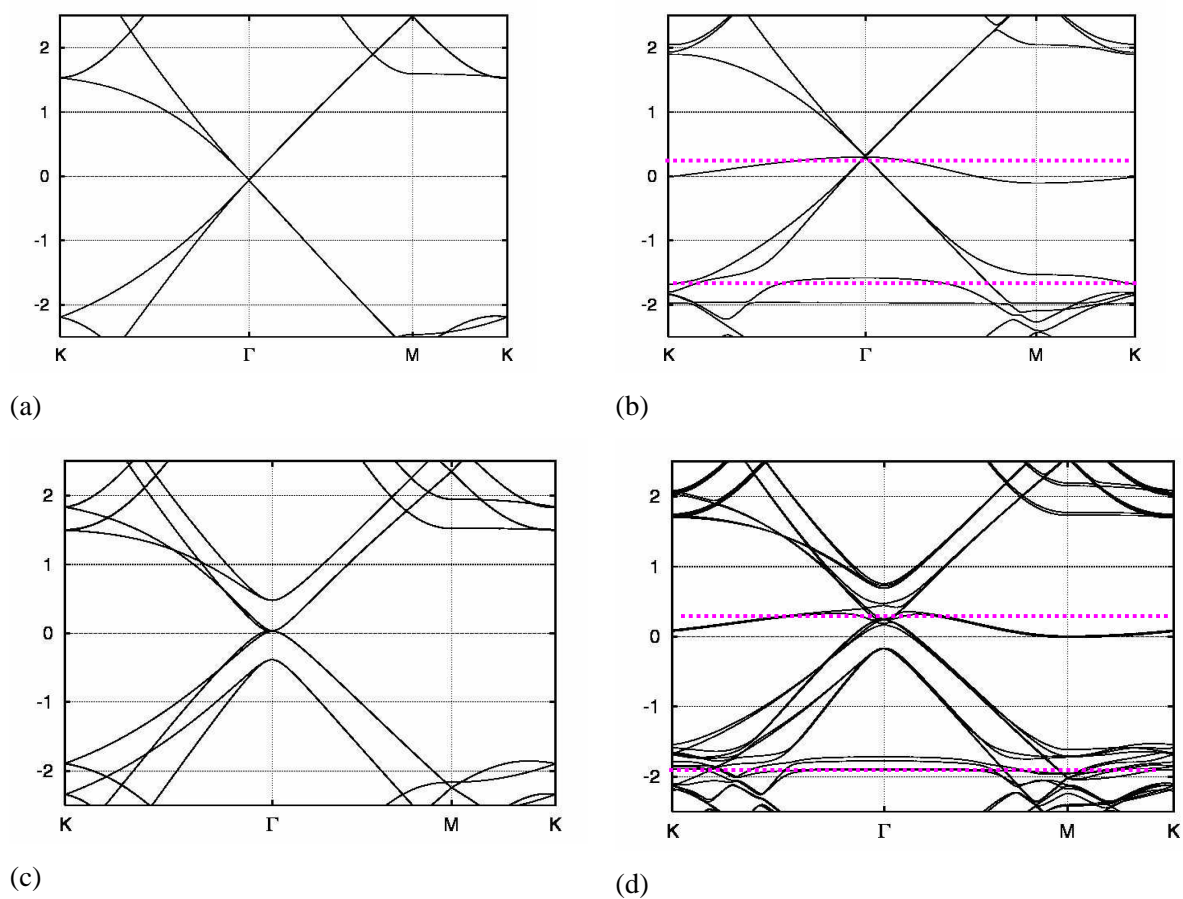


Figure 22 Band structures for stage-1 AA-graphite (C₁₈Br₂) with (a) pure AA-graphite (b) Br₂ doped AA-graphite and stage-2 AABB-graphite (C₇₂Br₄) with (c) pure AABB-graphite (d) Br₂ doped AABB-graphite. Dotted pink lines are guide to the eye showing the bromine states.

4.10 Br₂ doped Single-walled Carbon Nanotubes (SWCNTs)

The physical properties of single-walled carbon nanotubes (SWCNTs) doped with bromine show large differences with respect to the undoped pristine materials. Since SWCNTs are

normally present in bundles, the long length and cylindrical geometry of the nanotube can provide a way of confining the dopant within the nanotube environments (see Figure 23). The interstitial spaces within nanotube bundles provide one-dimensional channels for the incorporation of dopants and the adsorption of dopants into this site should be constrained in comparison to adsorption in a two-dimensional material. Therefore the electrical properties of these doped nanotubes can change in unusual manners as the dopant is absorbed on the surface and the interstitial spaces of the tube bundles.



Figure 23 SWCNTs bundle showing specific interstitial spaces for Br intercalations (image taken from Ref. [40])

Iodine, which has the same valence electrons as bromine, is reported to form chains inside SWCNTs by inducing a zipper-like effect as the concentration of iodine changes [41]. Bromine doped nanotubes exhibit drastic change in vibrational and electronic properties but their structure is not yet clear.

The Raman spectra for pristine SWCNTs contain several finger print modes, notably the tangential G mode seen at 1590 cm^{-1} which are related to the E_{g2} graphite mode, the D mode at 1300 cm^{-1} which is associated with disorder or other amorphous structures present in the nanotubes, and the radial breathing modes (RBMs) in the low frequency regime (the values of RBMs depend on the diameter of the tube).

Raman modes of bromine doped nanotube shows a stepwise behaviour after doping and removal of bromine. Evidently, a mode has been seen near 240 cm^{-1} for Br_2 -doped SWCNTs

with excitation energy higher than 1.8 eV and was tentatively assigned to the breathing mode of Br₂-doping of nanotube bundles [42].

We next prepared brominated samples of SWCNTs and took Raman spectra with laser energy of (514nm and 1064nm). The full Raman spectra at RT for pristine HiPco SWCNTs sample in the solid state, liquid bromine and that of brominated HiPco tubes together with TEM image of the brominated tubes in the range 0-500 cm⁻¹ are shown in Figure 24.

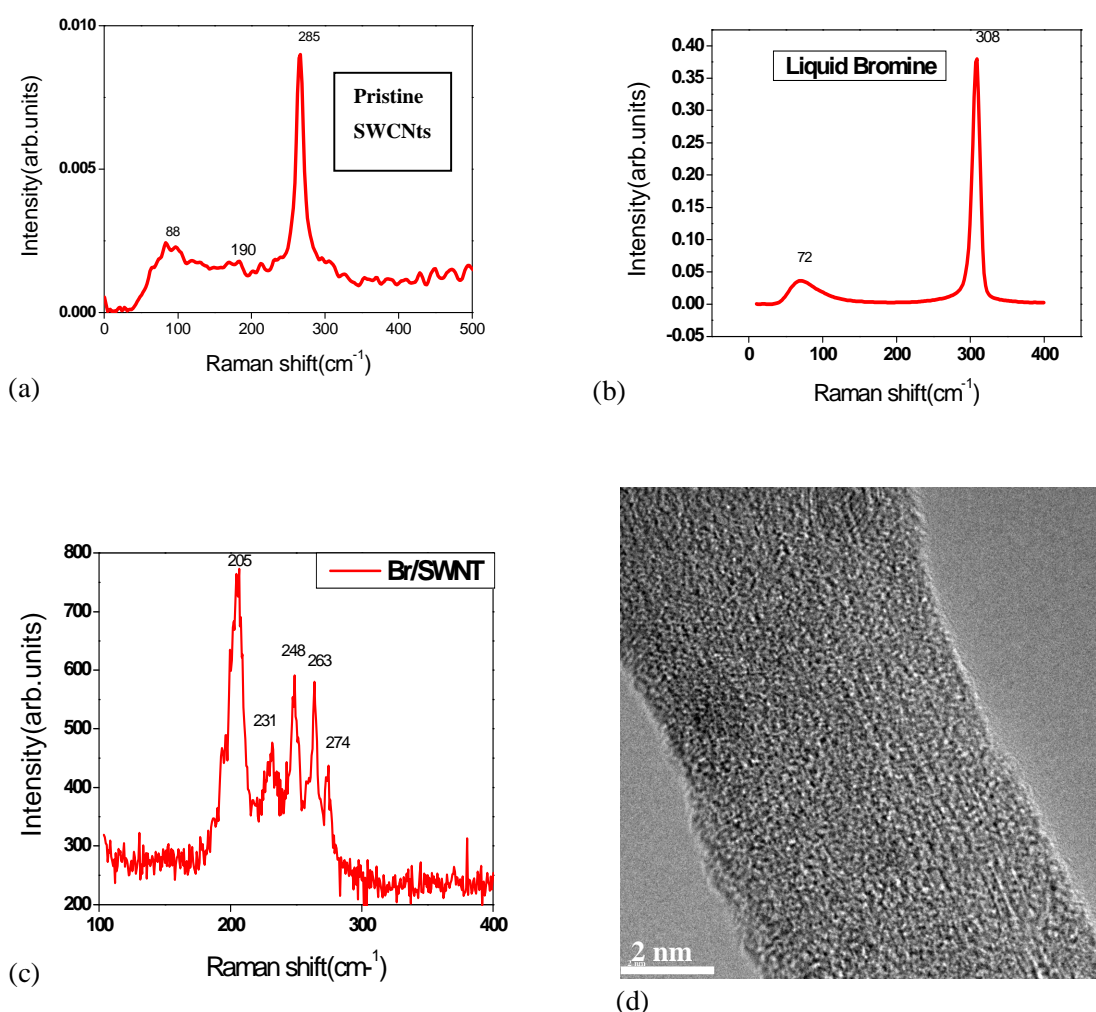


Figure 24 Our experimental Raman spectra (a) pure SWCNTs, (b) liquid bromine, (c) Br/SWCNTs respectively and TEM image of (d) Br/SWCNTs bundles. (a) and (b) performed with FT-Raman at 1064 nm, (c) by UV Raman at 514 nm.

No signal was observed for the brominated sample with the 1064 nm laser.

The strong signal at 308 cm^{-1} in Figure 24b is due to the symmetrical Br-Br stretching mode of the liquid bromine solvent, in good agreement with literature value of 308 cm^{-1} [43]. As earlier indicated, the RBM and the G-mode are both sensitive to bromine doping but here only the RBM region is investigated. For the pristine tubes, Figure 24a, two frequency modes are seen (190 and 285 cm^{-1}), identifying the diameter range as corresponding to HiPco tubes (0.8 - 1.3nm). Both FT-Raman spectra exhibit a peak at $\sim 80\text{cm}^{-1}$ (72 and 88 cm^{-1} respectively) corresponding to the notch filter of the spectrometer.

The spectrum taken at 514nm after bromination shows other frequency modes in the RBM region between (205 - 274 cm^{-1}). These can be ascribed to the bromine stretch mode and other different chirality tubes in resonance with the laser. For a given laser excitation energy, only certain nanotubes will be in resonance, as a function of the spacing between their van Hove singularities.

However detailed comparison is not possible for our Raman spectra, since the same laser energy was not used for both. Once the tubes become charged, the tubes that are in resonance change, indeed there is a shift in the whole Katura plot [44]. Indeed some treatments, such as Fluorination, remove all RBMs [45]).

The 240 cm^{-1} frequency mode seen in bromine intercalated graphite is also present in the case of bromine doped SWCNTs seen around the 231 cm^{-1} frequency mode, signifying bromine intercalates in-between the bundles of the tube to give this frequency mode. We note it is broader than the SWCNT RBMs, probably due to local variation in the Br_2 environment. Although the nanotubes used here were not purified, the mixing of bromine liquid with the SWCNTs coupled with sonication resulted in the dissolution of some of the impurities present in the SWCNTs compared to the pristine tubes but this can not be seen because no comparison picture but rather comparatively clean bundle surfaces are seen (see Figure 24d). Apart from this, no significant differences were seen between the sonicated sample and the dispersed tube indicating that the tubes were still in bundles.

In order to investigate the effect of bromine doping on SWNT frequency modes seen in the Raman spectra, calculations were performed as detailed earlier in the text. Firstly, the molecular structure and the changes in RBMs for isolated (5,5) SWCNTs before and after Br₂ adsorption was investigated. Just like in all the structures mentioned above, several atomic models of the bromine on the isolated (5,5) SWCNT were optimised and the most stable structure is given in Figure 25a with concentration of C₄₄Br₂. Br₂ molecules were oriented at radial, axial, circumferential and perpendicular to the nanotube axis. After atomic relaxation the Br₂ molecules oriented radially on the nanotube were found to be the most stable matching what we found for graphene above carbon atom with a C-Br distance of 3.45 Å. Thus we have found that the doping of the nanotubes with bromine gave the same orientation as in graphene with a characteristic change in bromine bond length, frequency and radial breathing mode frequency of the tube (see Table 7).

We next constructed models of (5,5) CNTs in hexagonal packed bundles by reducing the size of the unit cell to 13.2 Å. We then added Br₂ and allowed all atoms to relax, as well as the lattice parameter of the cell. The bundles expanded by 40 % in the presence of Br₂.

In this case, the most stable structure was when the Br₂ molecules were oriented parallel to the nanotube axis, this time behaving the same as Br₂ intercalated graphite.

The calculated stretching frequencies for the isolated SWCNTs/Br₂ were (264, 272 cm⁻¹) and for SWCNTs/Br₂ bundles was 204, 237 cm⁻¹. The range of values represent small local variations in Br-Br bond length and agrees with the broad peak and the lower frequency agrees best suggesting most Br₂ is intercalated into bundles which is seen in our Raman experiments above. Similar Raman experiment for SWCNTs using a lasers between ($\lambda = 619.9\text{nm}-563.5\text{nm}$) have been reported as 239cm⁻¹ [11]. The higher frequency modes observed in the Raman spectra for the SWCNTs, are similar in our model for graphene with Br₂ molecules, which suggest similarity in molecular structure. Furthermore, for bundles of SWCNTs/Br₂, a stretching frequency of 237cm⁻¹ is seen, which is close to 242cm⁻¹ frequency associated with Br₂ intercalated in graphite. Again, this gives a clue to the interlayer arrangements in the bundles of the nanotube when intercalated with the Br₂ molecules.

It's clear from literature that, it is difficult to assign a particular frequency other than the one seen near $230\text{-}245\text{ cm}^{-1}$, which has been linked to bromine intercalated graphites and Br_2 between the nanotubes bundles, see Table 7. This means the other associated frequencies seen in the Raman measurements other than the ones corresponding to the calculated frequencies could come from other chiral tubes in resonance with the energy of the laser used.

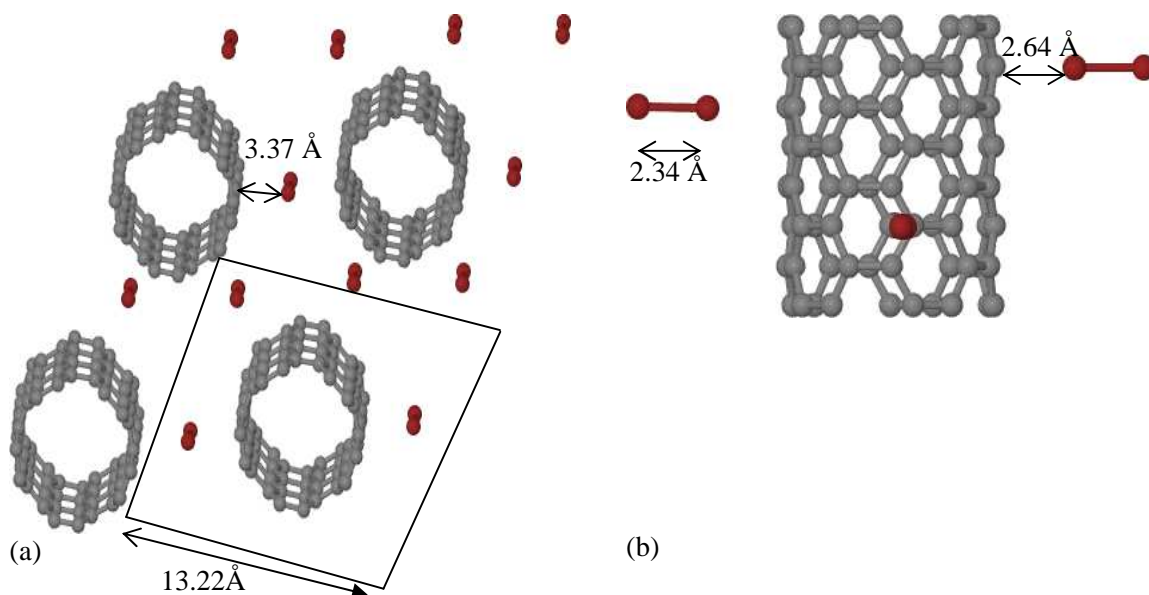


Figure 25 Optimised geometry of Br_2 absorbed on (a) bundles and (b) isolated (5,5) SWCNTs in a hexagonal lattice.

	Isolated SWNT	SWNT Bundle
Br ₂ orientation	Perpendicular	Parallel
Concentration	C ₈₀ Br ₈	C ₈₀ Br ₆
Binding Energy / Br (eV)	0.22	0.34
Br-Br stretch frequency (cm ⁻¹)	272, 264	204, 237
Br-Br bond length (Å)	2.34	2.34
Inter tube spacing (Å)	25.39	13.22
Charge transfer / Br ₂ (e)	-0.08	-0.09

Table 7. Calculated parameters for low density bromine doped with isolated and bundled SWCNTs. Stretch frequency range represents small local variation in Br-Br bondlength.

Finally, the adsorption of the Br₂ on the surface of the SWCNTs results in similar orientation to graphene in which the perpendicular orientation is the most favoured. On the other hand if the Br₂ is oriented parallel in-between the bundles of the tube, then this becomes similar to graphite, in which the parallel orientation is the most favoured which subsequently gives lower frequency modes (seen around 230-245 cm⁻¹).

4.11 Br₂ doped double-walled nanotubes (DWCNTs)

Due to large computational time required to calculate a model for DWCNTs, we used instead SWCNT calculation to predict what will be observed when DWCNTs are doped with bromine.

Our calculated RBMs for isolated (5,5) SWCNTs without bromine molecule adsorption was 339 cm⁻¹(but could not find any literature value to compare this value to as at the time of writing this thesis), which is down-shifted to 274 cm⁻¹ after bromine adsorption.

Table 8, is a summary of results for the Raman frequency of Br₂ intercalated carbon nanomaterials with different laser energies taken from ref [11]. Souza Filho et al [46], reported the Raman spectrum of Br₂ doped DWCNTs in which they showed, the Raman

intensity of the most intense peaks decreases after bromine doping. Similar studies by Gustavo et al, found the Br-Br vibrational mode to be 231 cm^{-1} at RT for Br doped DWCNTs [10]. The radial breathing modes for the DWCNTs have their outermost wall RBMs mode quenched as a consequence of bromine doping.

Based on our SWCNTs calculations, we can speculate that the only way to see a lower frequency mode at 242 cm^{-1} , will be when the bromine is intercalated between the bundles of the tubes, where we find a Br-Br frequency similar to that observed for Br₂-intercalated graphite at 242 cm^{-1} . The Raman frequency for Br₂ doped DWCNTs has been reported in the range of $232\text{-}222\text{ cm}^{-1}$ using different laser energy of excitations at 1.73 to 2.41eV and 1.92 to 2.1 eV respectively [11]. Thus, it is evident that depending on the energy of the laser used different frequency could also be seen. Our calculations give a stretching frequency for the Br₂/SWCNTs bundles and Br₂ intercalated in graphite respectively as 237 and 226 cm^{-1} which are consistent with the experimental Raman measurement on Br₂ doped DWCNTs. Therefore, based on this, one could conclude that, for DWCNTs doped Br₂, lower frequency similar to that of Br₂/graphites or SWNTs/Br₂ bundles are seen when the Br₂ are intercalated between the DWCNTs bundles.

	Laser Energy (eV)	Raman Frequency (cm^{-1})
Br ₂ (g)	2.4	323
Br ₂ (l)	2.1	306
Br ₂ (s)	2.0	300
Br ₂ -C ₆₀	-	271
Br ₂ -graphite	2.2	242
Br ₂ -SWNT	2.0-2.2	239
Br ₂ -DWNT	1.73-2.41	232
Br ₂ -DWNT	1.92-2.1	222

Table 8 Variation of Raman frequency with laser energy for isolated bromine molecules and Br₂ doped carbon nanomaterials [11]. No laser energy was reported for Br₂-C₆₀

Thus, it is reasonable to assume that the vibrational mode for Br-Br exhibits low values when charge transfer with carbon surface is higher (agrees with section 4 at the start). Hence the

variation in the frequency for the Br₂ molecules seen in the DWCNTs and SWCNTs when the Br₂ molecules are adsorbed on the surface and when intercalated with each giving different frequency.

Therefore calculation at low coverage of bromine explains why different frequencies are seen in our experimental Raman spectra, due to bromine adsorption within the intralayer bundles or on the outermost layer which giving rise to different frequency in the Raman spectra not also ruling out the resonance effects of other tubes with the laser. This also accounts for the downshifting of the RBMs associated with bromination.

Just as for graphene, in the samples with isolated SWCNTs or very small bundles where surface area is high, it would be interesting to try FTIR to look for a Br-Br stretch for the perpendicular high-dipole species of Br₂.

4.12 Polybromide Chain structures

There are multiple phases of the standard halides. In the gas and liquid phase they consist of diatomic molecules. The corresponding solid halogen acid acceptor compounds (Cl₂, Br₂, I₂) belong to the space group D_{2h}-Cmca, with two molecules in the primitive unit cell. However as well as the diatomic species, halides are able to form chain structures. The ability for these halides to form chains decreases in the order I > Br > Cl [47]. The clusters of the heavier halogens, Bromine and Iodine, easily form larger hetero and homoatomic aggregates stabilized by charge delocalization, that of Cl and F have hardly been reported, mainly due to their high volatility and reactivity.

Polyiodide chains such as (I₄²⁻, I₅⁻, I₇⁻, up to I₂₉³⁻) which result by the interactions of I, I₂ and I₃⁻ building units, were observed in extended polymer networks [48,49], with characteristic vibrational features reflected in their Raman response [50]. Also, linear or bent chains of polyiodide consisting of several atoms have been synthesized [47] and are significant in halogen doped organic systems, in which high temperature superconducting transitions in the organic systems is associated with the Iodine chains [51].

Polybromide chains of (Br_2^- , Br_3^- , Br_4^{2-} , Br_5^- , Br_8^{2-}) have been characterised in various polymers and metal complexes [47,52-54], and it is suggested that bromine undergoes interactions whose nature and orientation are similar to the more studied chains of polyiodides.

Recent theoretical studies suggest that at higher concentration of bromine, bromine chains could form inside SWCNTs, DWCNTs, graphites and graphenes [8]. Experimental studies by Sung et al. [55] suggest that bromine forms chains after encapsulation in SWCNTs with the odd numbered bromide ions, Br_3^- , Br_5^- becoming more stable than the Br_2 molecule.

DFT calculations of halogen chains have been performed mainly on polyiodide chains [56] with only three theoretical calculations reported in the literature on polybromide chains, which mainly focus on geometry optimizations and associated electron affinity.

In this thesis, the equilibrium geometry and vibrational modes of different polybromide chains were calculated using the detailed procedure described elsewhere in the thesis (in which structural optimization and double derivatives calculations on Br_2 , Br_2^- , Br_3^- , Br_4^- , Br_5^- polybromide anion and Br_4 interacting with graphene sheet was considered). In particular we have studied the reaction kinetics of (Br_4) chain formation on graphene sheets via reaction barrier calculation.

4.12.1 Polybromide Chains of Br_2^- , Br_3^- , Br_4^- , Br_4^{2-} and Br_5^-

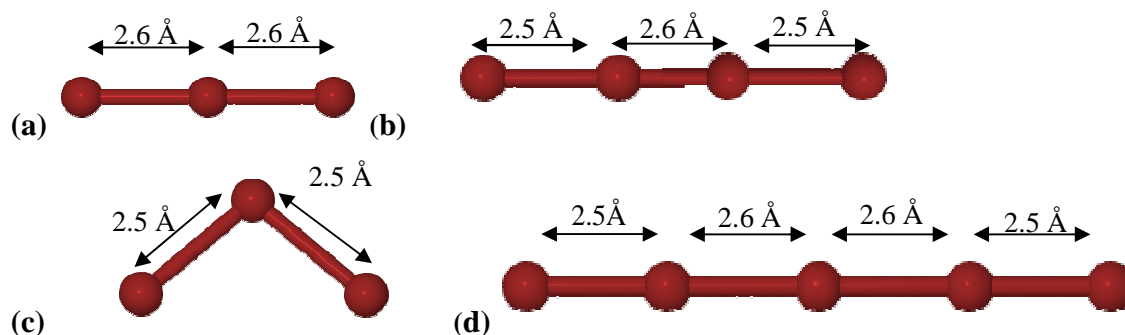


Figure 26. Our optimized geometry of some of the polybromide chains bond lengths with; (a) Br_3^- ($D_{\infty h}$), (b) Br_4^- ($D_{\infty h}$), (c) Br_3^- (C_{2v}), and (d) Br_5^- ($D_{\infty h}$) in which the symmetry group of the polybromide chains are given in parenthesis.

In Table 9, optimised structures of different bromine anions, bond lengths and their stretching modes were calculated and compared with literature DFT calculation and experimental Raman measurements, see also Figure 26. Slight charge variation could explain differences in observed modes, typically in crystals. As described in section 4, bond length and stretching frequencies, change dramatically with a gain in charge on the bromine. However in the polybromide chains the lower symmetry means that the charge state of each atom need not be equal, and this results in different bond lengths and stretching frequencies. Atomic Br and molecular Br_2 have been characterized well both experimentally and theoretically, hence, we use here as test systems for the performance of theoretical calculations on larger clusters of Br.

Calculation of Br_2^- stretching frequency from the literature lie below experiment; and this current work gave a better match to experiment. To the best of my knowledge, there is no experimental data reported for Br_2^- on bond length so we could not make any meaningful comparison between the calculated bond length, however, there was good match between other DFT calculated bond lengths of (2.81, 2.86 Å) with this work (2.83 Å).

	Br ₂	Br ₂ ⁻	Br ₃ ⁻ (D _{∞h})	Br ₄ ⁻ (D _{∞h})	Br ₄ ²⁻	Br ₅ ⁻ (C _{2v})	Br ₅ ⁻ (D _{∞h})
Bond Lengths (Å)							
This work	2.29	2.83	2.55	2.55, 2.55, 2.63	2.55, 2.93 2.93	2.49 2.59	2.45, 2.63
Other Calc.	2.315 ^a , 2.331 ^a , 2.30 ^b , 2.32 ^c , 2.360 ^f	2.990 ^a , 2.964 ^a 2.868 ^b , 2.81 ^c	2.636 ^f , 2.637 ^a , 2.618 ^a 2.593 ^j	-	2.745 ^k 3.152 ^k	2.492 ^a 2.756 ^a	
Experiment	2.283 ^d	-	2.541-2.551 ⁱ	-	2.43 ^l 2.98 ^l		2.43 ^d 2.82 ^d
Bromine structures	Calc. stretching freq. (This work) (cm ⁻¹)		Previous DFT calculations (cm ⁻¹)		Experimental Raman modes (cm ⁻¹)		
Br ₂	326		313 ^a , 321 ^a , 312 ^c , 318 ^f		320 ^d , 325 ^g		
Br ₂ ⁻	152		118 ^a , 121 ^a , 179 ^c		149-160 ^e		
Br ₃ ⁻ (D _{∞h})	93(bv), 218(as), 164(sy)		84, 86 ^a (bv), 176 ^a , 178 ^a (as), 146 ^a , 152 ^a (sy), 81 ^f (bv), 216 ^f (as), 158 ^f (sy)		210 ^h , 205 ^h , 201 ^h (as), 170 ^h , 163 ^h , 160 ^h (sy), 140 ⁿ (sy), 208 ⁿ (as)		
Br ₄ ⁻ (D _{∞h})	64, 69, 72, 94, 119, 164		(99, 106, 155.9, 102, 158.2) ^a		-		
Br ₄ ²⁻	58, 130		70, 176 ^k		(74, 167) ^k , (187, 200) ^m		
Br ₅ ⁻ (C _{2v})	16, 80, 81, 84, 90, 144, 174, 221, 227		(16.2, 74.4, 76.4, 82.5, 83.5, 122.8, 133, 192.8, 218) ^a				
Br ₅ ⁻ (D _{∞h})	184, 242				(157, 245) ^l		

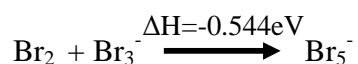
Table 9. Comparison of calculated properties of bromine for stretching modes and bond lengths with experimental Raman modes and other DFT studies (bv= bending vibration, as=asymmetric stretch, sy= symmetric stretch, {^a [57], ^b [58], ^c [59], ^d [19], ^e [60], ^f [61], ^g [62], ^h [63], ⁱ [64], ^j [65], ^k [47], ^l [66], ^m [67], ⁿ [68]}).

Br₄²⁻ is a metastable species resulting when two molecules of Br₂⁻ dimerise with formation energy per Br atom of (+0.42 eV) which is endothermic; making Br₄²⁻ unstable compared to

the other polybromide structures such as Br_3^- or Br_5^- . The charge sits primarily on the terminal atoms, accounting for the increase in bond length we observed after geometry optimization which then results in a longer bond length and lower stretching modes. Experimental differences in frequency exist due to the cations used to stabilise the polybromide ion, as seen in the Raman modes in Table 9. As a result, no inference can be made between the calculated stretch modes to that of Raman experiments, however, the bond length calculated for Br_4^{2-} fits better to experiments than the other DFT calculation methods, which predicted longer bond lengths for Br_4^{2-} . Other factors such as basis sets and the number of k-points used could contribute to the difference between the calculated stretching frequencies ($58, 130 \text{ cm}^{-1}$) and that from other DFT calculations ($70, 176 \text{ cm}^{-1}$) and also difference may be if the stretching frequency is highly anharmonic. Nonetheless, the error margins between the two separate theoretical works are acceptable.

Br_3^- polybromide anion, has been seen in various geometrical structures with different levels of symmetry because of the influence of solvent interactions and crystal fields. In this study, the asymmetric structure (linear chain) was optimised with calculated bond lengths and stretching modes compared with other similar data on this structure, where available see table above. Again, the calculated values are consistent with experimental and other theoretical calculations. The calculated bond angle was 180° which agrees with the other calculation methods together with the experimental bond angle of 177.3° , reported by D.D.L Chung for asymmetric Br_3^- [68].

Br_5^- , has two symmetry forms, i.e. $\text{Br}_5^-(C_{2v})$ and $\text{Br}_5^-(D_{\infty h})$ and are formed when Br_2 binds to Br_3^- with a binding energy of 0.11 eV per Br. Below is the reaction describing $\text{Br}_5^-(C_{2v})$ formation:



We find $\text{Br}_5^-(C_{2v})$, to be 0.23 eV more stable than the other symmetry form, $\text{Br}_5^-(D_h)$, which is mostly reported in Raman spectra experiments, with no experimental confirmation for the theoretically predicted stable form.

Our calculation for $\text{Br}_5^- (\text{C}_{2v})$, agrees with similar calculations done by others in terms of the stability of this symmetry over the linear form, and our calculated bond angles of 128.4° and 173.3° closely match that of other DFT calculations (114.6° and 177.4°) [57]. Again, the lack of experimental data on this symmetry form makes it difficult to draw any conclusions. For $\text{Br}_5^- (\text{D}_{\infty h})$, we obtain the shorter bond length almost identical to experiment with the longer bond slightly underestimated. This is reflected in the calculated stretching frequencies with the higher frequency mode matching almost exactly experiment but the lower frequency mode slightly overestimated, see Table 9.

Thus in conclusion, where comparable data is available, it appears that we are able to accurately model polybromide anions, generally reproducing experiment better than previous literature theoretical modelling results. We next turn our attention to their formation and interaction with graphene.

4.12.2 Kinetic barrier for Br chain formation

Even though extensive progress has been made in the determination of structures and transitional phases in graphite-bromine at or above room temperature with many experimental and theoretical data, a lot remains to be answered theoretically, concerning what happens to graphite-bromine at high concentration and low temperatures. The existence of polybromides chains were reported experimentally by D.D.L. Chung et al who proposed the existence of chain of polybromides at liquid nitrogen temperature in her work on graphite-bromine intercalates [69].

M. Suzuki et al [70], carried out Raman vibrational spectroscopy for bromine chains at 77K and reported frequencies as low as ($110, 96, 82, 70, 53 \text{ cm}^{-1}$). The lowest temperature Raman frequency measurement in the literature was carried out at 15K, in which frequencies for solid bromine were given as ($55, 74, 86, 101 \text{ cm}^{-1}$), by Cahil et al [16].

I am not aware of theoretical calculations confirming these polybromides chain with carbon at low temperatures. Therefore, the section of this work is aimed at giving insight on these complexes and unclear processes occurring during the formation of these structures.

Optimised geometry (Figure 27) of bromine molecules on graphene were obtained by placing two molecules of bromine at a distance of 11.28Å apart on a graphene sheet, Table 10.



Figure 27 Optimised geometries of 2Br₂ on graphene (a), Br₄ on graphene (b) and above is the hypothetical reaction for the thermodynamic transformation.

Thermodynamically, a reaction in which two molecules of bromine sitting at a distance of 11.28Å apart on graphene sheet and perpendicular to each other, will gradually align into chains of Br₄ polybromide ions with an increase in bond length and a decrease in vibrational stretching mode as a result of charge transfer but, kinetically, this seems restricted, due to the presence of a kinetic barrier.

While, the formation of chain structures is favourable, there is a barrier (activation energy) for the two bromine molecules to stick together in forming this chain which we calculate to be 0.35eV (33.77 kJ/mol). This is due to a longer range Coulombic repulsion of associated holes in graphene beneath the Br₂, and Coulombic repulsion between the Br₂ themselves at shorter distance.

This transformation, is exothermic, in which the enthalpy of formation for the reaction was calculated as, $\Delta H = -0.28\text{eV}$ (-27.01 kJ/mol), see Figure 28.

We initially studied many polymerised Br structures in graphite, often when starting from cells with too high Br density. All calculations of Br vibrational modes were consistent with

the valued reported in Table 10, i.e. in the range 170-190 cm^{-1} . This stretch frequency therefore seems to be characteristic sign of polymerisation in the C-Br system. And the doping effect due to chains appears to be stronger than that of molecular Br_2 .

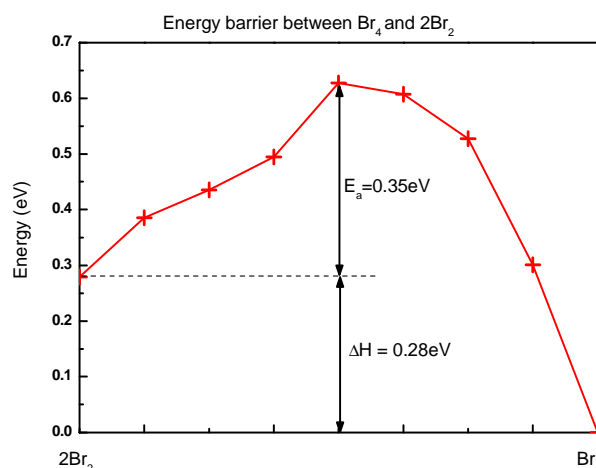


Figure 28 Energy barrier curve for Br_4 chain formation on graphene.

Calculated parameters	Br_4 on graphene	2Br_2 on graphene
Br-Br bond length (\AA)	2.53	2.33
Br-C distance (\AA)	3.52	2.70
C-Br-Br bond angle ($^\circ$)	70.3	180
Stretching frequency (cm^{-1})	175	284
Charge transfer/Br (e)	0.3	0.2

Table 10 : Calculated parameters for graphene interacting with Br_4 and 2Br_2 in the formation of chain structures.

Thus to summarise, the formation of polybromide chains is favourable but due to Coulombic repulsion of associated holes in graphene, this is kinetically hindered. For the polybromide chains longer bond lengths and low stretching frequency mode are observed.

4.13 Summary

The adsorption of Br₂ molecules at low and high density has been examined on graphite, graphene, single wall carbon nanotubes and double-walled nanotubes by ab initio DFT/LDA calculations as implemented in the AIMPRO method.

In graphene, we find that bromine molecules are preferentially oriented perpendicular to the carbon planes. The molecules form a dipole with strong associated charge transfer. The molecule forms a Br⁺ + Br⁻ pair making it infra-red active, and result in a small band gap opening in the graphene (86 meV). This is a new form of bromine molecule previously only considered as an unstable intermediate to bromine-induced carbon bond saturation. Whereas in the parallel configuration, no dipole but symmetrical charge transfer distribution between the pair of atoms. Also the binding energies calculated showed that, the parallel orientations are (0.15 eV) less stable than the perpendicular orientations and since the difference in binding energies between the perpendicular and parallel structures is negligible, it is proposed that at room temperature, these structures could be intermediate due to tumbling motion.

In graphite, bromine molecules adopt a parallel orientation to the sheets with an associated charge transfer and this is in agreement with experimental data where available. Binding energies for both *stage-1* (Br₂/AA-graphite) and *stage-2* (Br₂/AABB) were calculated to be endothermic at low coverage due to binding energy of the Br₂/graphite not being able to offset the interlayer separation energy for graphite: which was calculated as 36.74 meV/atom for AB- and AA- being 12 meV/atom less stable. But on bromination, there is a preferential stability for AA-stage-1 than AB-stage-1, even though, experimentally no stage one compound of bromine have been thought to exist.

Also, for the nanotubes, when bromine was oriented perpendicular to the isolated tubes, it gives similar arrangements as with graphene and when in bundles they intercalate within the bundles as with Br₂ intercalated graphites lying parallel on the hexagons and by similar extension, the same phenomenon could be seen as happening for the double wall nanotubes.

At high Br₂ concentration, polybromide chain structures will be thermodynamically favourable. But, the formation of these bromine chain structures is not spontaneous. There is

an activation barrier calculated as -27.01KJ/mol and kinetically such chain structures will not be feasible. Thus, it could imply that, the Coulombic interaction between the bromine results in repulsion between bromine molecules as a result of charge transfer from the neighbouring graphene carbons to the bromine molecules.

For these systems, LDA seems to be sufficient and addition of vdW energy term shouldn't qualitatively change our results, but possibly shifting our values for the binding energies calculated. In any case, agreement between LDA values and experimental data where available is excellent.

Finally, bromine may provide way to reliably produce bilayer graphene if used in conjunction with secondary separator afterwards.

4.14 References

- [1] M. S. Dresselhaus and G. Dresselhaus, *Advances in Physics* **30**, 139-326 (1981).
- [2] S.-H. Jhi, S. G. Louie, and M. L. Cohen, *Solid State Commun.* **123**, 495-499 (2002).
- [3] N. Jung, N. Kim, S. Jockusch, N. J. Turro, P. Kim, and L. Brus, *Nano Letters* **9**, 4133-4137 (2009).
- [4] S. Bandow, G. Chen, G. U. Sumanasekera, R. Gupta, M. Yudasaka, S. Iijima, and P. C. Eklund, *Phys. Rev. B* **66**, 075416 (2002).
- [5] K. K. Bardhan, J. C. Wu, and D. D. L. Chung, *Synthetic Metals* **2**, 109-120 (1980).
- [6] M. S. Dresselhaus, G. Dresselhaus, and J. E. Fischer, *Phys. Rev. B* **15**, 3180 (1977).
- [7] X. Fan, L. Liu, J. L. Kuo, and Z. Shen, *J. Phys. Chem. C* **666** (2010).
- [8] A. Yaya, C. P. Ewels, I. Suarez-Martinez, P. Wagner, S. Lefrant, A. Okotrub, L. Bulusheva, and P. R. Briddon, *Phys. Rev. B* **83**, 045411 (2011).
- [9] P. G. Collins, A. Zettl, H. Bando, A. Thess, and R. E. Smalley, *Science* **278**, 100 -102 (1997).
- [10] G. M. do Nascimento, T. Hou, Y. A. Kim, H. Muramatsu, T. Hayashi, M. Endo, N. Akuzawa, and M. S. Dresselhaus, *J. Phys. Chem. C* **113**, 3934-3938 (2009).
- [11] G. M. do Nascimento, T. Hou, Y. A. Kim, H. Muramatsu, T. Hayashi, M. Endo, N. Akuzawa, and M. S. Dresselhaus, *Nano Letters* **8**, 4168-4172 (2008).
- [12] A. M. Rao, P. C. Eklund, S. Bandow, A. Thess, and R. E. Smalley, *Nature (London)* **257** (1997).
- [13] H. J. Monkhorst and J. D. Pack, *Phys. Rev. B* **13**, 5188 (1976).
- [14] C. Hartwigsen, S. Goedecker, and J. Hutter, *Phys. Rev. B* **58**, 3641 (1998).
- [15] I. Suarez-Martinez, A. A. El-Barbary, G. Savini, and M. I. Heggie, *Phys. Rev. Lett.* **98**, 015501 (2007).
- [16] J. E. Cahill, *J. Chem. Phys.* **51**, 4514 (1969).

- [17] W. T. Eeles and J. A. Turnbull, Proceedings of the Royal Society of London. Series A. Mathematical and Physical Sciences **283**, 179 -193 (1965).
- [18] P. C. Eklund, N. Kambe, G. Dresselhaus, and M. S. Dresselhaus, Phys. Rev. B **18**, 7069 (1978).
- [19] A. Erbil, G. Dresselhaus, and M. S. Dresselhaus, Phys. Rev. B **25**, 5451 (1982).
- [20] K. T. Chan, H. Lee, and M. L. Cohen, Phys. Rev. B **83**, 035405 (2011).
- [21] T. Ohta, A. Bostwick, T. Seyller, K. Horn, and E. Rotenberg, Science **313**, 951 -954 (2006).
- [22] X. Peng and R. Ahuja, Nano Letters **8**, 4464-4468 (2008).
- [23] G. Giovannetti, P. A. Khomyakov, G. Brocks, V. M. Karpan, J. van den Brink, and P. J. Kelly, Phys. Rev. Lett. **101**, 026803 (2008).
- [24] D. C. Elias, R. R. Nair, T. M. G. Mohiuddin, S. V. Morozov, P. Blake, M. P. Halsall, A. C. Ferrari, D. W. Boukhvalov, M. I. Katsnelson, A. K. Geim, and K. S. Novoselov, Science **323**, 610-613 (2009).
- [25] F. Schedin, A. K. Geim, S. V. Morozov, E. W. Hill, P. Blake, M. I. Katsnelson, and K. S. Novoselov, Nat Mater **6**, 652-655 (2007).
- [26] A. N. Rudenko, F. J. Keil, M. I. Katsnelson, and A. I. Lichtenstein, Phys. Rev. B **82**, 035427 (2010).
- [27] I.-S. Martinez, Theory of Diffusion and Plasticity in Layered Carbon Materials, PhD. Thesis, 2007.
- [28] J. D. Bernal, Proceedings of the Royal Society of London. Series A, Containing Papers of a Mathematical and Physical Character **106**, 749-773 (1924).
- [29] J.-C. Charlier, X. Gonze, and J.-P. Michenaud, Europhys. Lett. **28**, 403-408 (1994).
- [30] L. X. Benedict, N. G. Chopra, M. L. Cohen, A. Zettl, S. G. Louie, and V. H. Crespi, Chemical Physics Letters **286**, 490-496 (1998).
- [31] R. Telling and M. Heggie, Philosophical Magazine Letters **83**, 411-421 (2003).
- [32] R. Setton, P. Bernier, and S. Lefrant, *Carbon Molecules and Materials* (London, 2002).
- [33] T. Sasa, Y. Takahashi, and T. Mukaibo, Carbon **9**, 407-416 (1971).
- [34] M. Heerschap and P. Delavignette, Carbon **1**, 405 (1964).
- [35] W. Rüdorff, Zeitschrift Für Anorganische Und Allgemeine Chemie **245**, 383-390 (1941).
- [36] J. J. Lander and J. Morrison, Surface Science **4**, 103-107 (1966).
- [37] S. M. Heald and E. A. Stern, Synthetic Metals **1**, 249-255 (1980).
- [38] A. Erbil, A. R. Kortan, R. J. Birgeneau, and M. S. Dresselhaus, Phys. Rev. B **28**, 6329 (1983).
- [39] S. M. Heald and E. A. Stern, Phys. Rev. B **17**, 4069 (1978).
- [40] J. E. Fischer, Accounts of Chemical Research **35**, 1079-1086 (2002).
- [41] L. Grigorian, K. A. Williams, S. Fang, G. U. Sumanasekera, A. L. Loper, E. C. Dickey, S. J. Pennycook, and P. C. Eklund, Phys. Rev. Lett. **80**, 5560 (1998).
- [42] H. Kataura, Y. Kumazawa, N. Kojima, Y. Maniwa, I. Umezumi, S. Masubuchi, S. Kazama, Y. Ohtsuka, S. Suzuki, and Y. Achiba, Mol. Cryst. and Liq. Cryst. **340**, (2002).
- [43] Y. Mackeyev, S. Bachilo, K. B. Hartman, and L. J. Wilson, Carbon **45**, 1013-1017 (2007).

- [44] J.-Y. Mevellec, J. Amer. Chem. Soc. (In Submission) (2011).
- [45] P. R. Marcoux, J. Schreiber, P. Batail, S. Lefrant, J. Renouard, G. Jacob, D. Albertini, and J.-Y. Mevellec, Phys. Chem. Chem. Phys. **4**, 2278-2285 (2002).
- [46] A. G. Souza Filho, M. Endo, H. Muramatsu, T. Hayashi, Y. A. Kim, E. B. Barros, N. Akuzawa, G. G. Samsonidze, R. Saito, and M. S. Dresselhaus, Phys. Rev. B **73**, 235413 (2006).
- [47] M. C. Aragoni, M. Arca, F. Demartin, F. A. Devillanova, F. Lejl, F. Isaia, V. Lippolis, A. Mancini, L. Pala, and G. Verani, Eur. J. Inorg. Chem. **2004**, 3099-3109 (2004).
- [48] P. H. Svensson, M. Gorlov, and L. Kloo, J. Inorg. Chem. **47**, 11464-11466 (2008).
- [49] H.-H. Li, Z.-R. Chen, Y. Liu, J.-B. Liu, L.-Q. Guo, and J.-Q. Li, J. Mol. Struct. **934**, 112-116 (2009).
- [50] P. Deplano, J. R. Ferraro, M. L. Mercuri, and E. F. Trogu, Coord. Chem. Rev. **188**, 71-95 (1999).
- [51] D. W. Kalina, J. W. Lyding, M. T. Ratajack, C. R. Kannewurf, and T. J. Marks, J. Amer. Chem. Soc. **102**, 7854-7862 (1980).
- [52] C. R. Hubbard and R. A. Jacobson, J. Inorg. Chem **11**, 2247 (1972).
- [53] D. Schneider, O. Schuster, and H. Schmidbaur, Organometallics **24**, 3547-3551 (2005).
- [54] H. Vogt, D. Wulff-Molder, and M. Meisel, J. Chem. Sci. 1443 (1996).
- [55] D. Sung, N. Park, W. Park, and S. Hong, Appl. Phys. Lett. **90**, 093502 (2007).
- [56] S. B. Sharp and G. I. Gellene, J. Phys. Chem. A **101**, 2192-2197 (1997).
- [57] P. Schuster, H. Mikosch, and G. Baur, J. Phys. Chem. A **109**, 5 (1998).
- [58] P. Mcgrath and L. Random, J. Phys. Chem. **94**, 551 (1991).
- [59] A. B. Sannigrahi and S. D. Peyerimhoff, Chem. Phys. Lett. **175**, 279-281 (1990).
- [60] C. A. Wight, B. A. Ault, and L. Andrews, J. Inorg. Chem. **15**, 2147 (1976).
- [61] J. J. Novoa, F. Mota, M. H. Whangbo, and J. M. Williams, J. Inorg. Chem. **30**, 54-58 (1991).
- [62] K. P. Huber and G. Herzberg, *Molecular Spectra and Molecular Structure-IV* (Van Nostrand Reinhold, New York, 1979).
- [63] G. R. Burns, R. M. Renner, Spectrochimica Acta Part A: Mol. Spec. **47**, 991 (1991).
- [64] P. J. Estienne, Cryts. Struc. Commun. **42**, 1614 (1986).
- [65] K. O. Christe, D. A. Dixon, and R. Minkwitz, Z. Anorg. Allg. Chem **612**, 51 (1992).
- [66] D. Ghosh and D. D. L. Chung, Synth. Met **7**, 283-288 (1983).
- [67] J. H. Clark, L. Maresca, and R. J. Puddephatt, J. Inorg. Chem. **7**, 8 (1968).
- [68] D. D. L. Chung, Phase Transitions: A Multinational Journal **8**, 35 (1986).
- [69] D. D. L. Chung, Journal of Materials Science **37**, 1475-1489 (2002).
- [70] M. Suzuki, T. Yokohama, and M. Ito, J. Chem. Phys. **51**, 1929 (1969).

Chapter 5

Pi-stacking vs. electrostatic interactions

The forces of importance in the interactions between molecules have long been recognized [1,2]. However, it is only recently that theoretical and experimental methods have been developed to directly measure the interaction forces between individual molecules under experimental conditions. These specific interactions resulting from multiple weak, non-covalent interactions are thought to be responsible for the complex nature that controls our daily lives. For example, hydrogen bonding has been shown to be a critical feature in all double helical structures of nucleic acids and the basis for genetic coding in all living organisms [3]. Similarly, it is H-bonds and other supramolecular interactions that ensure the stability of the proteins.

This section will explore non-covalent interactions such as π - π stacking, by the use of the AIMPRO/LDA method described earlier to study the interactions between PPV/SWCNTs, PPV/Graphene, PPV/PPV, and SWCNTs/Benzene in which a Benzene dimer is used as a prototype for π - π interaction.

5.1 What is π - π interaction?

The π - π interaction can be defined as non-covalent interactions involving sp^2 -hybridized hydrocarbons containing aromatic rings. The term is often generally used when unsaturated hydrocarbons are involved in non-covalent interactions [4].

These interactions are usually caused by intermolecular overlapping of π -orbitals in π -conjugated systems, which becomes stronger by increasing the number of aromatic rings. In an aromatic system with less than three rings for instance, theoretical calculations suggest that aromaticity contributes little to the stacking forces, and that the strength of these forces which contributes to the stacking does not differ significantly from the *Van der Waals* forces

also experienced by similarly-sized saturated molecules when stacked [5]. Similarly, in larger aromatic rings containing more conjugated rings, π - π stacking interactions appear to dominate, due to π -orbitals-dependence, which contributes to the dispersion component of the vdW force in equivalent saturated molecules.

As noted by Grimme [4], π - π stacking interactions are not unique, and noncovalent interaction involving nonaromatic rings are often quite favourable. For example, a recent theoretical calculation by Bloom et al. [6] shows that the interaction energy between sandwich complexes of cyclohexane with benzene is -2.91 kcal/mol, which is nearly 80 % greater than that exhibited by the benzene sandwich dimer.

Other forms of non-covalent interactions are dipole-dipole, hydrogen bonding, cation- π , anion- π and charge-transfer interactions.

Next we discuss an introduction to the concept of this π - π stacking interaction from literature as well as theoretical approaches used in describing these noncovalent interactions.

5.2 Introduction

Interactions involving π - π bonding species play a crucial role in the stability and conformations of DNA and proteins, crystal stacking of polymers containing aromatic rings and the recognition of molecular species (self-assembly) [7–9]. These have also been known to play a major role in the stabilization of host-guest complexes and in the interactions of certain drugs to DNA [10].

However, the nature and variety in the structure and composition of aromatic compounds coupled with the lack of a thorough understanding of π - π interactions, makes it difficult to investigate their interactions. These difficulties come from the treatment of the electron correlation, dispersion, polarization and solvation, in a manner that is appropriate to the context of the applications and within the confines of available computer resources [11]. Experimental methods such as NMR have been used to study the nature of π - π interactions, giving partial information about their energetic and substituent effects. However, the interpretation of these experimental results is complex as solvation effects and secondary interactions complicate the situation [10].

In the light of this, quantum mechanical studies become pre-eminent in the study of interactions involving π - π bonding. Higher order wave function methods such as coupled-cluster theory through the use of perturbative triples, CCSD(T), with large basis sets [10,12,13], are known to reach a good level of accuracy, but, the computational cost is too demanding: time scales to about $O(N^7)$, where N is the number of atoms in the system. Less expensive methods such as Møller-Plesset perturbation (MP2) can also become expensive when a large basis function is taken into consideration. Also, they lead to overestimation of the electron correlation effects that are inherent in pure π - π interactions [11]. These then also leave problems for the theoretical understanding of larger systems containing π - π stacking interactions, which are still not fully understood [4,6]. Nonetheless, current theoretical chemistry literature suggests that, the high level of electronic structure theory approach used by Sinnokrot et al [14] and Tsuzuki et al [12] gives an accurate model of π -stacking interaction. However the computational cost mean it cannot be applied to many of the large systems we are considering here, such as PPV-nanotube interactions. Therefore a simpler and computationally less demanding approach is needed. The only theoretical means for understanding larger π - π systems is through the use of density functional technique which scales much less critically with basis set size than the advanced wave functional methods.

For this reason we benchmark here the DFT/LDA approach against these more complex techniques. Our approach is pragmatic, more akin to numerical experimentation: The question we are posing is, to what extent can simpler exchange-correlation description such as LDA successfully reproduce π - π interaction for extremely larger systems?

5.3 Computational Methods

We performed density functional calculations using the local density approximation with a $2 \times 2 \times 1$ k-point grid for graphene, $1 \times 1 \times 4$ k-point grid for benzene and a $1 \times 1 \times 2$ k-point grid for the nanotubes. Localized Gaussian basis sets with 38 functions per carbon and 16 per hydrogen were used, with Hartwigsen, Geodecker and Hütter relativistic pseudopotentials. A

Fermi temperature smearing for the electron population of $kT=0.04\text{eV}$ was incorporated to improve the convergence. Two carbon basis sets were used – either 22 or 38 independent Gaussian basis functions. The PPV-SWCNTs energies were calculated with 22 functions per carbon in our earlier calculations, the band structures were studied with 38 and all other calculations with 38 basis functions. The effect of basis set size is discussed later.

Hexagonal supercells were used containing nanotubes with lengths in the range 24.29-25.41Å (160-400 atoms), to which we added the PPV chain ($\text{C}_{22}\text{H}_{18}$). The graphene was modeled using an 8×8 graphene supercell (C_{128}). A large vacuum spacing was used in each case (at least 13.5Å between tubes) to ensure no inter-system interaction. Isolated tubes and graphene were fully relaxed and then held fixed once the PPV or benzene was added. The PPV and benzene were then fully geometrically optimized. Binding energies are calculated in comparison to the isolated separate components, i.e. for a PPV-nanotube, $E_B = E_{CNT-PPV} - E_{CNT} - E_{PPV}$. Inter-PPV interaction was calculated with two PPV chains in a large hexagonal supercell with full atomic relaxation of both chains.

Single point energies were obtained for the benzene dimer in three different configurations (T-shaped, parallel-displaced and parallel-stacked) by initially optimizing the equilibrium geometry of a single benzene molecule and then systematically varying the distance between the center of mass of the two benzene monomers (denoted by R_1 in Figure 29) while the monomer geometries were kept rigid.

Contour map plots were obtained by applying diffusion constraints to the molecules, varying and then fixing their directions in the xy plane but allowing their z height in the direction to vary freely during an optimization. The constraints were applied to carbon atoms (7, 8, 15, & 16) of vinylene bonds on the PPV chains in the xy and on all atoms in benzene in the xy directions which are interacting with substrates (SWNTS, Graphene, Benzene and PPV). All other atoms in the PPV molecule were allowed to freely relax in x, y and z directions. These substrates were kept frozen during the relaxation process.

5.4 Benchmarking- benzene-benzene interaction

The benzene dimer has been widely studied as a prototype for understanding noncovalent bonding of π - π interactions, both theoretically [10,12,14–22] and experimentally [23–28].

Theoretical and experimental studies suggest two minima on the potential energy surface for the benzene dimer; (i) parallel-displaced (PD), (ii) T-shaped (T) configurations, which are usually observed in crystal structures of simple aromatic compounds with the T-shaped being the dominant [29,30] and the highest energy transitional structure (iii) parallel-stacked (PS) (see Figure 29).

Although the benzene dimer can adopt a wider range of different relative configurations, only the three prototype structures mentioned above are critical in the understanding of π - π interactions.

The first theoretical studies on the benzene dimer using high levels of electronic structure theory such as CCSD(T) with corrections for basis set effects used for giving insights on prototype systems was done by Sinnokrot et al. [14] and Tsuzuki with co-workers [12]. This study was very instrumental in revealing mistakes made earlier, by wrongly assuming that the (T-) shaped dimer was more stable energetically than the (PD) orientation. Rather, the two configurations were found to be nearly isoenergetic.

The small binding energy for the benzene gas-phase dimer (~ 2 - 3 kcal mol⁻¹) and the depth of its potential energy surface makes it highly challenging both experimentally and theoretically. The dimer is stable at low temperature and low pressure and is prepared in supersonic jet expansions into the vacuum. Due to the sizes and shapes of the various clusters produced, it is relevant to use detection techniques that are very sensitive to their masses. This then makes it difficult experimentally for their description. Also, the diverse experimental methods employed have often resulted in controversies in results and only matches if there are at least two separate low-energy potential minima or if the system is highly continuous with low barriers [14]. Work on beam electric resonance studies by Klemperer et al [25,31], on the gas-phase dimer gave evidence for a *T-shaped* configuration with C_{2v} symmetry. Studies by Arunan and Gustowsky [32] on gas-phase benzene dimer

using microwave spectroscopy reported the separation distance for the *T-shape* configuration as 4.96 Å. Also, an extensive study on benzene dimer and isotopomers by applying mass selective, ionization-detected stimulated Raman spectroscopy (IDSRS) was made by Henson et al [33]. Their results showed that the T-shape geometry for the benzene dimer is dominant.

The existence of other configurations such as the *parallel displaced* and *parallel-stacked* was not ruled out since the method used was only sensitive to dipole moments of molecules and these two configurations have no dipole moments. In fact, hole-burning spectroscopy suggested the existence of more than one isomer of the benzene dimer [34]. Further studies on the intermolecular vibrations of the benzene dimer by Felker and co-workers [35,36], is consistent with a dimer which is composed of a monomer that was not related by a symmetry element as is the case for the *T-shaped* geometry. The existence of *parallel-displaced* with C_{2h} symmetry was supported by optical absorption spectroscopy measurements by Bernstein et al [37].

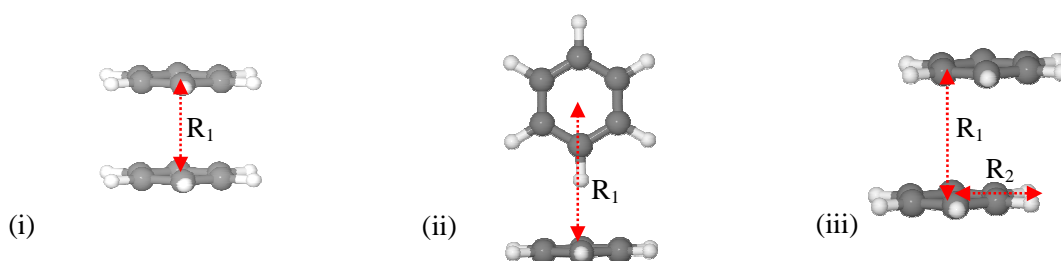


Figure 29. Our calculated benzene dimer in various geometries including (i) *parallel-stacked* (PS), (ii) *T-shaped* (T) and (iii) *parallel-displaced* (PD). Here R_1 is the distance of separation (center-center) and R_2 is the displacement from the center. Dashed-red vertical arrow indicates center-center separation and horizontal red-arrow displacement from the center position.

Using the experimental dissociation energy of the ions and the ionization potentials of the benzene dimer and monomer, Grover et al. [38], and Krause et al. [39], gave the values of 2.4 ± 0.4 and 1.6 ± 0.2 kcal mol⁻¹ respectively as the binding energy of the dimer.

Accurate ab initio calculations of the benzene dimer necessitate both the use of an extensive basis set with diffuse functions and high levels of dynamic correlation in order to predict binding energies on the potential energy curves which are comparable to CCSD (T) level of theory, which then can be used for calibrating other methods and for modeling π - π systems.

What effects are involved in π -stacking then? Figure 30, comes from an email exchange I had with Professor Stefan Grimme. It shows that when the benzene dimer is parallel AA-stacked ($R=0$), the main contribution to the total energy is the positive exchange repulsion at shorter distances which is primarily offset by the dispersion interaction, giving a net total attraction energy of around -2.1 kcal/mol. The electrostatic effects and inductive effects are relatively small, and constant with displacement as the top benzene is laterally displaced away from "AA" structure to the equilibrium "AB" structure ($R \approx 3.2$ Bohr), the exchange repulsion drops significantly with some cost in reduced binding dispersion; however the net effect is to reduce the total energy.

According to Grimme [4], the dispersion component term is composed of two main components; an orbital-dependent part responsible for the π -stacking effects (*PSE*) which dominates at short intermolecular distances and a non-orbital dependent part which actually weakly counters the *PSE* and mainly dominates at larger intermolecular distances.

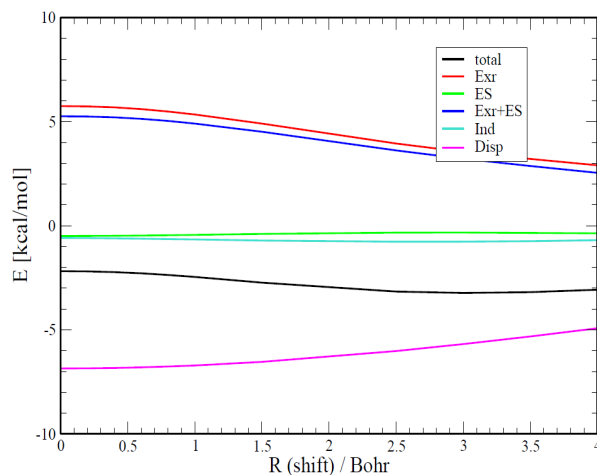


Figure 30. Energy decomposition analysis (EDA) for benzene dimer indicates the lateral displacement of the top benzene ring, so $R=0$, corresponds to “AA” parallel structure (Courtesy of Prof. Dr. Stefan Grimme [Private Communication, 2011]).

We calculated these structures using AIMPRO with the settings described earlier.

A large basis set per atom was used in order to minimise basis set superposition errors (BSSE) for the calculation of the single point energies. The absence of dispersion corrections could modify our results slightly.

So how do we do with LDA? In Figure 31, our calculated single point energies for the three different configurations of the benzene dimer are compared with a Lennard-Jones (LJ) best fit potential energy curve. It can be seen from (Figure 31a) that for the T-shape dimer the LJ fit passes through the minimum of the LDA results. This is due to the presence of dipole moments in this dimer, whose interaction our method is able to describe very well. As one moves away from the minimum the long-range effects such as dispersion forces dominate which we are unable to capture. For the other dimers i.e. PD has only very weak dipole and PS none at all (Figure 31 (b & c)) and as a result there is poor match to the LJ curve in the region around the minimum and at long range which is purely attributed to dispersion interactions.

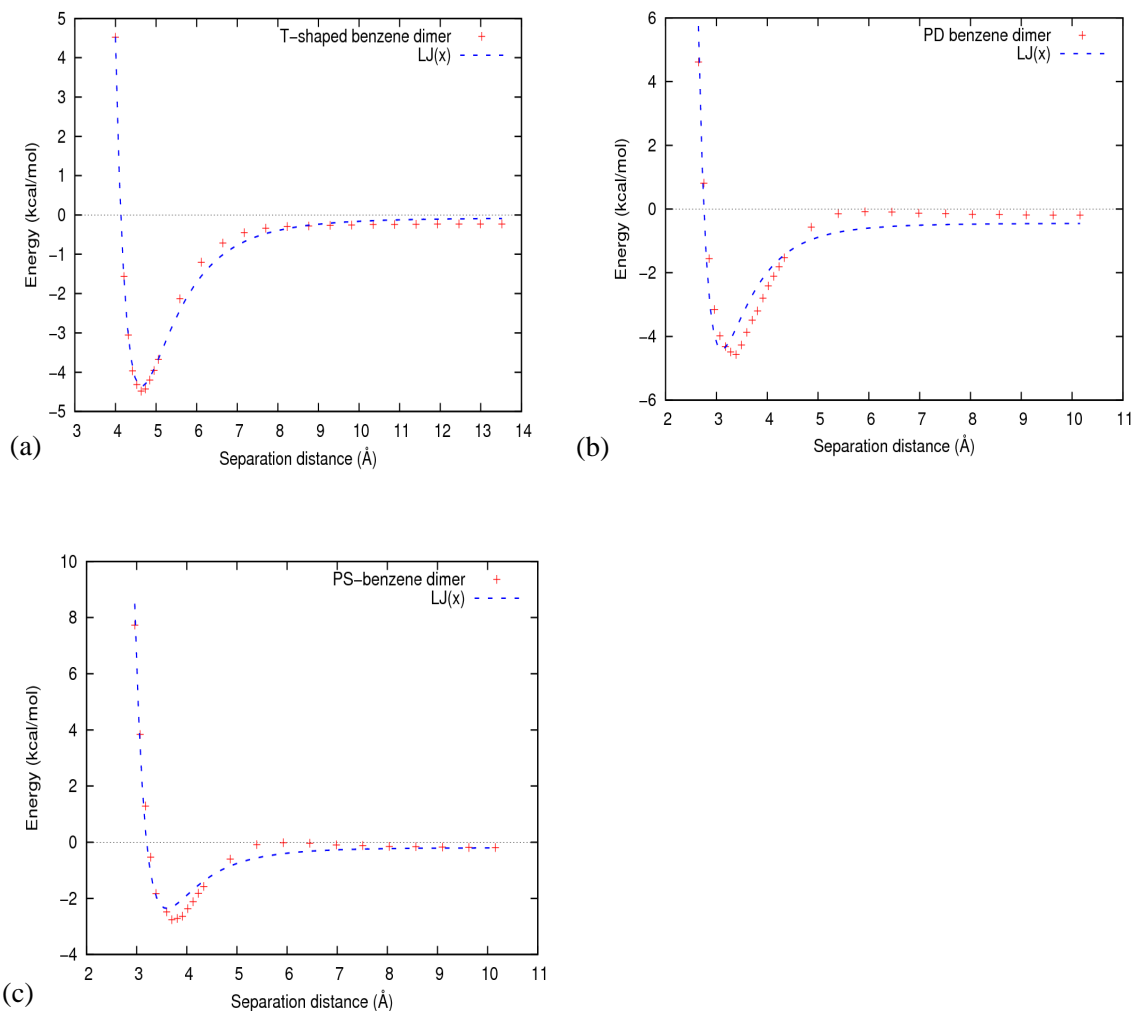


Figure 31. Potential energy curves for (a) edge-on face (T-shaped), (b) parallel displaced (PD) and (c) parallel-stacked (PS) with Lennard-Jones (LJ) potential fit. Dashed blue lines are (LJ) and red crosses are data points from our DFT/LDA system for the single point energy calculated.

Our approach does not include dispersive forces which follow an asymptotic behaviour. The incorporation of correlation corrections into DFT/LDA is necessary for describing weaker attractive forces which will directly affect the magnitude of the interaction energy. For system involving π - π interactions, the electrostatic interaction controls the geometry of

these π - π systems together with orbital-dependent dispersion and not the classical (atom pairwise) dispersion or vdW, but this vdW interactions will only act to add to the net interaction energy [4,30]. Structurally correct but quantitatively energies will need shifting. This justifies our approach to base our study on DFT/LDA.

Method	T-shaped	Parallel displaced (PD)	Parallel stacked (PS)
This work	-4.250	-3.371	-2.501
CCSD(T)	-2.492	-2.513	-1.564
DF-LMP2	-3.503	-4.427	-3.147
DF-SCF-LMP2	-2.436	-2.604	-1.833
MP2	-3.516	-4.324	-3.222

Table 11. Interaction energies (kcal mol⁻¹) for different configuration of benzene dimer compare with this Work and other methods taken from Ref [16].

Method	T-shaped	Parallel displaced	Parallel stacked
This work	4.89	3.52	3.71
CCSD(T) [14]	5.00	3.60	3.90
DF-LMP2 [16]	4.89	3.70	3.72
DF-SCF-LMP2 [16]	5.04	3.54	3.89
MP2 [14]	4.90	3.40	3.70

Table 12. Interatomic distance, R_1 (Å (see Figure 29)) for this work compared with other methods taken from Refs [14,16].

Tables (11 & 12) give the binding energies for our single point energies benzene dimer and the minimum lattice separations in comparison to other highly correlated methods. Our method compares favorably with other methods such as MP2 and DF-LMP2 in the absence of correlation corrections which are known to best describe non-covalent interactions.

Nonetheless, to capture dispersion interactions which are instrumental in the binding of these dimers, one still needs a correlated description of the electrons. Our binding energies estimated for the different dimer configurations, although slightly overestimated (which is intrinsic in DFT/LDA) by comparing to the most highly efficient correlation method to date, CCSD (T), is still within reasonable range. This also signifies how correlation corrected functional will influence our calculated binding energies, should it be incorporated in our methods. But, our interlayer separations are in good agreement with the other methods.

Figure 32, is a comparison of the potential energy curves for the different benzene dimer configurations obtained in this thesis using AIMPRO modeling package, with that taken from refs [16,40] is given. From Figure 32(a, c) we can see our approach does better than the other dispersion corrected wave function methods such as MP2 and DF-LMP2 in describing the minimum interactions energy and the distance of separation for (PS and PD configuration) by taking the CCSD(T) value as the standard reference method. Similarly, for the T-shaped dimer our method gave rather higher binding energy as compared to the other methods near the equilibrium distance (see Figure 32b) and this is attributed to LDA, which is known to overestimate binding energies. Figure 32d shows the reason why the GGA approach is not good for treating systems of this nature since it does not predict any binding. Addition of vdW to the GGA will improve the binding considerably. This is not the case for our LDA approach which gives attractive binding for the different benzene dimer configurations together with other correlated methods and some respect gives much closer binding energies with reference to the CCSD (T) method.

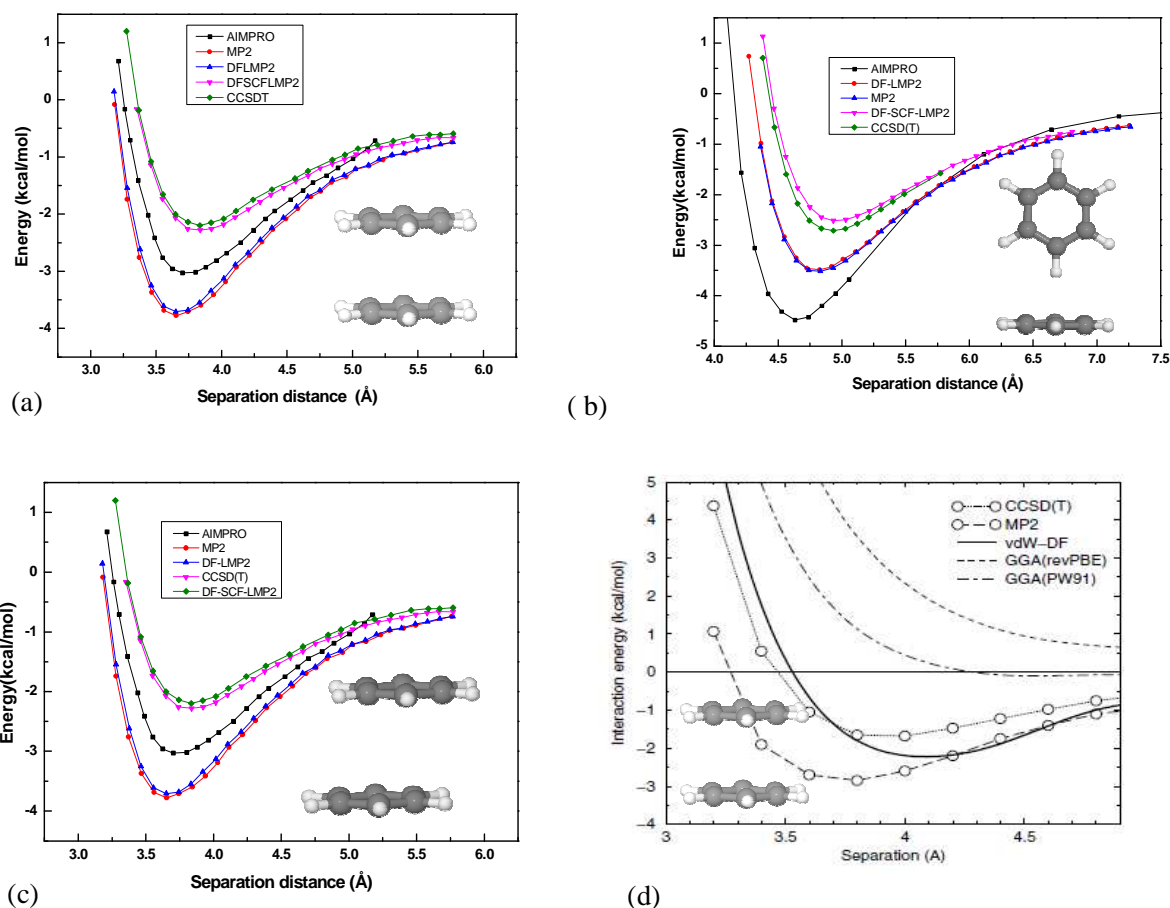


Figure 32. Comparison of the potential energy curves for (a) parallel-stacked, (b) T-shaped, (c) parallel-displaced benzene dimers between this work (AIMPRO) with that of CCSD(T), MP2, DF-LMP2, DF-SCF-LMP2 results of Grant et al [16] and (d) compares the results of CCSD(T), MP2, vdW-DF with that of GGAs both revPDE and PW91 taken from work of Dion et al. [40].

LDA is also known to perform much better in interactions with systems involving sp^2 -like materials, such as graphite [41,42]. Theoretical studies by Tournus et al. [43], showed that, LDA is able to describe the interactions between benzene and carbon nanotube better than GGA, which is also governed by non-covalent π - π stacking interactions.

We have shown here that although the dispersion interaction is lacking in DFT/LDA, the method is nonetheless able to predict with reasonable precision the interlayer interactions of benzene dimer (also the relative stability of the isomers) and slightly overestimates the binding interactions as compared to the CCSD(T) which is used as a standard for the benzene dimers. But, as stated earlier in this thesis, such higher correlated methods carry a large computational cost and when larger systems are being considered, the only way is to use DFT/LDA. In our test system for the benzene dimers, as shown by our potential energy curves, we have shown it to be a reliable and semi-quantitatively accurate tool for studying such systems.

Based on the good agreement we found in calculating the potential energy curves for benzene dimers using AIMPRO/LDA with other correlated methods, we feel justified using it in the later chapters for the study of other systems involving π - π stacking such as graphene, single-walled carbon nanotubes (SWCNTs) interacting with PPV (poly-paraphenylene-vinylene) and benzene molecules.

5.5 Surface Contour Maps

5.5.1 Benzene-benzene interaction

The majority of studies of benzene-benzene interaction focus on a few high symmetry configurations. The relative speed of our techniques allows us to explore in more detail the potential energy surface for benzene-benzene interaction.

We plotted the energy for two benzene rings as a function of their center-to-center displacement in a grid point of xy plane with the interplanar separation z allowed to vary freely whilst fixing the movement of the dimer in the xy directions.

Figure 33 (a,b), is a contour map showing the least and most stable benzene dimer. The plot confirms that the most stable configuration is the T-shaped dimer. The PS dimer in the red regions of the map is unfavoured as a result of π -electron repulsions (competition between Pauli exchange repulsion and electrostatic effects in the dimer). As the stacking arrangements become offset, this leads to other transition state structures with much lower repulsive energy

than the initial structures until one eventually reaches the stable form which is the parallel-displaced (PS) dimer (0.15 eV more stable than two isolated benzene molecules), in which the electrostatic effects are minimized as a result of offset in the dimer planes. Filled orbitals then overlap, at the same time leading to the minimization of the Pauli exchange repulsion, (shown in Figure 33a) with the most favorable conformation in the blue regions of the map.

For the edge-on-face (T-shaped dimer), there is a strong dipole attraction between the hydrogen atom of one monomer pointing to the centre of another monomer which constitutes a σ - π interaction, in a system 0.2 eV more stable than two isolated benzene molecules (see Figure 33b) with most favoured dimer in the blue region of the map. As the two monomer positions are changed i.e. from the blue regions in the map with respect to the xy planes, other structures with lower binding energies are seen (the other colours in the map) until an unfavourable state is reached (colour red in the map, Figure 33b). At this state, it is seen that, the dimers are totally displaced from the initial favourable position, and the benzene molecules are no longer interacting due to their distance apart.

The contour plot for the different positions of the dimers and their binding are consistent with the notion that π - π repulsion increases as the aromatic pair are facing each other.

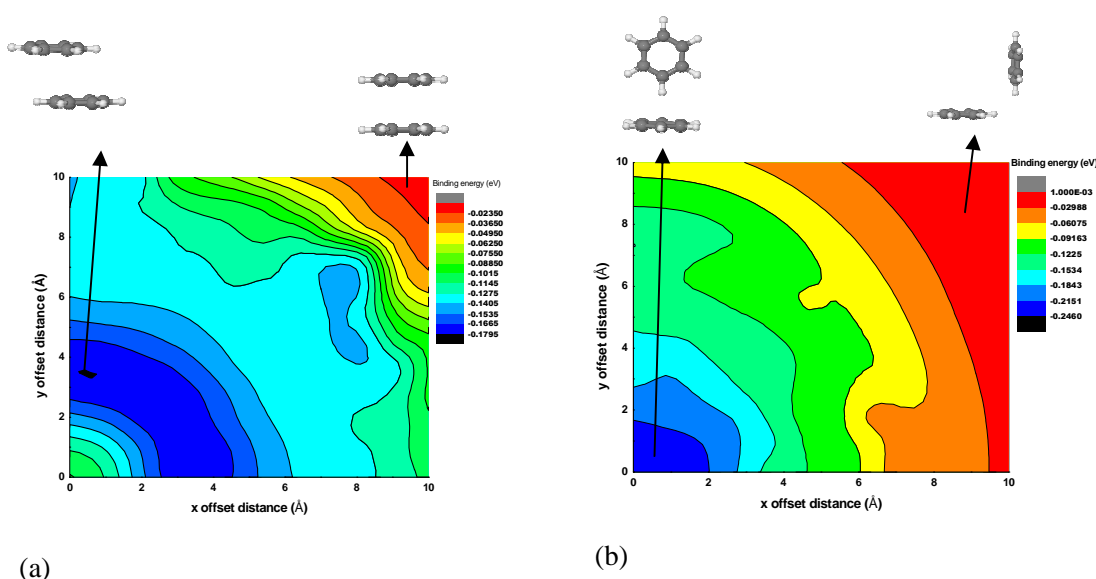


Figure 33. Contour plot showing binding energies (eV) between two benzene dimers as a function of their centre-centre offset in a grid points of xy plane (Å); with the interplanar separation, z, allowed to vary freely without constraints. The xy plane lies in the plane of the lower benzene molecule. With (a) for the parallel-stacked (PS) and (b) edge-on face (T-shaped) geometry. The geometries for the highest binding energy state, favourable state (blue region) and that of the lowest unfavourable (red region) are also indicated.

5.5.2 Benzene-graphene interactions

We next examined the binding between graphene and benzene. We placed benzene over a large unit cell made up of 128 atoms of graphene, and shifted the benzene laterally in the (x & y) directions. At each point the graphene was held fixed and all benzene atoms fixed in the x & y directions, but allowed to move freely in the z direction.

Figure 34(a,b) is the resultant contour plot map for graphene interacting with a benzene molecule. The interaction shows a similar molecular arrangement as that of the benzene dimer outlined above. For the T-shaped orientation, the most favourable geometry is when the benzene molecule is positioned at the centre of a graphene hexagon, which results in a higher binding for this conformation, that is 0.10eV more stable (blue region) than the other conformation (red region) shown in Figure 34a. Unlike the benzene-benzene stacking case, this time the parallel configuration is more stable than the T-shaped geometry.

When the benzene molecules are parallel stacked on a graphene sheet, the most stable orientation is when the parallel stacking switches to a PD conformation (in which the centre of the aromatic ring is positioned on top of a graphene carbon similar to graphite AB stacking), which is 0.10 eV more stable than the PS configuration (equivalent to AA stacking) see Figure 34b. The benzene is physisorbed on graphene, producing a parallel geometry in which we find the adsorbate to be positioned 3.27 Å above the surface in good agreement with 3.24 Å value reported by Rochefort et al [44] using LDA. This distance between graphene and benzene is smaller compared to the interlayer distance of 3.71 Å we obtained for parallel stacked benzene dimer, and is close to the interlayer spacing for hexagonal AB-graphite of 3.35 Å.

Adsorption of benzene on graphite reported in the literature gives binding energy values for the two most stable adsorption sites (PS and PD) from 0.229 to 0.350 eV with LDA [43], and the experimental value is 0.45 eV [45] which are in close agreement with our binding energy of 0.38 eV.

Parallel stacking of benzene with graphene is much more stable than perpendicular, unlike benzene-benzene interaction in which the perpendicular is more stable. These differences may arise as in the graphene-benzene interaction, the parallel stacked geometry which maximizes the effect of π - π stacking interaction whilst in the latter, this is not the case. In addition all the carbon atoms in graphene are neutral, reducing the dipolar interactions in the perpendicular configuration as compared to benzene-benzene interactions.

This work also agrees with theoretical studies by Olga et al. [46], on the adsorption of benzene and ovalene lying parallel to hydrogen terminated graphene sheet. They found that, both the ovalene and the benzene preferred the AB-stacking, which is the global minimum but not the AA-stacking which is a global maximum.

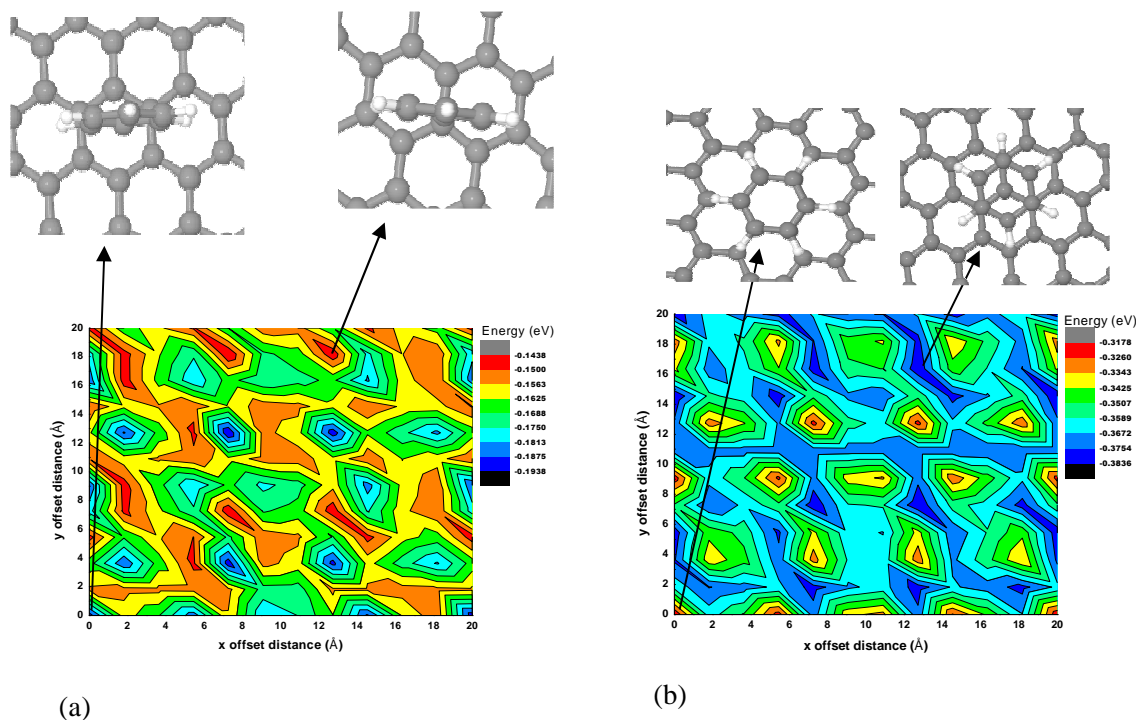


Figure 34. Contour plot showing binding energies (eV) interactions between graphene and benzene molecule as a function of their centre-centre offset in a grid of xy plane (\AA); with the interplanar separation, z , allowed to vary freely without constraints; (a) edge-on face (T-shaped) and (b) for the parallel-stacked (PS). The geometries for the highest binding energy state, favourable state (colour blue) and that of the lowest unfavourable (colour red) are also indicated.

5.5.3 Benzene-SWNT Interactions

Aromatic compounds are known to interact with graphite and also with the graphitic sidewalls of carbon nanotubes [47]. This interaction does not disturb the aromatic systems conjugation of the network and is therefore ideal for applications such as electronic and others where noncovalent functionalisation is needed. However the presence of aromatic molecules on the sidewall of a CNT could modify their transport and electronic properties [48].

Benzene molecule adsorption on armchair [(4,4), (6,6)] and zigzag [(7,0), (13,0)] CNTs were computed with the benzene molecule either perpendicular above the hexagon hole of SWCNTs, above a carbon atom of SWCNT, or parallel-stacked (with the centre of the benzene molecules just above an atom of CNT) (see Figure 35). In Table 13, for each tube, the binding energies after geometry relaxation are compared with benzene oriented on graphene in parallel stack and perpendicular orientation.

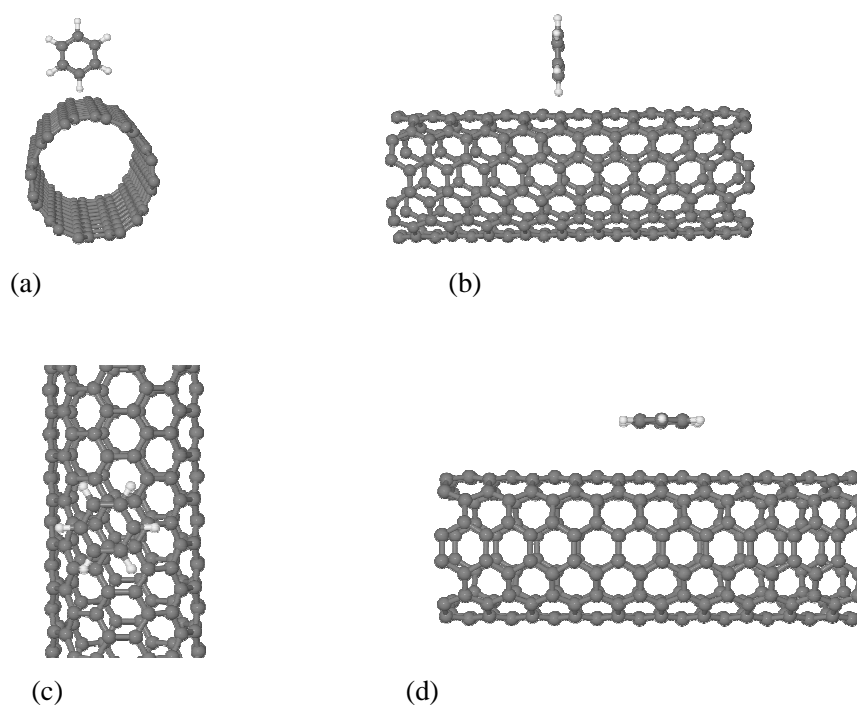


Figure 35. Optimised geometry of benzene on (6,6) SWCNTs with (a) top view, (b) side view for perpendicular benzene on SWCNTs and (c) top view, (d) side view for benzene/SWCNT in parallel-stacked conformation.

Tube (n,m)	Diameter (Å)	Stacking Binding energy (eV)	Perpendicular (hexagon centers) Binding (eV)	Perpendicular (on carbon) Binding (eV)
(4,4)	5.43	0.19	0.16	0.14
(6,6)	8.14	0.25	0.13	0.13
(7,0)	5.48	0.18	0.11	0.12
(13,0)	10.18	0.26	0.10	0.10
Graphene	-	0.38	0.19	0.15

Table 13 .Binding energy for different orientation of benzene molecule on various nanotubes with different diameters in comparison with benzene oriented on graphene sheet.

In all the conformations studied the most favourable is the PD (on-top conformation) with higher binding energies as compared to the perpendicular orientation more than 0.15 eV higher in the case of larger diameter tubes. This is the same conformation as benzene on graphene with the latter having a higher binding energy than benzene on CNTs. Table 13 can be summarized as follows; (i) binding is weakest to smallest tubes, (ii) binding increases with diameter (iii) even on large tubes is less than graphene. This implies that curvature is important for conjugation (decreases it) so on small diameter tubes, π stacking is damaged and lastly (iv) benzene perpendicular above the hexagon hole of SWCNTS or when one hydrogen atom of the benzene is placed directly above a carbon atom of the SWNTS, there is no any significant difference observed in binding between the two conformations, but there seems to be a preference for the metallic tubes in this conformation as compared to the semi-conducting tubes. This may be because charge in the metallic tubes can redistribute more easily to interact with the δ^+ on the hydrogen.

Our theoretical findings are in agreement with the theoretical calculation of benzene on different nanotubes by Tournus et al. [43], who found the parallel stacked conformation coming out as the most favourable with increasing diameter of the nanotubes.

5.6 Poly Para-Phenylene Vinylene (PPV) Polymer

This is an attractive polymer for the theoretical study of properties of conjugated polymers, because it takes the form of relatively simple quasi-one-dimensional molecules arranged in a 3D crystal structure. These arrangements therefore make it possible to study the conformational and electronic characteristics of both the isolated and crystal chains of the PPV polymers.

PPV has aromatic groups in its chain length which makes it stiffer and mainly responsible for most of the noncovalent interactions of these polymers. The physical properties of polymeric materials are also governed by polymer-polymer interactions. This can be dominated by dipole-dipole interactions, exchange repulsion of atomic constituents, steric repulsion and hydrogen bonding mechanisms. This behavior in their interactions is mostly associated to the local or non-local electrons of the polymers.

Although there have been a few theoretical studies on these types of polymers [49–51], the main underlying mechanisms for understanding the interaction in these polymers is often lacking, due to the use of simple computational techniques such as basic force field approaches and empirical molecular mechanics which do not take into account the electronic description of these conjugated polymers.

Hence, a lot of these interactions can be understood by quantum mechanical modeling to calculate their effects, thereby giving the origin and nature of these interactions.

5.6.1 Isolated PPV (3-Phenyl repeat monomer unit)

The isolated PPV chain studied in this work is made up of a *3-phenyl repeat monomer*.

We study two different configurations made up of flat and bent configurations shown in Figure 36. After the atomic relaxation, we find the flat conformation to be 0.30 eV more stable than the meta-stable bent conformation. This is in agreement with theoretical studies by Zheng et al. [50], where they found the isolated monomer unit to be planar or flat and the most stable. We also find a very small torsional angle of 8° slightly stabilizes the molecule further. Indeed, experimental diffraction studies [52,53] suggest a torsion angle of approximately 5° per PPV monomer within the planes that increases with temperature.

In general for PPV two competing mechanisms can be seen to occur; (1) for extended π -conjugation to occur the PPV chain must be planar and (2) steric hindrance occurring between the benzenoid ring and the vinyl linkage will in some respect favour a non-planar conformation, which might also come with an energetic cost (which we calculated to be 0.12 eV) see Figure 36b.

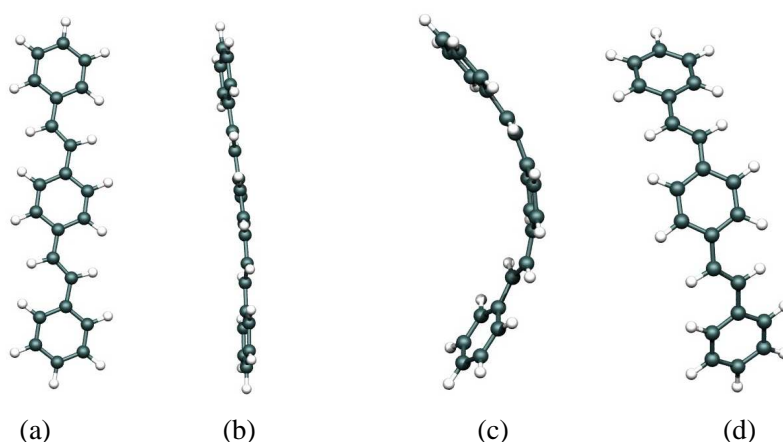


Figure 36. Optimized geometries for 3-phenyl repeat monomer units of PPV with ((a) front view for flat geometry, (b) side view of the stable planar configuration and ((c)-side view, (d)-front view) of a meta-stable bent configuration.(0.30 eV less stable than (b) which is the most stable, with a slight torsional twist in our calculations of 8° per PPV monomer.

5.6.2 Electronic Structure of Isolated PPV Chains

Since there are eight carbon atoms in a PPV repeat unit cell but only one electron per carbon atom can take part in π conjugated bonding, and because each energy level can take a maximum of two electrons, this implies that only four π valence states, with lowest energy are filled and that four π^* conduction band states will be empty per unit cell. This means the benzene ring contributes three π -electron pairs and the remaining π - electron pair comes from the vinylene bond, (see Figure 37 for the band structure of PPV molecules).

The LDA band gap for the two configurations was calculated: that of the planar PPV is 2.17eV, and the bent PPV is 2.13eV with the experimental band gap given as 2.5eV [54]. In the bent configuration the energy levels are all shifted up by about 0.9eV with respect to the energy level of the flat configuration. A previous theoretical calculation of the band gap for a PPV oligomer chain was found as 1.3 eV [50]. The low band gap value obtained by this group could be due to their use of an infinite chain in their calculation that would give a lower gap. Our short chain introduces confinement effects which can open the gap wider. Compared to the other theoretical value, our calculated value for the band gap matches closely to the experimental value of 2.5 eV.

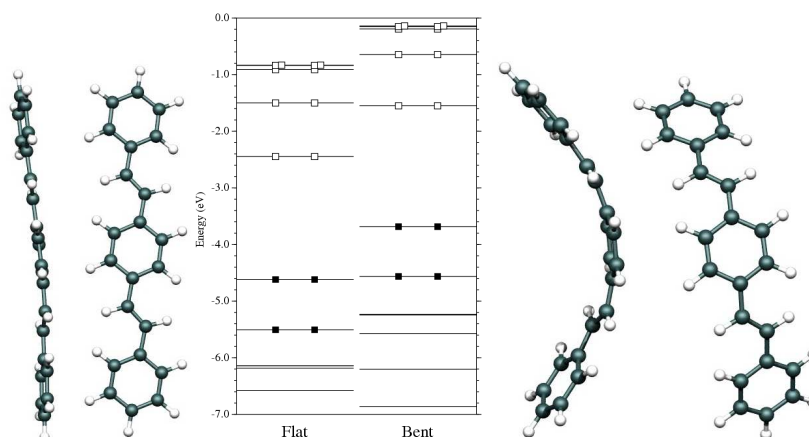


Figure 37. Energy levels for molecular (3-phenyl chain unit) PPV, in (left) the stable flat configuration, and (right) a meta-stable bent configuration. In both cases the gap remains around 2.15eV, but once bent the levels are shifted upwards in energy. [Black squares indicate filled states and white squares empty states]

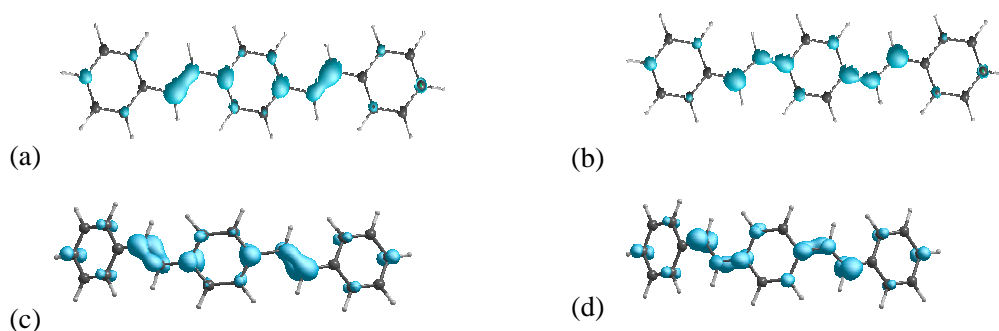


Figure 38. Square of the wavefunction isosurfaces for HOMO (a), LUMO (b) for planar isolated PPV chain and HOMO (c), LUMO (d) for bent isolated PPV chain.

In Figure 38, the wavefunction plot for the charge density isosurfaces for the highest occupied molecular orbital (HOMO) and lowest unoccupied molecular orbital (LUMO) are shown for both the planar and bent meta-stable isolated PPV chains. For the planar PPV, the HOMO state (Figure 38 (a)) is delocalized with most states on the vinylene linkages, but in the LUMO state (Figure 38 (b)) there is no state on the vinylene bond but on the single C-C bond between the benzenoid ring and that of the vinylene carbon because it's an anti-bonding orbital.

A similar effect was seen in the bent meta-stable isolated PPV for HOMO state (Figure 38 (c)) and (Figure 38 (b)) LUMO. However the increase steric repulsion between neighbouring atoms as a result of bending the PPV chain coupled with the shortening of double bonds induced by bending could account for the shifting of the energy levels of 0.9 eV which we calculated compare to the planar conformation (see Figure 37) .

Having established that the planar PPV isolated chain is the most stable form, we then moved on to study the effects of stacking two planar PPVs in parallel-stacked and T-shaped geometry and also the interaction of this polymer with graphene sheets and different diameter nanotubes, as described below.

5.6.3 PPV-PPV Interactions

PPV is known to have the T-shaped structure as its solid crystal structure (herringbone) [52], shown in Figure 39.

The interactions between two PPVs (3-phenyl repeat unit) in AA-stacked and T-shape configurations were studied by varying their positions on a grid of points (xy plane) to determine the most stable conformation at each configuration (see Figure 40), in a similar way to our previous treatment of benzene. One of the PPV chain was frozen whilst in the other PPV chain two atoms at the far end of each vinyl linkage were constrained in the xy directions but allowed to optimize freely in the z direction. All the other atoms in the 2nd PPV chain were allowed to move freely.



Figure 39 Herringbone crystal structure of PPV in the x and y directions, (taken from reference [50]) Where $\Phi=52^\circ$

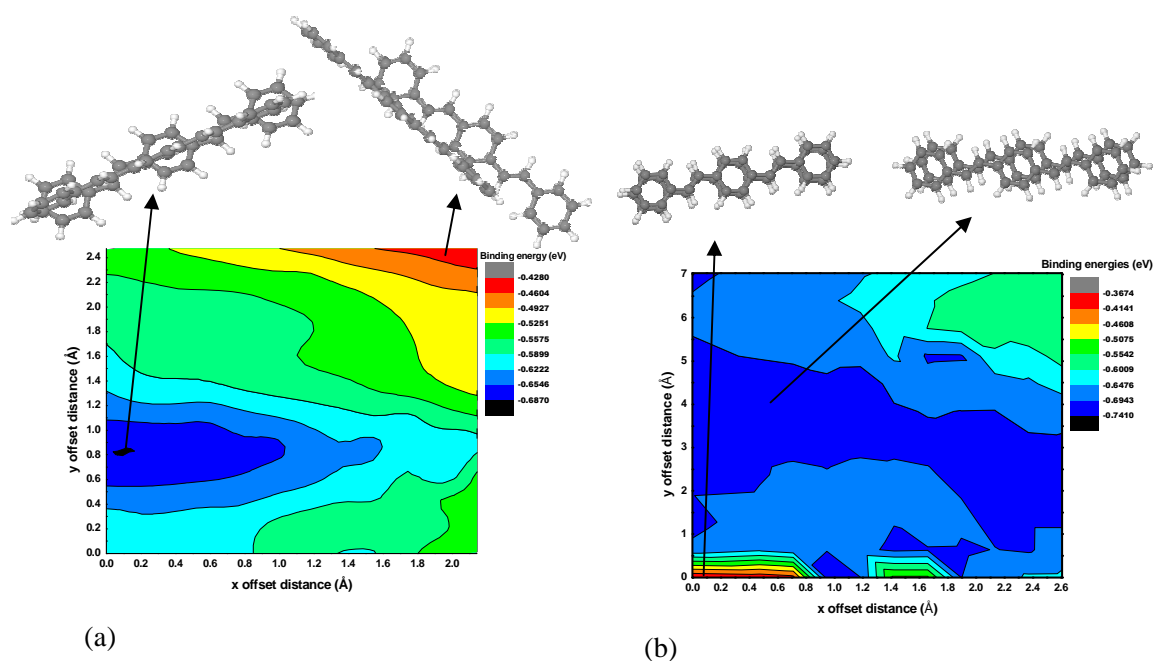


Figure 40. Contour plot showing binding energies (eV) interactions between two PPV molecules as a function of their centre-centre offset in a grid of xy plane (Å); with the interplanar separation, z , allowed to vary freely without constraints; (a) edge-on face (T-shaped) and (b) for the parallel-stacked (PS). The geometries for the highest binding energy state, favourable state (colour blue) and that of the lowest unfavourable (colour red) are also indicated.

Figure 40 shows that the PPV stacked in a T-shape and PS- configuration are the ones that result in energy minimum structures similar to that of the benzene-benzene and benzene-graphene previously discussed. As for the benzene-benzene, the energy of the T-shaped and PS structures are very similar, unlike benzene-graphene. Binding energies are roughly three times those of benzene; this is consistent because the molecule is roughly three and half times bigger. Unlike benzene-benzene, in this case the parallel stacked is slightly more energetically favoured than the perpendicular stacking. This is because of the increased π - π aromaticity.

As the two interacting PPV in the PS are displaced in the xy plane, they reach a conformation where the PPV-dimers assume an “AB-graphite” type configuration i.e. a staggered conformation, which minimizes the steric repulsion between the hydrogens at the periphery of the aromatic rings (map-(b)). For the T-shaped (map-(a)), the energy minimum structure

is formed when the hydrogens above the hexagonal ring of one PPV molecule point directly to the middle of the hexagonal ring of the other PPV molecule below.

So these results show that PPV-PPV interaction is similar to benzene-benzene interaction with stacking now favouring a more graphitic parallel conformation. We next turn our attention to the interaction of graphene with PPV.

5.6.4 PPV-graphene interaction

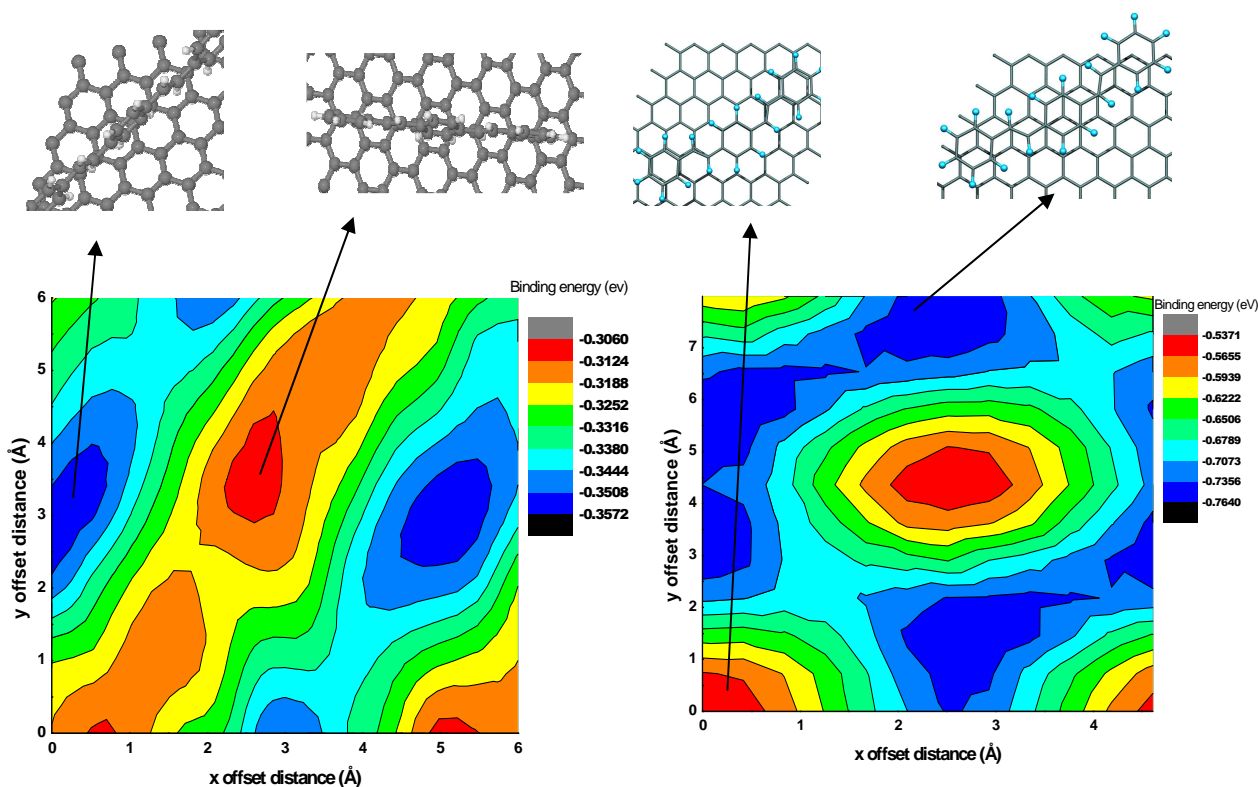


Figure 41. Contour plot showing binding energies (eV) interactions between Graphene-PPV in the T-shaped (left) and parallel-stacked (PS) (right) conformation as a function of their centre-centre offset in a grid of xy plane (\AA); with the interplanar separation, z , allowed to vary freely without constraint. The geometries for the highest binding energy state, favourable state (colour blue) and that of the lowest unfavourable (colour red) are also indicated.

Our contour plot for the interaction of graphene with PPV is given in Figure 41. This was obtained using the procedure described before in which the graphene sheet was kept frozen during the optimization run constraint applied in the PPV by constructing a grid of points in the xy plane and then allowing it to move freely in the z direction during relaxation.

As for benzene on graphene, the parallel stacked structures are much more stable. T-shaped geometry shows a weaker binding than the parallel configuration, similar to the benzene.

The global maximum (least stable) corresponds to the PS positions in which all of the atoms in neighbouring layers face each other, which is normally an “AA-stacking” type conformation with an interlayer spacing of 3.51 Å between the molecules and the surface with binding energy of 0.5 eV. The global minimum (most stable) corresponds to that of PS adopting the parallel displaced (PD) conformation (graphite AB-stacked conformation) with a binding 0.2 eV higher and an interlayer spacing of 3.22 Å (see Figure 41).

The contour plot suggests that there is an energetic cost in moving from the AB-stacking geometry to an AA-stacking (Figure 41). This then defines the largest barrier in energy difference between the AA- and AB-stacking for the PPV lying parallel on graphene sheet. Next, we calculated the frictional force involve in sliding the PPV over the graphene from the global minimum position, AB-stacked, to the global maximum, AA-stacking. This is the differential of the energy plot in Figure 41 and is shown in Figure 42.

As expected, at the AB-stacking, which corresponds to the energy minimum structure, the friction force is equal to zero (0 N). A force of 0.13 nN will be required to slide the PPV directly from the stable position to the energy maximum AA-stacking conformation which is improbable. However, in the minimum energy position, it will be much easier to slide the PPV on the graphene between AB configurations which require a smaller force (0.04 nN) see Figure 42.

This is important for composite application and this can be compared to experiments where synergistic effect on composite of this nature will have a higher mechanical strength in which the interface between the PPV and the graphene form an AB-stacking pattern.

These results are in broad agreement with experimental studies on the frictional mechanisms between small graphene flakes and graphites using a frictional force microscope that

achieves a resolution in the lateral forces down to 15 pN. It was found that there is a strong dependence of friction on the orientation of the molecules [55]. The frictional force was maximal when the orientation angle, which defines the lattice mismatch between the flake and substrate, was zero or 60° meaning the flakes slide over the graphite surface in commensurate contact. Ultra-low friction behaviour and enhanced slipperiness was observed when the flake slides over graphite surface in an incommensurate contact. However we note that we have not looked at rotating the PPV due to time constraints.

A theoretical study on the adsorption of PAHs on hydrogen terminated graphite shows that there is a large force in moving from an AB-stacking orientation of these PAHs to AA-stacking, this agrees with our studies [46].

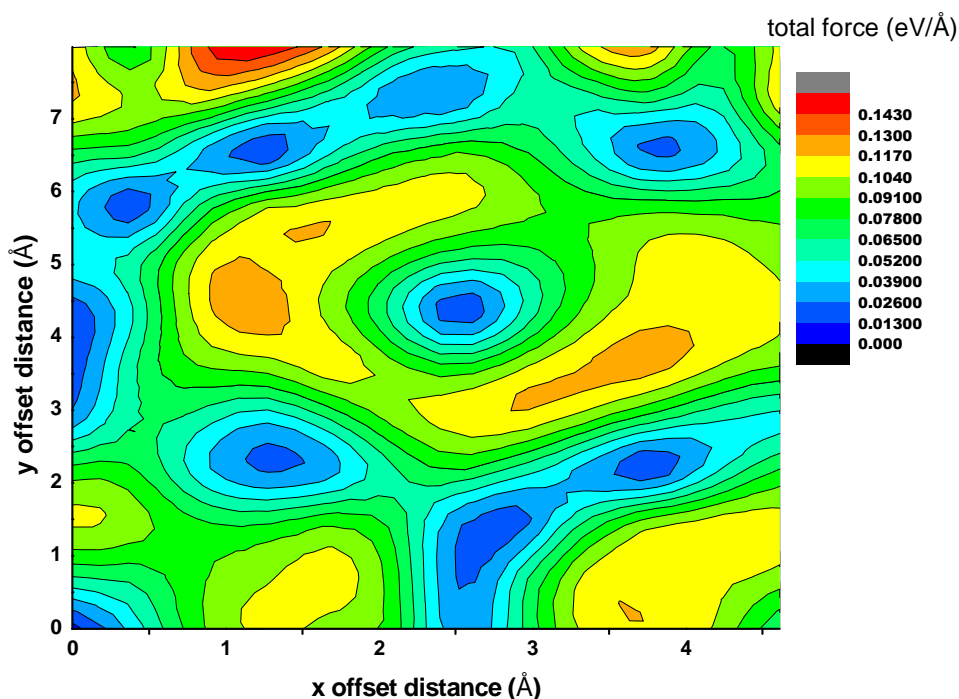


Figure 42. Energy gradient (force) plot for PPV interacting with graphene in a grid point of xy plane (Å).

5.7 Non Covalent modification of Single-Walled Carbon Nanotubes (SWCNTs)

Even though there is intense interest in exploiting the novel properties of carbon nanotubes in electrical and mechanical devices, the realization of these applications is so far very limited, because CNTs are highly hydrophobic and often form insoluble aggregates. The presence of multiple chirality tubes also presents a problem in achieving the potential applications of CNTs. Two important hurdles of hydrophobicity and conformational heterogeneity in both aqueous and non-aqueous pose considerable challenges for their separation and assembly and therefore limit their highly envisaged applicability.

Therefore, solubility of these tubes can be enhanced by chemical modification of SWCNTs, through covalent functionalization using polymers, substituted phenyl groups, and other many substituent groups. By this way, the chemical method can perturb the electronic structure of the nanotubes and for the worst cases will lead to destruction of the tubes.

Non covalent modification is one of the most widely used approach to separate bundles of nanotubes and make individual tubes. Because the electronic properties of tubes remain intact, this has attracted a lot of studies compared to the covalent functionalization methods. It is widely believed that the interfacial binding between CNTs and polymer matrix controls the efficiency of load transfers and since CNTs are known to have a uniform charge distribution, there is hardly any electrostatic interactions between nanotubes and polymers, which means in the absence of chemical functionalization, π - π stacking will dominate the interactions [56]. In these cases the strength of interfacial binding will depend therefore, on the conformational geometry of the polymer with respect to the nanotube.

It is therefore, important to explore the possibility of optimizing noncovalent intermolecular interactions between CNTs and polymers in order to achieve strong interfacial transfers.

In this section, we investigate the relationship between different geometries of PPV polymer interacting with different SWCNTs diameters and graphene, using the AIMPRO code and also, by comparing our calculation with available experimental results from our group.

5.7.1 PPV/SWCNTs complex

Conjugate polymers have been shown to exhibit good binding with SWCNTs and electron microscopy studies have demonstrated the wrapping of SWCNTs by several polymers [57,58].

Theoretical modeling of CNTs interacting with single-stranded DNA have shown that, it binds to the nanotube in a helical wrapping to the surface, via π - π stacking in which the DNA was demonstrated to provide a tube within which the nanotube resides, which makes it water soluble [59]. Also, Lordi and Yao [60], used force field based molecular mechanics calculations to determine the interfacial strength and morphology of the polymer conformation on SWCNTs and they found that, for a polymer the helical morphology wrapping around the SWCNTs is the most important factor for building ultrastrong nanocomposites, while the interfacial binding energy plays a minor role. Furthermore, using molecular dynamic simulations, other authors have studied the interactions between one or two polymers interacting with nanotubes. Even though some of these studies cannot represent the bulk nanocomposite properties, they however give useful information on the nature of the interface between polymer and nanotube. Yang and co-workers [56] studied the interaction between poly(styrene) PS, poly(phenylacetylene) (PPA), poly(para phenylene vinylene) (PPV) and SWCNTs using molecular dynamics; they found that the monomer structure plays a vital role in determining the strength of the interaction between the SWCNTs and polymer. Based on their simulations, they suggested that polymers with backbones containing aromatic rings are much promising for noncovalent binding of CNTs into composite structures. McCarthy and co-workers [61] noted that the driving force for polymer adsorption can dictate the conformation of the polymer relative to the CNTs, and other studies [58,62] indicated that the CNT structure can also dictate the conformational characteristics of the adsorbed molecules.

Molecular dynamics simulations by Liu and co-workers [63], only observed helical wrapping for single chains of oligomers with stiff backbones, which they also determined to be sensitive to the conformational arrangement of the repeat units within the chain.

Composite materials based on the polymer wrapping of multi-walled nanotubes (MWCNTs) using PPV has been reported by Ago et al. [64] and they subsequently investigated the physical nature of the interaction. Others like Dalton et al. [65] also extended this concept by using the copolymer poly (p-phenylenevinylene-co-2,5-dioctyloxy-m-phenylenevinylene) (PmPV-co-DOctOPV) for wrapping and separating SWCNTs.

Recent studies [66–68] have suggested that, a combination of backbone stiffness and aromaticity and also π - π stacking interactions can stabilize the polymer adsorption to the CNTs surface and can also lead to enhanced functionalization.

We investigated the effect of polymer wrapping on nanotubes via density functional theory (DFT) calculations on a triphenyl PPV section ($C_{22}H_{18}$) by firstly, optimizing the PPV chain in various orientations next to a range of metallic and semiconducting nanotubes, and a graphene sheet. Since the calculations were performed earlier during the thesis, a smaller basis set for C of only 22 independent functions (pdpp) was used. This is discussed later.

The resultant structures for a (6,6) nanotube are given in Figure 43 with the binding energies plotted in Figure 44. In all cases PPV-CNT binding is significantly stronger than PPV-PPV (0.301 eV), i.e. there will be strong and preferable binding between the nanotubes and the polymer.

The most stable orientation is always with the PPV parallel to the nanotube axis, lying flat on the tube surface at a distance of $\sim 3.1 \text{ \AA}$. The PPV chain remains relatively flat, with small displacements of the hydrogen atoms. There is no significant difference in binding energy between metallic and semiconducting tubes, and instead a weak dependence on tube diameter favouring larger tubes.

Placing the PPV along the axis but perpendicular to the nanotube wall, or curving the PPV chain circumferentially around the nanotube result in weaker binding (around 0.4eV less), although still significant and still stronger than PPV-PPV interaction.

Tube (n,m)	Diameter (Å)	Binding (eV)			Difference (Axial-Circumferential) parallel (eV)
		Axial parallel to surface	Axial perpendicular to surface	Circumferential parallel to surface	
(4,4)	5.43	-1.13	-0.72	-0.63	0.50
(6,6)	8.14	-1.27	-0.79	-0.94	0.33
(8,8)	10.86	-1.23	-0.72	-0.94	0.30
(10,10)	13.57	-1.29	-0.76	-1.04	0.25
(7,0)	5.48	-1.18	-0.76	-0.60	0.58
(9,0)	7.05	-1.17	-0.73	-0.76	0.41
(11,0)	8.62	-1.19	-0.73	-0.86	0.33
(13,0)	10.18	-1.21	-0.75	-0.95	0.26
Graphene	-	-1.29	-	-	-

Table 14 .Binding energy (eV) of triphenyl PPV to different carbon nanotubes, with graphene for comparison.

In Table 14 above, are the binding energies for the different diameter tubes. As seen for the smaller tubes, due to bond angle strain which invariably affects the conjugation in the aromatic rings, the stacking between the polymer and the tubes are slightly perturbed resulting in lower binding energies.

However, as the tube diameter increases, there is a sharp rise in the binding energies towards that of graphene, which has no constraint in its aromatic conjugation and therefore will in turn have a higher stacking order effect which maximizes π - π stacking interaction.

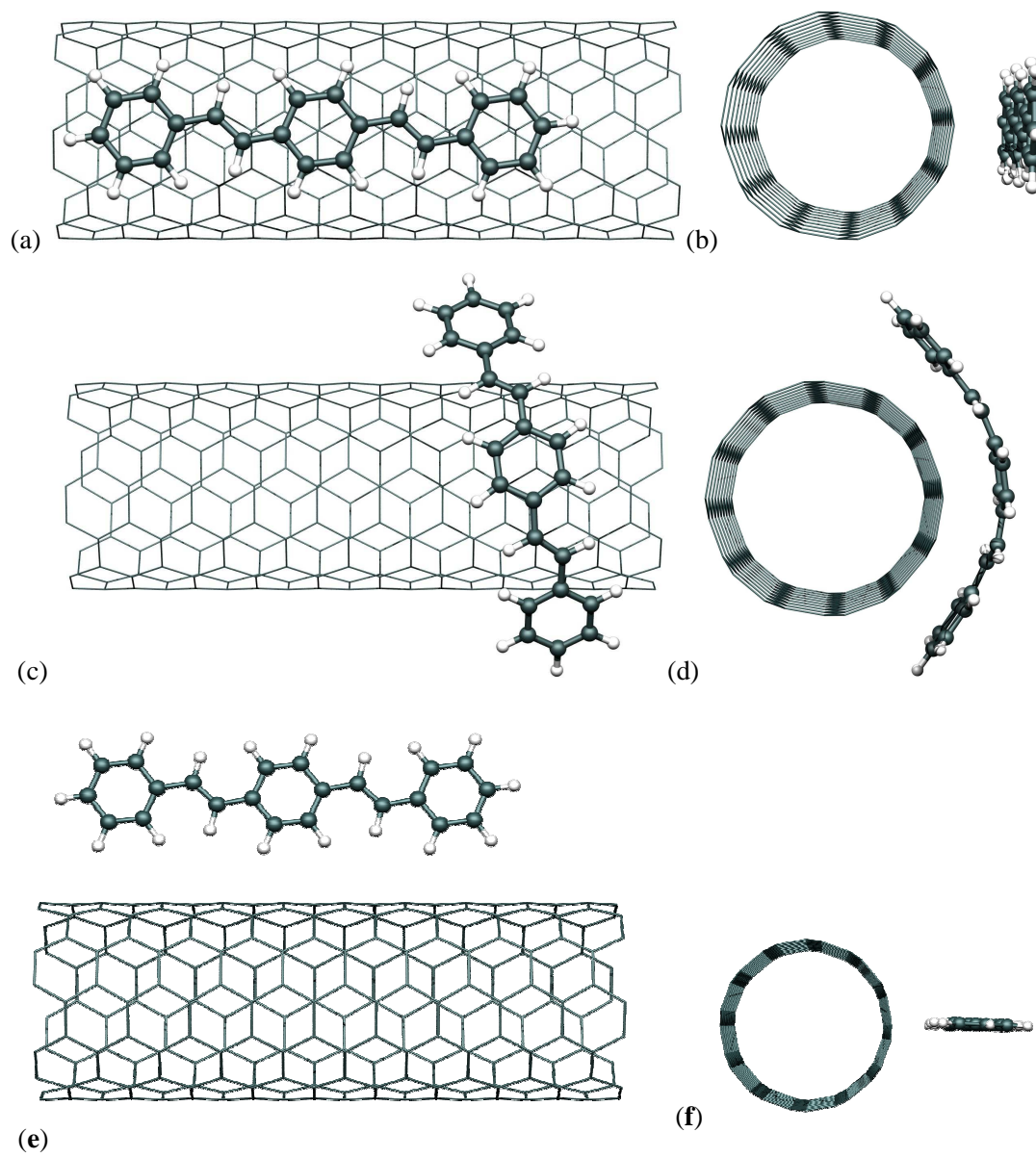


Figure 43 PPV interacting with (6,6) metallic nanotube, (a-b) parallel, (c-d) perpendicular and (e,f) axial to the nanotube axis. (a,c,e) side and (b,d,f) end view (showing complete supercell).

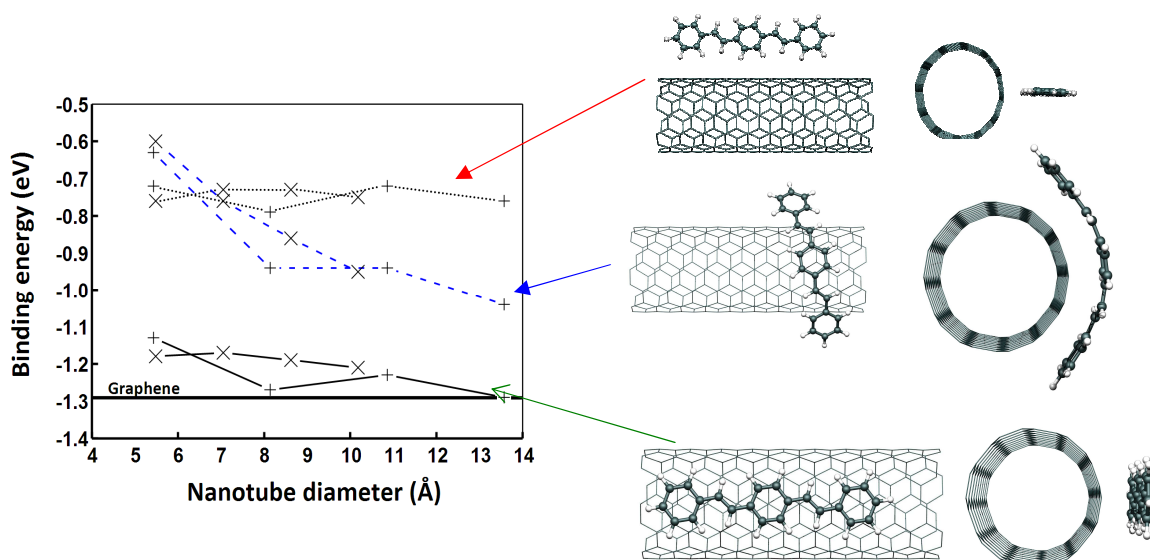


Figure 44. Calculated binding energy of triphenyl PPV to different carbon nanotubes (eV).

× = Semiconducting tubes, + = Metallic. Solid line indicates PPV aligned along tube axis parallel to the nanotube surface, Dotted line indicates along the tube axis perpendicular to the nanotube surface, and Dashed line indicates PPV wrapped circumferentially around the nanotube, parallel to the nanotube surface.

Metallic tubes are (4,4), (6,6), (8,8) and (10,10), semiconducting tubes are (7,0), (9,0), (11,0) and (13,0). PPV binding to graphene is given for comparison. Arrows indicate the orientation of the PPV on SWCNTs.

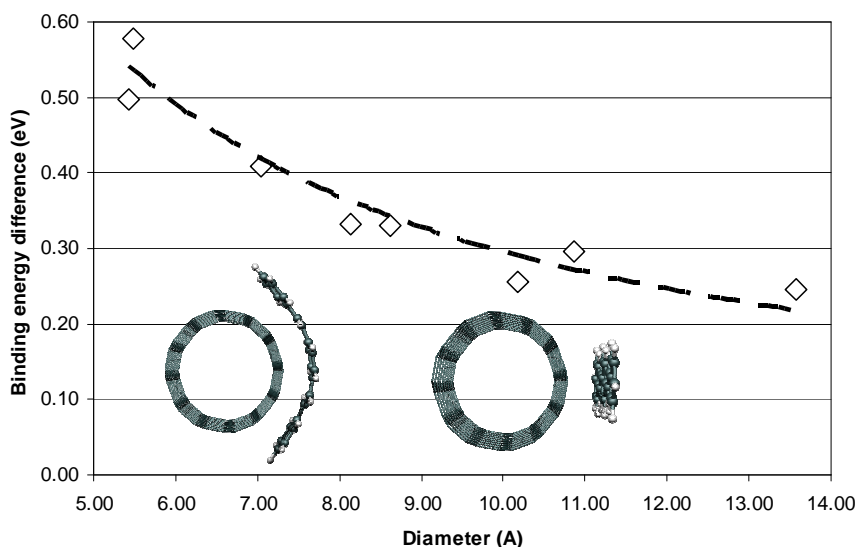


Figure 45. Binding energy difference between carbon nanotubes and triphenyl PPV parallel to the nanotube surface, either lying along the tube axis or bent circumferentially. Included is a $1/x$ curve which shows a better fit to the data than an inverse exponential. This curve shows that for large diameter nanotubes the PPV orientation dependence will become increasingly weak.

PPV in a circumferential orientation remains curved in order to maximize π - π stacking interaction with the tube, with an energy cost associated with the distortion. For this reason the energy difference between the circumferential and axial configurations decreases with increasing tube diameter, see Figure 45.

Thus, the calculations show there is a strong thermodynamic driving force for PPV-CNT interaction, with the axis of the polymer preferentially aligning with that of the nanotube.

This theoretical work is in agreement with the experimental work by F. Massuyeau et al [69] in our laboratory, who studied composite mixtures of PPV with SWCNTs synthesized inside nanoporous alumina templates. They found that polarized-resolved Raman spectra exhibit strong anisotropic orientation behavior for the SWCNT and also the conjugated polymer chains after their conversion into PPV, which was seen to be dependent on the polarization angle, θ . They mounted the composite sample on a rotating stage to provide the tilt in the angle θ_m between the polarization and the pore axis directions. Their Raman spectra (Figure

46a) of the nanotube RBM and the tangential mode (G band) were recorded with parallel polarizations of the incoming and scattered light (VV configuration) as a function of the measured angle θ_m . For both modes, the Raman peaks intensities decrease from $\theta_m = 0^\circ$ to 90° and increase from $\theta_m = 90^\circ$ to 180° . The G band intensity is reported in blue with red line in a polar diagram (Figure 46c) from $\theta_m = 0^\circ$ to 360° . They observed a strong optical anisotropy of the G band intensity with a ratio of about 5.6. Their G band intensities exhibit clearly an angular dependence which can be described by $I(\theta_m) \propto \cos^2(\theta_m)$. This optical anisotropy Raman behaviour is comparable to other aligned carbon nanotube systems which have also been observed in the emission and absorption behaviour of SWCNTs [70,71]. They therefore concluded that the observed maximum at $\theta_m = 0^\circ$ or 180° for a polarization direction parallel to the pore axis, was strong evidence that the SWCNTs inside the composite nanofibers are well aligned parallel to the pore axis and parallel to the nanofibers axis. A similar result was obtained for the PPV, showing that both PPV and SWCNTs exhibited the same preferential alignment.

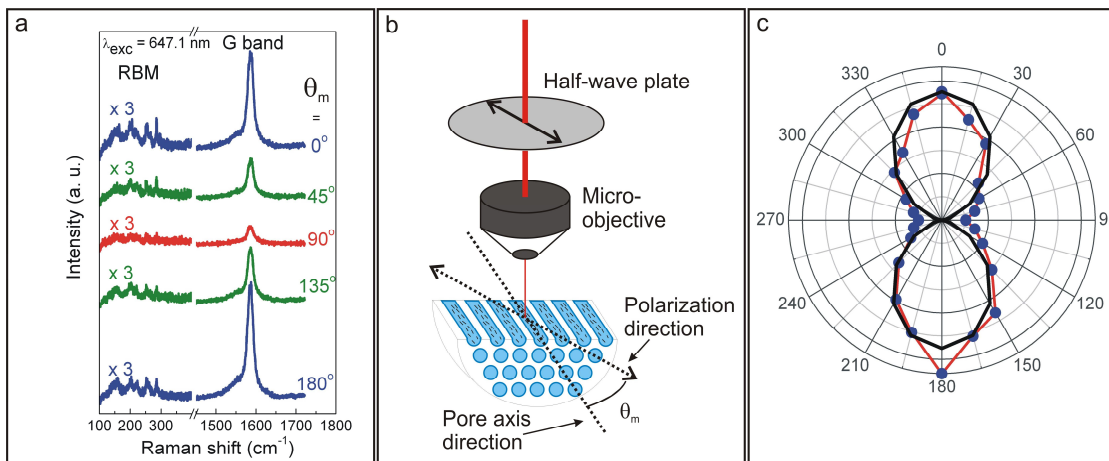


Figure 46 (a) Polarization resolved Raman spectra in the VV configuration as a function of the measured angle θ_m between the polarization direction and the pore axis direction, filled with PXC/SWNT, excitation line: 647.1 nm. (b) Experimental setup of the polarization resolved Raman experiment. (c) Polar diagram showing the G band intensity of SWNT as a function of the angle θ_m , experimental points are in blue with a red line, black line is the ideal $\cos^2 \theta_m$ function, taken from (F. Massuyeau et al [69]).

We next investigated the effect of charge transfer between a PPV chain oriented parallel to either a semi-conducting (7, 0) or a metallic SWCNT (4, 4). The nanotubes were chosen due to their similar diameters, as shown in Figure 47.

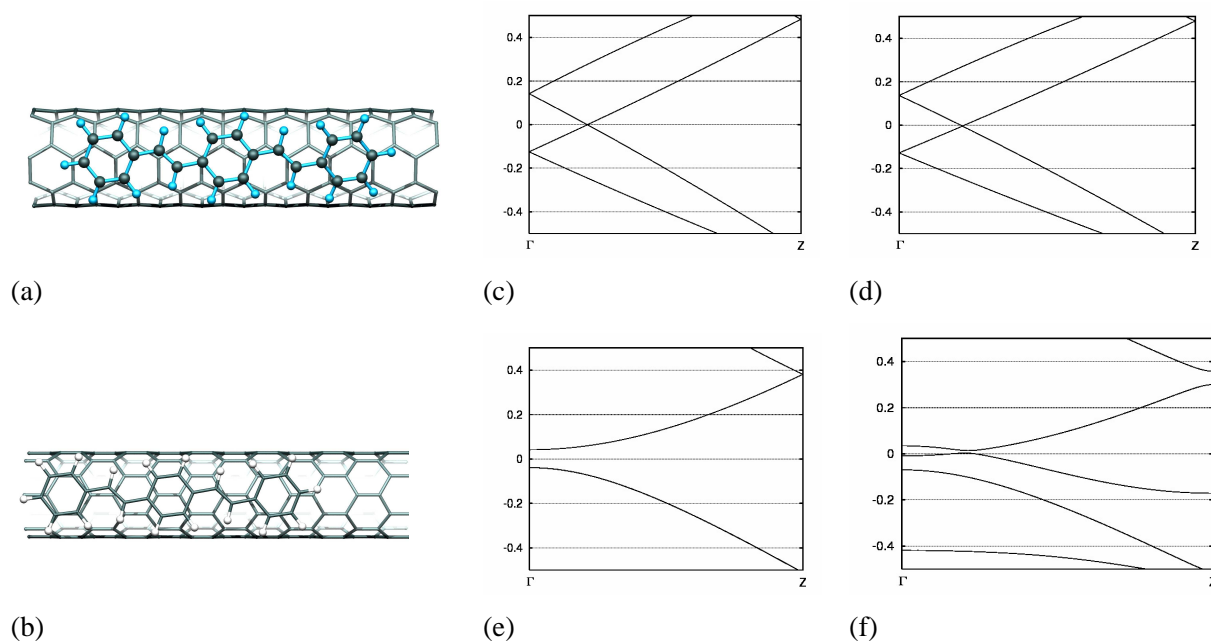


Figure 47. DFT calculations of triphenyl PPV-nanotube interaction. (a) Metallic (4,4) nanotube, (b) Semi-conducting (7,0) nanotube. (c,e) show band structures for the isolated (4,4) and (7,0) nanotube sections, and (d,f) in conjunction with the PPV section. Fermi levels are aligned at zero.

We indeed found strong interaction between the PPV and both nanotubes, with binding energies of 1.21 eV and 0.94 eV for the (4,4) and (7,0) tubes respectively, i.e. interaction is stronger with the metallic tube.

Figure 47 (c-f) show band structures for the tube segments with and without the PPV. The metallic (4,4) shows a slight up-shift of 0.02eV of the Fermi level indicating a small charge transfer from the PPV to the nanotube. This corresponds to a charge of 0.03e as determined by Mulliken population analysis which is not significant within the error bounds of the

Mulliken approach. However, the band structure around the Fermi level remains the same, suggesting negligible electronic coupling between the two systems around this energy range. The semiconducting (7,0) tube exhibits strong coupling between the PPV state near the Fermi level and the nanotube conduction band state. Unlike the metallic tube, there is a charge transfer from the nanotube to the PPV, visible in the band structure as an upward displacement of the Fermi level as compared to the isolated tube. The system is rendered semi-metallic with a small gap of 0.01 eV.

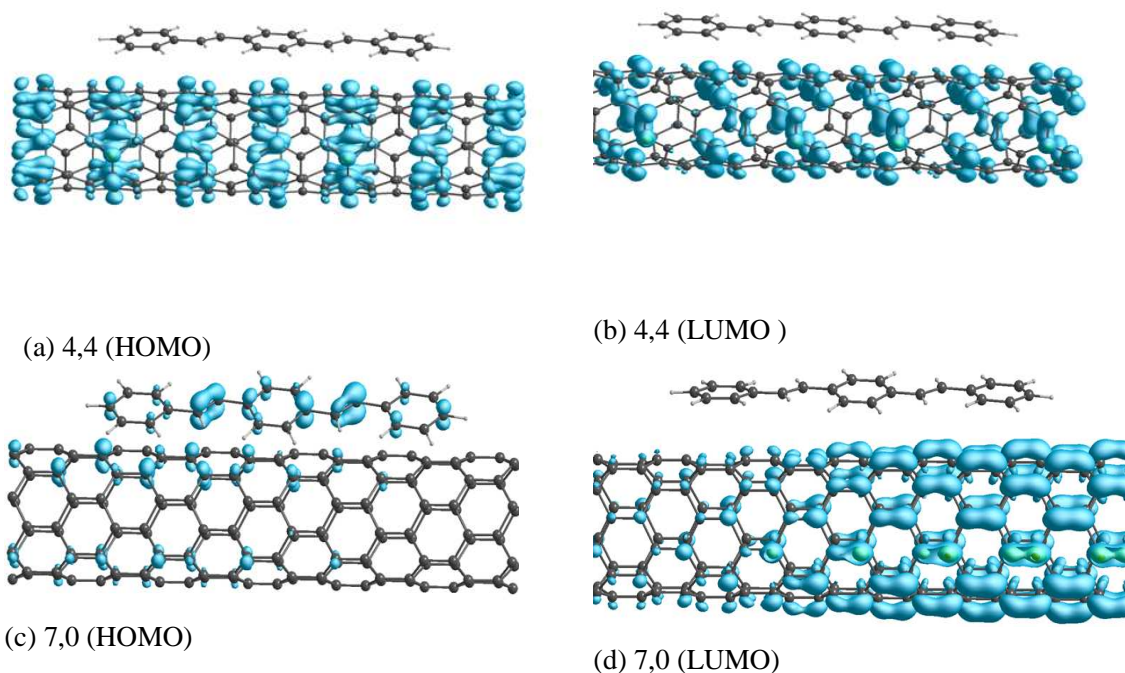


Figure 48 Square of wavefunction isosurface plots of HOMO and LUMO states for metallic 4,4 (a,b) and semiconducting 7,0 (c,d) nanotubes interacting with triphenyl PPV oligomer at the Γ -point of the Brillouin zone.

The wavefunction isosurface plot for the PPV interacting with either metallic (4,4) and semiconducting (7,0) tubes is shown in Figure 48.

For the metallic nanotube, it shows that the HOMO states are on the nanotube with no states on the PPV, which is an indication that the states around the Fermi level are nanotube like in agreement with our analysis above. The states also show no coupling between the nanotube and the PPV as seen in the band structure in Figure 47(c,d).

For the (7, 0) nanotube, the HOMO state has a mixed character with most of the state on the PPV. However, there is a strong coupling between the PPV and the nanotube as exhibited by the presence of some of the state on the nanotube. This is also observed in the band structures, where there is a crossing of the PPV state around the Fermi level (Figure 47(e,f).

We found no significant charge transfer between PPV and the nanotube in any of the calculations, but note that these are ground state calculations and do not reflect electron distribution after exciton formation.

This suggests however that PPV exciton formation in semiconducting nanotube systems should show strong PPV-CNT interaction (e.g.; for light capture in solar cells) whereas less coupling in metallic nanotube-PPV interaction.

The results of these simulations can be used to correlate the role of aromaticity and backbone stiffness to the interfacial behaviour between a SWCNT and PPV polymer, and this information can be used to optimize the desired properties of the bulk material.

5.8 Summary

Density functional theory, which in principle gives the true ground state energy and electronic density of any system, is known to give an imperfect description of the long range van der Waals (vdW) interactions within the widely used local density approximation (LDA) or generalized-gradient approximations (GGA) for the exchange-correlation energy. DFT has proven to be quite successful and in good quantitative agreement with experimental data for sp^2 -like materials, especially graphite. In addition, DFT gives a better description of these π -systems than empirical methods and is able to capture the underlying physics.

The success of the LDA is not fortuitous and is more suitable than the GGA to study weakly interacting systems like the π -stacking interaction on sp^2 -like materials. Indeed, the GGA is

known to usually underestimate binding energies. This is problematic for example in the case of graphite where, within the GGA, two graphene layers are completely unbound whereas the LDA interlayer separation and spacing are very close to the experimental. In the same way, two parallel benzene molecules are found to be unbound using the GGA, whereas our LDA results are in quite good agreement with high level quantum chemistry calculations.

Therefore our use of LDA on these systems in the absence of vdW is justified, since the vdW will only act in changing the binding energy and will not affect the overall results of our findings. Nevertheless we find that our binding energies are somewhat basis set dependent, notably we find that increasing the number of basis function per carbon from 22 to 38 contributes to a decrease in the PPV binding energy to graphene. This does not qualitatively change our results and will be a systematic error in the case of our relative energy studies, in future work we would use largest possible basis sets and should investigate the effects of basis set superposition errors. Unfortunately time constraints precluded this study in this thesis work.

For the benzene dimer interaction calculation, we found energy minimum structures as the T-shaped and parallel-displaced (PD) with transitional state being the parallel-stack (PS) conformations. This was also seen in the contour map plot with other meta-stable energy structures. For benzene on graphene and nanotubes, the stack conformation (similar to an AB-graphite conformation) was found to be the most favoured with an AA-stacking conformation having a higher energy and therefore highly improbable for the adsorption of benzene and the T-shape being significantly less stable.

Unlike for benzene we found the interaction between two PPV-PPV molecules to orient similarly to PPV-SWCNTs or PPV-graphene, and the most favourable orientation is when the PPV molecules are aligned parallel with a binding dependence on orientation of the PPV decreasing with increasing diameter. These results show a transition from T-shape orientation for small molecules to parallel stacking for larger systems.

For the two conformation of PPV-PPV molecular interactions studied, the planar conformation was found to be 0.31 eV more stable than the bent conformation.

Finally, wavefunction isosurface plots of some selected nanotubes, suggests very little effect of PPV adsorptions on the electronic structure of SWCNTs; however more effect for semi-conducting nanotubes than metallic but without any significantly perturbing the electronic properties of the systems. This means the noncovalent functionalization by π -stacking is then completely different from covalent functionalization, which strongly modifies the properties of the CNT.

So we expect a change in structural behaviour; PPV crystals will stack herringbone, PPV in composites with graphene or nanotubes will stack parallel.

5.9 References

- [1] J. Lehn, *Angewandte Chemie-International Edition* **27**, 89-112 (1988).
- [2] L. Stryer, *Biochemistry* (W. H. Freeman and Company, New York, 1995).
- [3] G. Jeffrey, W. Saenger, *Spinger-Verlag* (1991).
- [4] S. Grimme, *Angew. Chem. Int. Ed. Engl* **47**, 3430-3434 (2008).
- [5] R. G. K. A. Petitjean, A. Petitjean, R. G. Khoury, N. Kyritsakas and J. M. Lehn, [[*J. Am. Chem. Soc.*]] **126**, 6637–6647 (2004).
- [6] J. W. G. Bloom, S. E. Wheeler, *Angewandte Chemie International Edition* **50**, 7847-7849 (2011).
- [7] F. JACOB, J. MONOD, *J. Mol. Biol* **3**, 318-356 (1961).
- [8] B. H. Zimm, *J. Chem. Phys.* **33**, 1349 (1960).
- [9] J. H. Parish, *Biochemical Education* **13**, 92-92 (1985).
- [10] C. D. Sherrill, T. Takatani, E. G. Hohenstein, *J. Phys. Chem. A* **113**, 10146-10159 (2009).
- [11] R. Peverati et K. K. Baldrige, *J. Chem. Theory Comput.* **4**, 2030-2048 (2008).
- [12] S. Tsuzuki, K. Honda, T. Uchimaru, M. Mikami, K. Tanabe, *Journal of the American Chemical Society* **124**, 104-112 (2002).
- [13] W. Langel, *Journal of Solid State Electrochemistry* **6**, 359-360 (2001).
- [14] M. O. Sinnokrot, E. F. Valeev, C. D. Sherrill, *Journal of the American Chemical Society* **124**, 10887-10893 (2002).
- [15] C. A. Hunter, *Philosophical Transactions: Physical Sciences and Engineering* **345**, 77-85 (1993).
- [16] J. Grant Hill, J. A. Platts, H-J. Werner, *Phys. Chem. Chem. Phys.* **8**, 4072 (2006).
- [17] M. Gordon, L. Slipchenko, H. Li, J. Jensen, *Annual Reports in Computational Chemistry* **3**, 177-193 (2007).
- [18] A. L. Ringer, C. D. Sherrill, *Chemistry - A European Journal* **14**, 2542-2547 (2008).
- [19] M. O. Sinnokrot et C. D. Sherrill, *The Journal of Physical Chemistry A* **110**, 10656-10668 (2006).
- [20] M. O. Sinnokrot, C. D. Sherrill, *The Journal of Physical Chemistry A* **108**, 10200-10207 (2004).

- [21] T. Tran-Duc, N. Thamwattana, B. J. Cox, J. M. Hill, *Philosophical Magazine* **90**, 1771 (2010).
- [22] J. K. M. Sanders, C. A. Hunter, *Journal of the American Chemical Society* **112**, 5525-5534 (2005).
- [23] W. Kim, M. W. Schaeffer, S. Lee, J. S. Chung, P. M. Felker, *J. Chem. Phys.* **110**, 11264 (1999).
- [24] G. Fischer, *Chemical Physics Letters* **139**, 316-320 (1987).
- [25] J. M. Steed, T. A. Dixon, W. Klemperer, *J. Chem. Phys.* **70**, 4940 (1979).
- [26] P. M. Maxton, M. W. Schaeffer, P. M. Felker, *Chemical Physics Letters* **241**, 603-610 (1995).
- [27] M. W. Schaeffer, W. Kim, P. M. Maxton, J. Romascan, et P. M. Felker, *Chemical Physics Letters* **242**, 632-638 (1995).
- [28] K. Brendel, H. Mäder, Y. Xu, W. Jäger, *Journal of Molecular Spectroscopy* **In Press**, **Corrected Proof**, (2011).
- [29] S. Burley et G. Petsko, *Science* **229**, 23 -28 (1985).
- [30] C. A. Hunter, J. Singh, J. M. Thornton, *J. Mol. Biol* **218**, 837-846 (1991).
- [31] K. C. Janda, J. C. Hemminger, J. S. Winn, S. E. Novick, S. J. Harris, et W. Klemperer, *J. Chem. Phys.* **63**, 1419 (1975).
- [32] E. Arunan, H. Gutowski, *J. Chem. Phys.* 4294 (1993).
- [33] B. F. Henson, G. V. Hartland, V. A. Venturo, P. M. Felker, *J. Chem. Phys.* **97**, 2189 (1992).
- [34] M. P. Waller, A. Robertazzi, J. A. Platts, D. E. Hibbs, P. A. Williams, *Journal of Computational Chemistry* **27**, 491-504 (2006).
- [35] P. . Felker, P. . Maxton, M. Schaeffer, *Chem. Rev. Letts* 1787 (1994).
- [36] V. Venturo, P. Felker, *J. Chem. Phys.* 748 (1993).
- [37] K. S. Law, M. Schauer, E. R. Bernstein, *Dimers of Aromatic Molecules: (Benzene)(2), (Toluene)(2), and Benzene-Toluene.* (1984).
- [38] J. R. Grover, E. A. Walters, E. T. Hui, *The Journal of Physical Chemistry* **91**, 3233-3237 (1987).
- [39] H. Krause, B. Ernstberger, H. J. Neusser, *Chemical Physics Letters* **184**, 411-417 (1991).
- [40] M. Dion, H. Rydberg, E. Schröder, D. C. Langreth, B. I. Lundqvist, *Phys. Rev. Lett.* **92**, 246401 (2004).
- [41] R. Telling, M. Heggie, *Philosophical Magazine Letters* **83**, 411-421 (2003).
- [42] J.-C. Charlier, X. Gonze, J-P. Michenaud, *Europhys. Lett.* **28**, 403-408 (1994).
- [43] F. Tournus, J-C. Charlier, *Phys. Rev. B* **71**, 165421 (2005).
- [44] A. Rochefort, J. D. Wuest, *Langmuir* **25**, 210-215 (2009).
- [45] A. Fisher et P. Blöchl, *Physical review letters* **70**, 3263–3266 (1993).
- [46] O. V. Ershova, T. C. Lillestolen, et E. Bichoutskaia, *Phys. Chem. Chem. Phys.* **12**, 6483 (2010).
- [47] F. Tournus, S. Latil, M. I. Heggie, et J.-C. Charlier, *Phys. Rev. B* **72**, 075431 (2005).
- [48] G. U. Sumanasekera, B. K. Pradhan, H. E. Romero, K. W. Adu, et P. C. Eklund, *Phys. Rev. Lett.* **89**, 166801 (2002).
- [49] R. B. Capaz et M. J. Caldas, *Phys. Rev. B* **67**, 205205 (2003).

- [50] G. Zheng, S. J. Clark, S. Brand, et R. A. Abram, *J. Phys.: Condens. Matter* **16**, 8609-8620 (2004).
- [51] L. C. De Carvalho, C. N. Dos Santos, H. W. L. Alves, et J. L. A. Alves, *Microelectronics Journal* **34**, 623-625 (mai).
- [52] D. Chen, M. Winokur, M. Masse, et F. E. Karasz, *Polymer* **33**, 3116-3122 (1992).
- [53] D. Chen, M. J. Winokur, M. A. Masse, et F. E. Karasz, *Phys. Rev. B* **41**, 6759 (1990).
- [54] K. F. Voss, C. M. Foster, L. Smilowitz, D. Mihailovicacute, S. Askari, G. Srdanov, Z. Ni, S. Shi, A. J. Heeger, et F. Wudl, *Phys. Rev. B* **43**, 5109 (1991).
- [55] M. Dienwiebel, G. Verhoeven, N. Pradeep, J. Frenken, J. Heimberg, et H. Zandbergen, *Phys. Rev. Lett.* **92**, (2004).
- [56] M. Yang, V. Koutsos, M. Zaiser, *J. Phys. Chem. B* **109**, 10009-10014 (2005).
- [57] C. D. Tran, S. Lucas, D. G. Phillips, L. K. Randeniya, R. H. Baughman, et T. Tran-Cong, *Nanotechnology* **22**, 145302 (2011).
- [58] W. Yi, A. Malkovskiy, Y. Xu, X.-Q. Wang, A. P. Sokolov, M. Lebron-Colon, M. A. Meador, et Y. Pang, *Polymer* **51**, 475-481 (2010).
- [59] Z.Zhu, G. Lu, *Langmuir* **20**, 10751 (2004).
- [60] V. Lordi, N.Yao, *J. Mater. Res.* **15**, 2770 (2000).
- [61] B. McCarthy, J. N. Coleman, R. Czerw, A.B. Dalton, M. Panhuis, A. Maiti, A. Drury, P. Bernier, J. B. Nagy, B. Lahr, H. J. Byrne, D. L. Carroll, et W. J. Blau, *The Journal of Physical Chemistry B* **106**, 2210-2216 (2002).
- [62] S.Gotovac, H.Honda, Y.Hattori, K.Takahashi, H. Kanoh, et K. Kaneko, *Nano Letters* **7**, 583-587 (2007).
- [63] W. Liu, C-L Yang, Y-T. Zhu, M.Shan Wang, *The Journal of Physical Chemistry C* **112**, 1803-1811 (2008).
- [64] H. Ago, M. S. P. Shaffer, D. S. Ginger, A. H. Windle, et R. H. Friend, *Phys. Rev. B* **61**, 2286 (2000).
- [65] A. B. Dalton, C. Stephan, J. N. Coleman, B. McCarthy, P. M. Ajayan, S. Lefrant, P. Bernier, W. J. Blau, H. J. Byrne, *The Journal of Physical Chemistry B* **104**, 10012-10016 (2000).
- [66] D. W. Steuerman, A. Star, R. Narizzano, H. Choi, R. S. Ries, C. Nicolini, J. F. Stoddart, J. R. Heath, *The Journal of Physical Chemistry B* **106**, 3124-3130 (2002).
- [67] W. Z. Yuan, J. Z. Sun, Y. Dong, M. Häußler, F. Yang, H. P. Xu, A. Qin, J. W. Y. Lam, Q. Zheng, B. Z. Tang, *Macromolecules* **39**, 8011-8020 (2006).
- [68] A. Nish, J-Y. Hwang, J. Doig, R. J. Nicholas, *Nat Nano* **2**, 640-646 (2007).
- [69] F. Massuyeau, A. Yaya, J. L. Duvail, S. Lefrant, J. Wéry, J. Y. Mevellec, E. Faulques, C. P. Ewels, *In Praparation* (2011).
- [70] G. S. Duesberg, I. Loa, M. Burghard, K. Syassen, S. Roth, *Physical review letters* **85**, 5436-5439 (2000).
- [71] A. M. Rao, A. Jorio, M. A. Pimenta, M. S. S. Dantas, R. Saito, G. Dresselhaus, M. S. Dresselhaus, *Phys. Rev. Lett.* **84**, 1820 (2000).

Chapter 6

Summary, Conclusions and Future Directions

This work used the ab initio electronic structure calculation method (AIMPRO/LDA) and experimental Raman spectroscopy to investigate the structures and properties of weakly interacting complexes, by making use of some specific examples from nanoscale carbon based materials science.

Using a DFT/LDA approach we are able to provide a reliable and improved understanding of the nature of weak intermolecular interactions such as dipole-dipole, π - π stacking, charge-transfer complex and H- π interactions. These interactions are of great importance in many disciplines of science and play a major role in biological and molecular recognition processes.

We first considered the interaction of bromine molecules (oriented parallel and perpendicular) with graphite, graphene, and single-walled carbon nanotubes. For the adsorption of bromine on graphene, we found for the first time that when bromine molecules are oriented perpendicular to the surface of the graphene they form a dipole with a strong charge transfer. The molecule forms a ($\text{Br}^+ + \text{Br}^-$) pair making it infra-red active, and resulting in a small band gap opening in the underlying graphene (86meV). This is therefore a new form of bromine which was previously only considered as an unstable intermediate to bromine-induced carbon bond saturation. Our results show a possible unexpected difference in behaviour between graphene and graphite. It would be very useful to test the prediction of IR activity experimentally. This should be aided by the fact that both liquid bromine and isolated graphene are IR inactive and hence only the surface Br_2 should have any strong adsorption. Where Br_2 lies parallel to the graphene, no dipole occurs but a symmetrical charge transfer distribution between the pair of bromine atoms and the graphene is observed. Our calculated binding energies show that the parallel orientation is 0.15 eV less stable than the perpendicular orientation however this difference is small enough that, we propose that, at room temperature, these structures could be alternating due to a tumbling motion of the

Br_2 . In graphite, bromine molecules adopt a parallel orientation to the sheets with an associated charge transfer and this is in agreement with experimental data where available. Binding energies for both stage-1 (Br_2 /AA-graphite) and stage-2 (Br_2 /AABB) were calculated to be endothermic at low Br_2 coverage due to the binding energy of the Br_2 /graphite not being able to offset the interlayer separation energy for graphite: which was calculated as 36.74 meV/atom for AB- and with AA- being 12 meV/atom less stable. However after bromination there is a preferential stability for AA-stacking either side of the intercalated bromine layer. These current calculations does not seem to provide an answer as to why stage-1 brominated graphite is not stable, and this is clearly an area for further study. For the nanotubes, when bromine was oriented perpendicular to the isolated tubes, it behaves similarly as with graphene. When the CNTs are in bundles Br_2 intercalates within the bundles similarly to Br_2 intercalated graphites lying parallel to the hexagons. By similar extension, we assume the same phenomenon will happen for double-walled carbon nanotubes.

At high Br_2 concentration, polybromide chain structures will be thermodynamically favourable. But, the formation of these bromine chain structures is not spontaneous. There is an activation barrier calculated as -27.01kJ/mol thus kinetically these chain structures will not be feasible under ambient conditions. This barrier is due to the Coulombic interaction between bromine molecules as well as neighbouring holes in the graphene as a result of charge transfer from bromine. This suggest the intriguing possibility that heating bromine/carbon systems in a closed system (for example under pressure) to avoid bromine loss may encourage the formation of polybromide chains. The calculated results show that, physisorption does not result in any noticeable change in geometry of the substrates such as graphene, graphite and nanotubes. And due to the chemical inertness of these carbon materials, the binding energy depends only on the contact area between the substrate and adsorbates.

Secondly, we studied π - π stacking interactions between PPV oligomer chain with graphene, PPV and SWCNTs of different diameter and chirality. We first considered the simplest prototype of aromatic π - π interaction, the benzene dimer and we found energy minimum structures as the T-shaped (T) and parallel-displaced (PD) conformations with transition state

being the parallel-stack (PS) conformations. In various complex chemical and biological systems, aromatic rings can be found at different orientations and distances from each other which might not correspond to the potential energy minima for π - π interactions. Nevertheless, the aromatic rings might still interact favorably enough to contribute significantly to the overall stability of the system. Therefore, it is essential to obtain the potential energy curves for prototype systems in order to determine how π - π interactions depend on both the orientation and distance between these aromatic rings. To achieve that goal, we have computed the potential energy curves as a function of intermonomer distances for three important configurations of benzene dimer, namely the parallel stack (PS), the T-shaped (T), and parallel-displaced (PD) configurations. This was also seen in the contour map plot with other meta-stable energy structures. With benzene on graphene and SWCNTs, the stacking arrangement was found to be same as AB-graphite conformation which is the most favoured with the least favoured being the AA-stacking conformation which has a higher energy and therefore, will not occur for the adsorption of benzene.

Also, we noticed that, the interaction between two PPV molecules is different from PPV-SWCNTs or PPV-graphene. In the former, the parallel & perpendicular orientations have similar energies with a perpendicular type of arrangement occurring in the crystal packing of these polymers and other polyaromatic hydrocarbons. But for the PPV-SWCNTs or PPV-graphene, the most favoured conformation is when the PPV is oriented parallel on these substrates. Molecule/molecule interaction seems to be fundamentally different to molecule/substrate.

In the case of the nanotubes, binding energy dependence on the orientation of PPV with decreasing diameter was observed. Wavefunction isosurfaces plot of some selected interactions between SWCNTs/PPV, suggest very little effect on the electronic coupling near to the Fermi level between the PPV and SWCNTs. This implies that non-covalent functionalization by π -stacking is categorically different from covalent functionalization. It preserves the properties of SWCNTs that can provide an opportunity for tailoring the nanotube in other specific application such as electronics where structural integrity is very important.

In this thesis we have shown that the AIMPRO code, based on the DFT/LDA theory can be used to give insight on weak interactions that can occur between carbon nanosystems (graphites, graphenes, and SWCNTs) and molecules such as bromine, benzene, and PPV. These carbon nanosystems can be described as sp^2 hybridized carbon species in which LDA has been proven to well describe such hybridized form of carbon materials and hence our justification for the use of LDA approach and its ability to treat larger systems of this nature with significantly less computational effort as compared to higher levels of theory.

Other Future directions of this research include the following;

1. The LDA as used in this thesis has no dispersion correction term. It will be useful to compare the binding energies in these LDA results with that of a dispersion force corrected approach (which is in its final stage of testing before release in our AIMPRO code).
2. It will be interesting to vary the polymer chain length of the PPV oligomer used from two oligomer chains up to ten oligomer chains to see whether there will be variations in the alignment of the PPV chains with SWCNTs as the number of phenyl rings increases.
3. Our contour plots only show binding energy variation as a function of molecular translation, and it would be interesting to investigate the effect of molecular rotation as well.
4. Our experimental colleagues in the PMN group work with a PPV pre-cursor, MEH-PPV, and they are keen for us to model its interaction with nanotubes for comparison with that of PPV-SWCNT. There are other interesting conjugated polymers we could also consider.
5. Our calculation for the force to move PPV over the surface of graphene gives a direct prediction of the frictional force to slide PPV on graphene and this could be important for nanocomposites applications. It is necessary to also confirm this finding

experimentally, and this is currently being considered by one of our experimental collaborators at Manchester University, Dr. Ian Kinloch.

6. It could be interesting to see whether at very low temperatures bromine structural behaviour and hence charge transfer doping of graphene changes if the tumbling motion can be frozen out.
7. Future development of approximate methods (such as molecular mechanics force fields) that are computationally inexpensive and capable of modeling π - π and other types of weak interactions in larger systems will require very accurate benchmark results for prototype systems, such as benzene dimers and interactions involving charge transfers or dipolar interactions, and we hope the calculations presented here will be useful for this.

The problems associated with the size of the system in doing such a calculation with longer PPV chains and SWCNTs of any chirality and diameter will be easier to tackle with the AIMPRO code when the so-called "Filtration method" is introduced. This method uses a much smaller number of basis functions that gives an equivalent description of the system as obtained using our current large number of basis functions, resulting in significant speed up. Finally, we expect that a better understanding of weak intermolecular interactions and how they may be tuned will play a major role in the advancement of rational supramolecular design.

Résumé

Avec le logiciel AIMPRO, qui fournit une modélisation quantique basée sur la théorie de fonctionnelle de densité, on étudie plusieurs exemples importants de la faiblesse des interactions intermoléculaires dans les nanomatériaux de carbone. Au niveau mécanique quantique, nos calculs donnent une compréhension fiable et améliorée du rôle et de la fonction des interactions intermoléculaires faibles, ce qui ne peut pas être prédit par des méthodes conventionnelles comme les potentiels interatomiques classiques.

Premièrement, on étudie l'interaction entre le brome physisorbé sur les nanomatériaux de carbone (graphène, graphite, nanotubes de carbone simple [SWCNT] et double [DWCNT] parois). Pour le graphène, nous trouvons une nouvelle forme de Br_2 , à notre connaissance jamais présentée dans la littérature, où la molécule se trouve perpendiculaire à la feuille de graphène avec un dipôle fort. La bromation ouvre un gap de petite taille (86 meV) dans la structuré de bande électronique et dope fortement le graphène. Dans le graphite, Br_2 reste parallèle aux couches de carbone avec un transfert de charge moins fort et sans dipôle moléculaire. À plus haute concentration, la formation de chaînes de polybromure est thermodynamiquement favorisée, mais n'a pas lieu spontanément à cause d'une barrière d'activation appréciable (27,01 kJ / mol). Avec les nanotubes monoparoi, le Br_2 reste perpendiculaire à la surface du tube, comme observé avec le graphène; dans les fagots, le Br_2 s'intercale comme dans le graphite. Les spectres Raman sont enregistrés afin de vérifier ce résultat.

Dans la deuxième partie, on étudie des interactions d'empilement de type π - π entre le benzène d'une part, les chaînes oligomères de PPV d'autre part, avec des nanomatériaux de carbone. Pour le dimère du benzène, nous avons réussi à reproduire les structures stables trouvées par ailleurs via des calculs de plus haut niveau de théorie ; pour le benzène sur le graphène ou sur les SWCNTs, l'empilement est de type AB comme dans le graphite. L'orientation de l'interaction dans le cas PPV / PPV est différente de celle obtenue dans le cas PPV / nanotube ou PPV / graphène. Dans le premier cas des plans moléculaires sont orthogonaux, semblable à un empilement de PPV ou d'autres hydrocarbures aromatiques polycycliques. Dans les autres cas, l'axe de la chaîne de PPV se trouve parallèle au plan du graphène comme à l'axe des nanotubes, ce qui est attribué à des effets d'empilement π - π . L'analyse des fonctions d'onde près du niveau de Fermi suggère qu'il y a peu de couplage électronique entre PPV et SWCNTs. La différence d'interaction prévue entre PPV et nanotubes semi-conducteurs ou métalliques suggère une nouvelle conception de composites PPV-SWCNT pour les dispositifs électroluminescents organiques.

Mots clé: Graphite, Graphène, Brome, PPV, SWCNT, DFT, Raman, AIMPRO.